| | |
|---|---|
| **Titre:** Title: | Aerodynamic Optimization of Aircraft Wings Using a Coupled VLM-2.5D RANS Approach |
| **Auteur:** Author: | Matthieu Parenteau |
| **Date:** | 2017 |
| **Type:** | Mémoire ou thèse / Dissertation or Thesis |
| **Référence:** Citation: | Parenteau, M. (2017). Aerodynamic Optimization of Aircraft Wings Using a Coupled VLM-2.5D RANS Approach [Master's thesis, École Polytechnique de Montréal]. PolyPublie. https://publications.polymtl.ca/2555/ |

UNIVERSITÉ DE MONTRÉAL

# AERODYNAMIC OPTIMIZATION OF AIRCRAFT WINGS USING A COUPLED VLM-2.5D RANS APPROACH

MATTHIEU PARENTEAU
DÉPARTEMENT DE GÉNIE MÉCANIQUE
ÉCOLE POLYTECHNIQUE DE MONTRÉAL

MÉMOIRE PRÉSENTÉ EN VUE DE L'OBTENTION
DU DIPLÔME DE MAÎTRISE ÈS SCIENCES APPLIQUÉES
(GÉNIE AÉROSPATIAL)
MAI 2017

UNIVERSITÉ DE MONTRÉAL

ÉCOLE POLYTECHNIQUE DE MONTRÉAL

Ce mémoire intitulé :

AERODYNAMIC OPTIMIZATION OF AIRCRAFT WINGS USING A COUPLED VLM-2.5D RANS APPROACH

présenté par : PARENTEAU Matthieu
en vue de l'obtention du diplôme de : Maîtrise ès sciences appliquées
a été dûment accepté par le jury d'examen constitué de :

M. TRÉPANIER Jean-Yves, Ph. D., président
M. LAURENDEAU Éric, Ph. D., membre et directeur de recherche
M. SERMEUS Kurt, Ph. D., membre

## DEDICATION

*To all my friends from the lab*
*and my family...*

## ACKNOWLEDGEMENTS

I would first like to thank my research director Éric Laurendeau. He has taken the time to give me sound advice throughout my research project. He also gave me the chance to complete a 5-month research internship at the National Office for Aerospace Studies and Research (ONERA) in Paris, France. It was an unforgettable professional and personal experience.

I would also like to thank Gérald Carrier and Michel Costes for their warm welcome during my internship at ONERA in Paris in the applied aerodynamics department. They offered me excellent support throughout the course.

Finally, I would like to thank all my colleagues in the lab who have helped me directly or indirectly to carry out my research project. I would like to thank Simon, Frédéric, Julien, Anthony, Athanas, Carlos, Sylvain, Pierre and Khazem ... Thank you all !

# RÉSUMÉ

Le processus de conception d'avion de transport civil transsonique est complexe et requiert une forte gouvernance afin de gérer toutes les phases de développements de programme. Il y a un besoin dans la communauté de développer des modèles numériques pour toutes les disciplines qui permettent de relier les phases de design conceptuel, préliminaire et détaillée de façon continue, de telle sorte que les choix faits soient consistants entre eux.

L'objectif de ce travail est de développer un modèle aérodynamique adapté pour l'optimisation conceptuelle multidisciplinaire avec un faible coût de calcul et une fidélité suffisante pour explorer un vaste espace de conception dans les régimes transoniques et basses vitesses avec systèmes hypersustentateurs. L'approche est basée sur la Méthode non-visqueuse *Vortex Lattice Method* (VLM), sélectionnée pour son faible temps de calcul. Les effets visqueux sont modélisés avec des calculs RANS bidimensionnels haute fidélité effectués à différentes sections le long de l'envergure de l'aile. Les données de sections visqueuses sont calculées avec les conditions d'une aile en flèche infinie pour inclure les effets de l'écoulement transverse qui sont important dans la prédiction du coefficient de portance maximal. Ces effets visqueux sont incorporés itérativement avec le VLM à l'aide d'un algorithme de couplage de type *alpha* modifié spécialement pour prendre en compte des données avec aile en flèche. De plus, une dissipation artificielle est ajoutée afin de stabiliser la solution dans la région post-décrochage.

La précision de la méthode est comparée à celle des solutions 3D RANS sur le *Bombardier Research Wing* (BRW) avec et sans systèmes hypersustentateurs. Les résultats démontrent une précision impressionnante de l'approche RANS VLM/2.5D par rapport aux solutions 3D RANS. De plus, les solutions de l'approche RANS VLM/2.5D s'effectuent en quelques secondes seulement sur un ordinateur classique.

Finalement, le solveur aérodynamique est implémenté dans un cadre d'optimisation avec une méthode de type *Covariant Matrix Adaptation Evolution Strategy* (CMA-ES). Des optimisations à basse vitesse et haute vitesse avec fonction mono-objective sont réalisées, ainsi que des optimisations avec fonction objective-composée en combinant des objectifs basses vitesses et hautes vitesses. D'autre part, l'approche VLM/2.5D est capable de capter les cellules de décrochage. Par conséquent, cette caractéristique est utilisée pour définir un nouveau critère de décrochage selon l'envergure de l'aile afin d'être utilisé comme contrainte d'optimisation.

Le travail conclue sur les limites de la méthode et sur les prochains développements possibles.

# ABSTRACT

The design process of transonic civil aircraft is complex and requires strong governance to manage the various program development phases. There is a need in the community to have numerical models in all disciplines that span the conceptual, preliminary and detail design phases in a seamless fashion so that choices made in each phase remain consistent with each other.

The objective of this work is to develop an aerodynamic model suitable for conceptual multi-disciplinary design optimization with low computational cost and sufficient fidelity to explore a large design space in the transonic and high-lift regimes. The physics-based reduce order model is based on the inviscid Vortex Lattice Method (VLM), selected for its low computation time. Viscous effects are modeled with two-dimensional high-fidelity RANS calculations at various sections along the span and incorporated as an angle of attack correction inside the VLM. The viscous sectional data are calculated with infinite swept wing conditions to allow viscous crossflow effects to be included for a more accurate maximum lift coefficient and spanload evaluations. These viscous corrections are coupled through a modified alpha coupling method for 2.5D RANS sectional data, stabilized in the post-stall region with artificial dissipation.

The fidelity of the method is verified against 3D RANS flow solver solutions on the Bombardier Research Wing (BRW). Clean and high-lift configurations are investigated. The overall results show impressive precision of the VLM/2.5D RANS approach compared to 3D RANS solutions and in compute times in the order of seconds on a standard desktop computer.

Finally, the aerodynamic solver is implemented in an optimization framework with a Covariant Matrix Adaptation Evolution Strategy (CMA-ES) optimizer to explore the design space of aerodynamic wing planform. Single-objective low-speed and high-speed optimizations are performed along with composite-objective functions for combined low-speed and high-speed optimizations with high-lift configurations as well. Moreover, the VLM/2.5D approach is capable of capturing stall cells phenomena and this characteristic is used to define a new spanwise stall criteria to be introduced as an optimization constraint.

The work concludes on the limitations of the method and possible avenues for further research.

# TABLE OF CONTENTS

# LIST OF TABLES

# LIST OF FIGURES

# LIST OF ACRONYMS AND ABBREVIATIONS

| | |
|---|---|
| RANS | Reynold's Averaged Navier-Stokes |
| VLM | Vortex Lattice Method |
| CMA-ES | Covariant Matrix Adaptation Evolution Strategy |
| MDO | Multi-Disciplinary Design Optimization |
| CMDO | Conceptual Multi-Disciplinary Design Optimization |
| LLT | Lifting-Line Theory |
| CFD | Computational Fluid Dynamic |
| NS | Navier-Stokes |
| DNS | Direct Numerical Simulation |
| AoA | Abgle of Attack |
| MTOW | Maximum Take-Off Weight |
| BRW | Bombardier Research Wing |

# LIST OF APPENDICES

# CHAPTER 1 INTRODUCTION

Basic concepts are presented in this chapter along with the elements of the problematics and the research objectives.

## 1.1 Context

The design of a new aircraft is a major challenge today for the main Original Equipment Manufacturers (OEM) like Airbus, Boeing and Bombardier. The development can extend up to 15 years with costs up to billion dollars. The final design must also comply with tight environmental, noise and security constraints. The aircraft aerodynamic characteristics are crucial in achieving these goals.

Aircraft design is made of three distinct design phases, preliminary, conceptual and detailed design. These phases require different results and fidelity levels, thus different tools are necessary. In conceptual design, the aerodynamic analysis comes mainly from knowledge-based and low-fidelity methods with low computation cost, because hundreds if not thousands of concepts are evaluated.

Moreover, nearly 80% of the life-cycle cost are induced by choices made in the conceptual phase (Figure 1.1). Errors made in this phase are difficult and costly to repair and must be avoided. The aerodynamic and structural analysis are particularly prone to errors due to the low-fidelity methods used and the complex interaction between the disciplines involved (Rizzi, 2011).

## 1.2 Basic Concepts

### 1.2.1 Computational Fluid Dynamics

Aerodynamics is the study of fluid motion interaction with an object. The mechanics of a fluid is described by the Navier-Stokes (NS) equations. Unfortunately, they cannot be solved analytically for real engineering applications. Therefore, they are solved numerically by discretizing the flow domain onto a mesh. A popular approach to solving the discretized equations is by Finite Volume method.

Fluid motion consists mainly of two regimes, laminar and turbulent. Laminar is characterized by a steady and smooth flow where turbulent flow is described by chaotic changes in pressure and velocity (Figure 1.2).

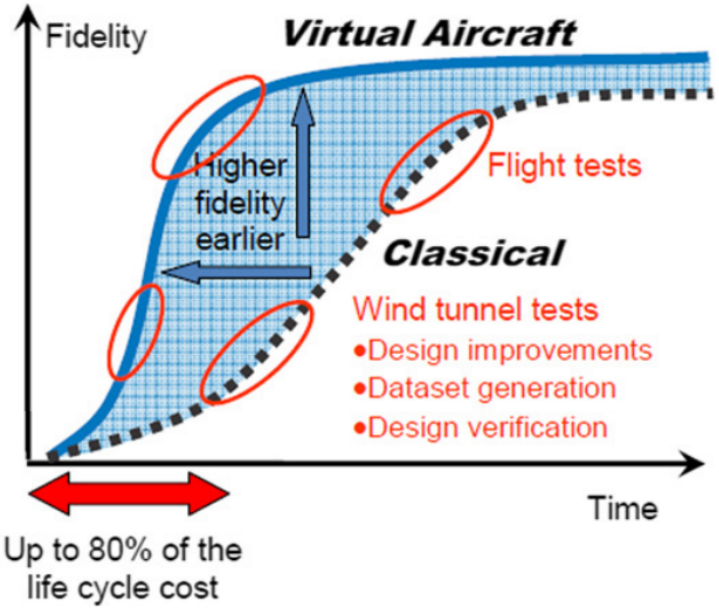


Figure 1.1 Contemporary product development contrasted against Virtual Aircraft approach (Source : Rizzi (2011))

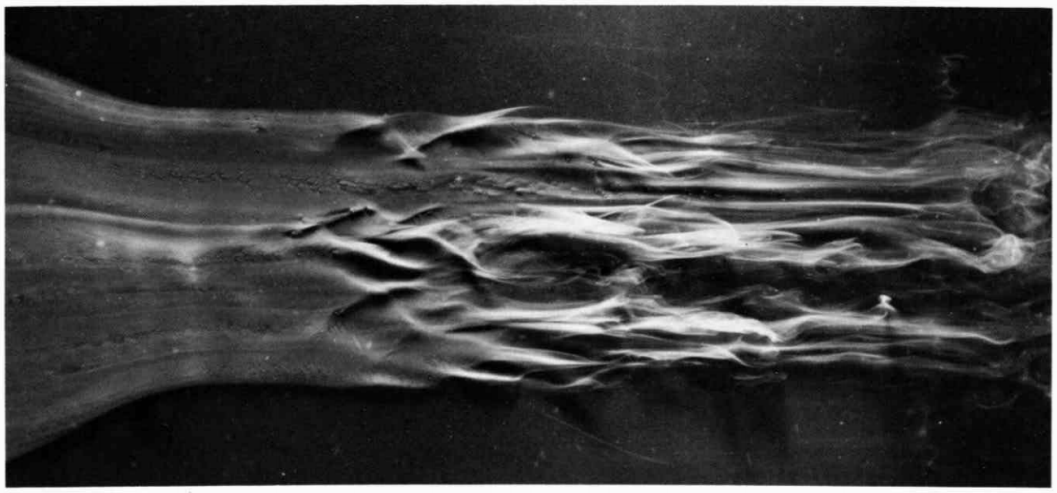

Figure 1.2 Natural transition from laminar to turbulent on a slightly inclined plate. *ONERA photograph, Werlé 1980* (Source : Dyke (1988))

### Direct Numerical Solution (DNS)

Solving directly the Navier-Stokes equations requires solving all the scales of turbulence both in space and time where the smallest scale is called the Kolmogorov microscales. The Kolmogorov microscale varies with the Reynolds number of the flow and requires very fine meshes to solve the smallest scale. The computation needed to solve directly the NS equations for

typical Reynolds number over a transport aircraft currently exceeds the capacity of supercomputers. Therefore, DNS is not suitable for aircraft analysis, let alone design.

### Reynolds Averaged Navier-Stokes (RANS)

The turbulent flow can be decomposed into a mean and a fluctuating part. In other words, the NS equations can be averaged, which leads to the Reynolds Averaged Navier-Stokes (RANS). However, the fluctuating velocity is still present in the RANS equations as the Reynolds stress. Turbulence modeling was then created to tackle the problem of modeling the Reynolds stress.

RANS is much more available in terms of computational cost compared to DNS and has become a main tool in aircraft design with the capabilities to model the flow physics with high fidelity. However, RANS still requires the flow field to be discretized and great care must be put into the mesh generation to ensure the boundary layer and the flow physics are well resolved. Depending on the available computer resources, RANS calculation can take multiple days. It is still out of reach for conceptual design phase were many configurations must be analyzed in weeks.

### Euler Equations

If the viscous terms in the NS equations are ignored, the Euler equations can be derived. By ignoring viscous terms, the boundary layer is ignored and turbulence modeling becomes unnecessary. Thus, a coarser mesh can be used which reduces drastically the computation cost compared to RANS. Euler codes can model compressible and rotational flows. Shock waves are captured, which makes them interesting for transonic aircraft design in cruise conditions. However, viscous effects are ignored and the wing stall cannot be captured, which is a crucial characteristic when designing a wing. They also affect the location and strength of shock waves, which are important parameters affecting wing performances.

### Full Potential Flow

Further simplification from the Euler equations can be made by assuming the flow is irrotational. This simplification allows the velocity to be replaced by the potential. Only one equation is solved for one variable which reduces again the computational cost with still the ability to handle compressibility. These methods are referred to as the full potential equation. However, vortex flows cannot be modeled, which becomes important at higher angles of attack and a new condition must be added to enable the calculation of lift from the wing. This is called

the Kutta condition and it is applied by modeling the wake as a thin surface emanating from the wing trailing edge. Even though full potential methods are fast and can accurately capture weak transonic shock waves, they still require the flow field to be discretized with the addition of the wake, which demands important pre-processing efforts.

**Linear Potential Flow**

The full potential flow can be linearized by ignoring the higher-order terms and assuming an incompressible flow. This linearization allows the equation to be solved on the surface of the geometry. The flow field discretization can now be ignored. Many codes have been developed using different representations of the geometry from simple thin lifting surfaces (Vortex Lattice Method) to complex higher fidelity wing-body geometries (Panel Method).

The governing equation for potential flow starts from the continuity equation :

$$\frac{d\rho}{dt} + \nabla \cdot (\rho V) = 0 \tag{1.1}$$

for steady and incompressible flow :

$$\nabla V = 0 \tag{1.2}$$

If the vorticity $\xi$ is equal to zero at all point in the field, the flow is considered irrotational. In the flow field, the vorticity is equal to the curl of the velocity, thus for irrotational flow :

$$\xi = \nabla \times V = 0 \tag{1.3}$$

If $\phi$ is a scalar function :

$$\nabla \times (\nabla \phi) = 0 \tag{1.4}$$

where $\phi$ is the velocity potential

$$V = \nabla \phi \tag{1.5}$$

$$\nabla^2 \phi = 0 \tag{1.6}$$

Incompressible, irrotational and inviscid flow are described by Laplace's equation (Equation 1.6). Laplace's equation is a linear equation, which means that a sum of elementary fluid solutions of Laplace's equation is also a solution of Laplace's equation (principal of superposition, Equation 1.7). Elementary solutions can therefore be superposed to solve the flow around complex geometries for which analytical solutions are not possible. Figures 1.3 and 1.4 present the different hierarchy of fluid flow models with their computation costs and geometry detail representation.

$$\phi = \phi_1 + \phi_2 + ... + \phi_n \tag{1.7}$$

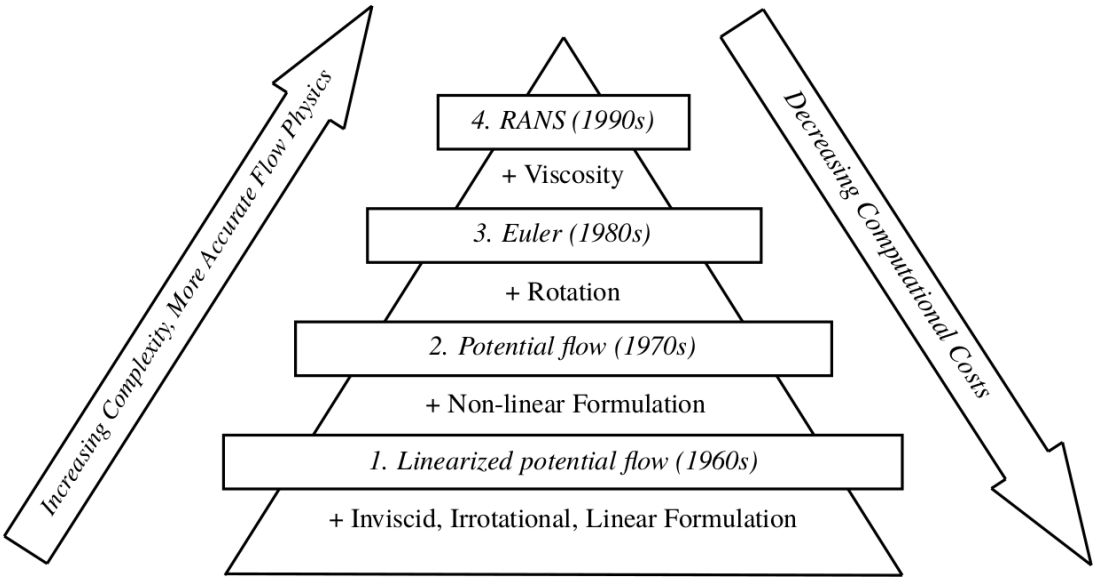


Figure 1.3 Hierarchy of fluid flow models (Source : Jameson (2004)).

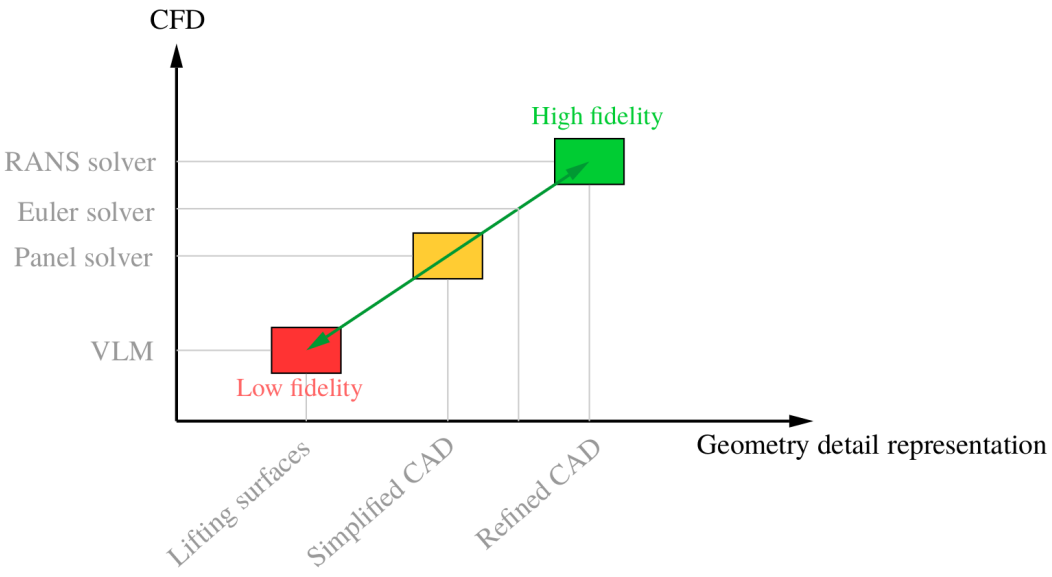


Figure 1.4 Multi-fidelity model in function of CFD method and geometry detail (Source : Mariens (2012).

### Kutta Condition and Generation of Lift for Potential Flow

The lift is directly proportional to the circulation around the body. As it was derived for a circular cylinder, the lift per unit span is given by the well-known Kutta-Joukowski theorem(Equation 1.8),

$$L' = \rho_\infty V_\infty \Gamma \tag{1.8}$$

but, there is an infinite number of solutions for the circulation $\Gamma$ (Figure 1.5). However, the German mathematician M. Wilhelm Kutta made the first observation in 1902 that for a steady flow around an airfoil, the flow leaves smoothly the top and bottom surfaces of the airfoil at the trailing edge (Anderson, 2001). From this observation, the Kutta condition was derived so that the circulation $\Gamma$ would correspond to a more natural flow physics. The Kutta condition is summarized as follows (Anderson, 2001) :

— For a given airfoil, the circulation around the body $\Gamma$ is such that the flow leaves smoothly the trailing edge
— If the trailing edge angle is finite, it is a stagnation point
— If the trailing edge is cusped, then the velocities leaving the top and bottom surfaces at the trailing edge are finite and equal in magnitude and direction (Figure 1.6)

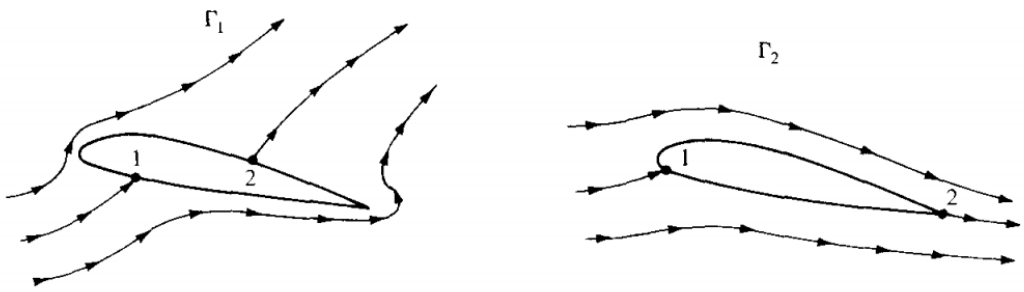


Figure 1.5 Effect of different values of circulation on the potential flow over a given airfoil. Points 1 and 2 are stagnation points (Source : Anderson (2001)).

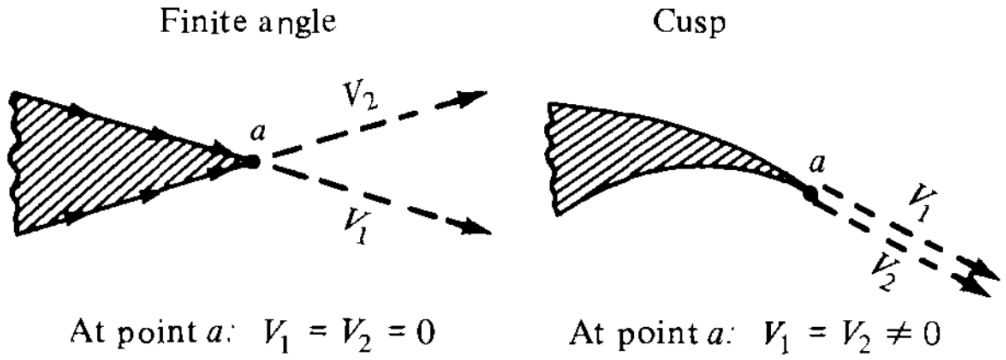


Figure 1.6 Kutta condition (Source : Anderson (2001)).

### 1.2.2 Viscous-Inviscid Coupling Methods

Ignoring viscous effects simplifies greatly the resolution of the fluid motion, but these viscous effects cannot be ignored for aircraft design. Therefore, many developments have been done to couple inviscid methods with boundary-layer (BL) equations. This led to the development of codes based on the Euler equations coupled with boundary-layer equations like MSES(Drela, 2007) or CART3D(Aftosmis and Cliff, 2011). Coupling approaches using full potential methods with boundary-layer equations were also developed and used in industry like KTRAN(Kafyeke and Robin, 1988). The same was also performed with linear potential flow methods using a panel method with BL equations like VSAERO(Maskew, 1987) and is still used today in the industry. Finally, the viscous effect can also be incorporated using high fidelity 2D RANS sectional data with lifting-line methods (Tani, 1934; Van Dam, 2002; Mukherjee *et al.*, 2003; Gallay, 2016). It allows a fast turnaround time with the possibility to capture viscous effects like stall. These methods are of great interest for conceptual design.

Table 1.1 3D CFD methods comparison (Adapted from Mariens (2012)).

| | **RANS** | **Euler** | **Full Potential** | **Panel Method** | **Vortex Lattice Method** |
|---|---|---|---|---|---|
| **Governing Equations** | RANS Equations | Euler Equations | Full Potential Flow | Linearized Potential Flow | Linearized Potential Flow |
| **Viscosity** | Yes | No | No | No | No |
| **Compressibility** | Yes | Yes | Yes | No (possible with compressibily corrections) | No(possible with compressibily corrections) |
| **Lift Coefficient** | Yes | Yes | Yes (with Kutta Condition) | Yes (with Kutta Condition) | Yes (with Kutta Condition) |
| **Shockwave Prediction** | Yes | Yes | Yes (Inacurate for strong shocks) | No | No |
| **CPU Time(Jameson, 2004)** | Multiple Days | 1 - 15 hrs. | 5 min. - 1 hr. | 1 min. - 15 min. | 5 sec. - 1 min. |

## 1.3 Elements of the Problematics

### 1.3.1 Aerodynamic Tools

As presented previously, there are many different methods to perform aerodynamic analysis for a wide range of computation costs and fidelity for both the geometry and the flow physics.

Table 1.2 and Figure 1.7 shows the typical aerodynamic tools use from the conceptual design phase to the detailed design phase of an aircraft. Usually, the conceptual design is owned by the advanced design department where low-fidelity and semi-empirical methods are favored for their fast turnaround time(Piperni and Deblois, 2013). The aerodynamic topology is fixed before entering the preliminary phase where higher fidelity tools like 3D RANS are used to complete the aerodynamic design. These two design phases are crucial for the aircraft aerodynamic performances and they are owned by two different departments with different sets of tools.

There is a need for an aerodynamic tool with low computation costs that can be implemented inside a conceptual design framework but with higher fidelity comparable to 3D RANS flow solver that could also support the preliminary design analysis. This is particularly important for high-lift design where the topology is fixed during the conceptual phase with low-fidelity methods and further developed in the preliminary design phase with high-fidelity methods requiring important efforts to prepare and perform the aerodynamic analysis.

Table 1.2 Aerodynamic tools for aircraft design

| **Task** | **Conceptual Design** | **Preliminary Design** | **Detailed Design** |
|---|---|---|---|
| **Owner (Department)** | Adavanced Design | Advanced Aerodynamics | Advanced Structures |
| **Function** | Aircraft-level design | Aerodynamic-lines at fixed topology | Structural design at fixed external geometry |
| **Tools** | Low-fidelity, semi-empirical | High-fidelity aerodynamic models | High-fidelity structurual models |
| **Aerodynamics** | Reduced-order models, 3D Linear aerodynamics | Non-linear 3D RANS steady flows | Non-linear 3D FEM, Frequency-domain 6-DOF |
| | ⟵ **Aerodynamic tool for both conceptual and preliminary design ?** ⟶ | | |

### 1.3.2 Multi-Disciplinary Optimization (MDO)

Complex trade studies are performed during the conceptual and preliminary aircraft design phases. The tradeoff often requires the interaction of many disciplines and was traditionally accomplished with semi-empirical and knowledge-based methods. MDO frameworks in aircraft design are now involving more and more disciplines to arrive at superior designs.

As mentioned by Rizzi (2011), most of the life-cycle cost comes from the decision made during the conceptual phase where difficulties arise from complex tradeoffs and the use of low fidelity tools. MDO is now present in all design phases (Figure 1.7), but it still remains a challenge in terms of implementation.

In a conceptual multi-disciplinary design optimization (CMDO) framework, the number of design variables remains low and the optimization is oriented towards the exploration of the design space (Piperni and Deblois, 2013). A stochastic optimizer is often used at this stage with both single-objective and multi-objective functions and requires thousand of function evaluations to converge toward an optimum. Fast turnaround aerodynamic tools are then necessary. Furthermore, the quality of the optimal solution found is directly dependent on the precision of the function analysis, mainly the aerodynamic solver.

Therefore, there is a need in the aircraft design community to develop and implement fast efficient CMDO framework with higher fidelity components.

| MDO Level | Fidelity | Aerodynamics | Structures | Propulsion |
|---|---|---|---|---|
| CMDO | L0 | Knowledge-based aerodynamics | Knowledge-based weight prediction | Fixed architecture, scaled engine model |
| | L1 | Quasi-3D methods (3D VLM / Panel method + 2D High-Fidelity CFD) | Beam or thin-shell models | Variable architecture, generic rubber engine |
| | L1.5 | Disciplinary L2 Surrogate Models | | Surrogate model(s) from Engine supplier(s) |
| PMDO | L2 | Mid-to-High Fidelity CFD (3D TSD to RANS) | Global FEM | Real engine model (fixed) |
| | L2.5 | Disciplinary L3 Surrogate Models | | |
| DMDO | L3 | RANS | Detail FEM | |

[a]CFD = computational fluid dynamics; 3-D = three-dimensional; 2-D = two-dimensional; VLM = vortex-lattice method; RANS = Reynolds-averaged Navier–Stokes simulation; FEM = finite element method.

Figure 1.7 MDO levels and tool sets (Source : Piperni and Deblois (2013))

## 1.4 Research Objectives

The overarching goal of the current project is to develop an aerodynamic tool suitable for conceptual multi-disciplinary design optimization with low computational cost and sufficient fidelity to explore a large design space. To ensure low computational costs, the aerodynamic solver chosen is a Vortex Lattice Method based on the linear potential flow equation coupled with 2.5D RANS sectional data to incorporate viscous and compressible effects for higher fidelity. From this, the following objectives are formulated :

1. Assess the fidelity of a Vortex Lattice Method coupled with 2.5D RANS approach for high-lift design with comparison to 3D RANS solutions ;
2. Explore the various optimization problems and the level of complexity and accuracy that can be achieved using a VLM coupled with 2.5D RANS approach :
   (a) Make use of the non-linearity of the VLM/2.5D approach to introduce a new stall criteria as an optimization constraint ;
   (b) Perform multi-topology optimization cases ;

## 1.5 Plan of Thesis

The thesis is divided into three main chapters : literature review, aerodynamic solver and optimization. The literature review covers the theory of the lifting-line method and its derivation to the Vortex Lattice Method. Different coupling methods with 2D RANS sectional data are reviewed and explained. The last part is a review of known conceptual design optimization tools using linear potential flow.

Chapter three focuses on the implementation of an *alpha-based* coupling algorithm for 2D and 2.5D RANS sectional data with a Vortex Lattice Method. The coupling algorithm is derived and explained in the first section with the infinite swept wing theory used to obtain 2.5D RANS data and how they capture crossflow effects. The last section of this chapter is a verification of the method and its precision compared to high fidelity 3D RANS solutions performed with Bombardier's 3D RANS flow solver. We notably focus on the sweep corrections.

Chapter four covers the implementation of the VLM/RANS approach inside an optimization framework using a well-known Covariant Matrix Adaptation Evolution Strategy (CMA-ES) optimizer. Results of many single-objective and multi-objective optimizations are presented for low-speed and high-speed conditions with high-lift configuration as well.

# CHAPTER 2 LITERATURE REVIEW

## 2.1 Lifting-Line Method

Ludwig Prandtl developed a practical theory to estimate the lift coefficient of finite wings, known as Prandtl's Lifting-Line Theory (LLT). The theory is still used today for a quick estimation of wings aerodynamic characteristics.

The finite wing is replaced by a bound vortex and due to Helmholtz's theorem, the vortex filament cannot end in the fluid. Thus, the vortex filaments are turned and shed downstream as two trailing vortices in the shape of a horseshoe vortex (Figure 2.1). The bound vortex induces no velocity on itself. The induced velocity comes from the trailing vortices and by using the Biot-Savart Law (Equation 2.1), the induced angle of attack at any point along the span is represented by Equation 2.2.

$$dV = \frac{\Gamma}{4\pi}\frac{dl \times r}{|r|^3} \tag{2.1}$$

$$\alpha_i(y_0) = \frac{1}{4\pi U_\infty}\int_{-b/2}^{b/2}\frac{(d\Gamma/dy)dy}{y_0 - y} \tag{2.2}$$

Therefore, the lift coefficient at $y = y_0$ can be defined in terms of effective angle of attack ($\alpha_{eff}(y_0) = \alpha - \alpha_i(y_0)$) :

$$Cl = a_0[\alpha_{eff}(y_0) - \alpha_{L=0}] = 2\pi[\alpha_{eff} - \alpha_{L=0}] \tag{2.3}$$

where $2\pi$ is the thin airfoil theory lift curve slope and $\alpha_{L=0}$ the angle of zero lift. By using the relation of lift with circulation (Kutta-Joukowski), Equation 2.2 can be rewriten into the classical Prandtl's integro-differential equation :

$$\alpha(y_0) = \frac{\Gamma(y_0)}{\pi U_\infty c(y_0)} + \alpha_{L=0}(y_0) + \frac{1}{4\pi U_\infty}\int_{-b/2}^{b/2}\frac{(d\Gamma/dy)dy}{y_0 - y} \tag{2.4}$$

If the following transformation is considered :

$$y = -\frac{b}{2}\cos\theta \tag{2.5}$$

and the lift distribution represented by a Fourier series, then the circulation $\Gamma$ distribution

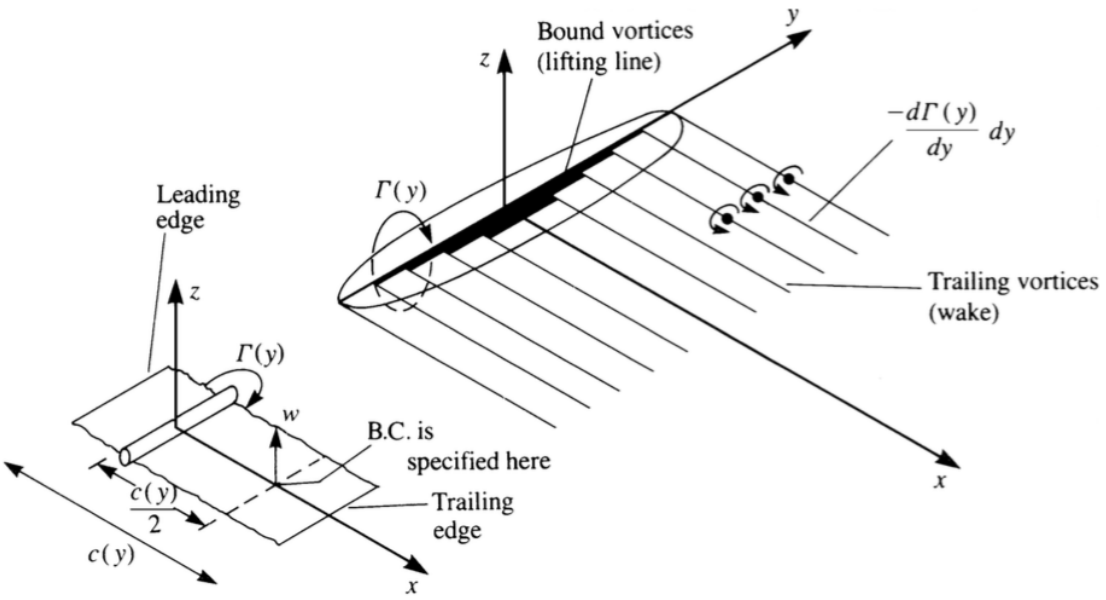


Figure 2.1 Lifting-line model consisting of horseshoe vortices. The bound vortex segment of all vortices is placed on the y axis (Source : (Katz and Plotkin, 2001)).

along the span is :

$$\Gamma(\theta) = 2bU_\infty \sum_{1}^{N} A_n \sin n\theta \tag{2.6}$$

The wing can be represented by as many terms N as necessary for precision and the transformation allows the integral of Equation 2.4 to be easily evaluated. The lifting-line method of Prandtl provides good results for incompressible and attached flows. However, it is limited to wings with aspect ratio higher than four and without sweep. This is an important limitation for wing design purposes.

In his theory, Prandtl made the assumption of a linear relation between the section lift and the section angle of attack. This assumption fails with swept wings. A modern adaptation of the lifting-line theory has been proposed by Phillips and Snyder (2000) where the general lifting vortex law (Saffman, 1992) is used and allows wings with sweep and dihedral angle to be modeled (Figure 2.2). This adaptation is equivalent to the *Finite Step Method* (Blackwell, 1969; Weissinger, 1947) and forms the basis of the Vortex Lattice Method.

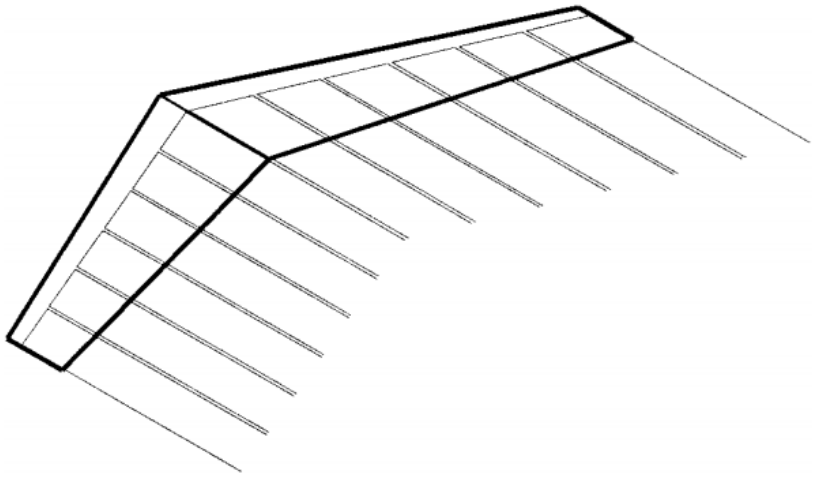

Figure 2.2 Horseshoe vortices distributed along the quarter chord of a finite wing with sweep and dihedral (Source : Phillips and Snyder (2000)).

## 2.2 Potential/RANS Coupling Methods

The idea behind Potential/RANS coupling methods is to introduce viscous effects into inviscid methods. The viscous effects are incorporated by sectional data coming from either wind tunnel of two-dimensional CFD simulations. These coupling methods fall into two categories, $\Gamma$ method and $\alpha$ method.

### 2.2.1 $\Gamma$ Method

An attempt to couple an inviscid method with viscous data was made by Tani (1934). A typical $\Gamma$ coupling algorithm, where the coupling variable is the circulation, is presented by Algorithm 1. Interesting results were produced by Sivells and Neely (1947) using a $\Gamma$ method compared to experimental data for a symmetrical lift distribution. However, the method is limited by the lifting-line theory and is only applicable to straight unswept wings. The same $\Gamma$ method is also presented by Anderson (2001), but one issue is the low relaxation factor required to achieve convergence (Gallay, 2016). Moreover, Sears (1956) demonstrated the non-uniqueness of Prandtl's lifting-line equation when the lift curve slope becomes negative, mainly in post-stall conditions. Therefore, a $\Gamma$ method fails at stall. However, it is possible to add artificial viscosity in the viscous correction to ensure a unique solution in post-stall conditions (Chattot, 2004).

**Algorithm 1** $\Gamma$ method

1: Assume a lift distribution (i.e. Elliptical distribution)
2: Calculate the induced angle of attack for each section using :
$\alpha_i(y_n) = \frac{1}{4\pi V_\infty} \int_{-b/2}^{b/2} \frac{(d\Gamma/dy)dy}{y_n - y}$
3: **for** Every Span-Wise Section $i$ **do**
4: Interpolate the sectional viscous lift at the effective angle of attack :
$\alpha_e(i) = \alpha(i) - \alpha_i(i) \Rightarrow Cl_{viscous}(\alpha_e(i))$
5: Calculate the new circulation distribution using the Kutta-Joukowski theorem :
$\Gamma_{new}(i) = \frac{1}{2} V_\infty c Cl_{viscous}(\alpha_e(i))$
6: Update the local circulation with a relaxation factor $\beta$ :
$\Gamma(i) = \Gamma_{old} + \beta(\Gamma_{new} - \Gamma_{old})$
7: **end for**
8: Repeat steps 2-7 until $|\Gamma_{new} - \Gamma_{old}| < \epsilon$

### 2.2.2 $\alpha$ Method

Later on, $\alpha$ methods were developed by Tseng and Lan (1988) with the coupling variable being the local angle of attack instead of the local circulation $\Gamma$. Van Dam (2002) has demonstrated the use of an $\alpha$ method with a *Finite Step Method* of Weissinger (1947) for high-lift design. The results presented was in good agreement with experimental data with $C_{L_{max}}$ well captured. The $\alpha$ method used by Van Dam (2002) is presented in Algorithm 2. The viscous lift curve slope ($Cl_{\alpha v}$) is used to update the local angle of attack and therefore the collocation point is modified so the local inviscid lift curve slope is equal to the viscous lift curve slope. Issues arise with this method at the stall point where the viscous lift curve slope is equal to zero.

**Algorithm 2** Van Dam $\alpha$ method (Van Dam, 2002)

1: Solve the *Finite Step Method* to calculate $Cl_{inviscid}$
2: **for** Every Span-Wise Section $i$ **do**
3: Calculate the effective angle of attack :

$$\alpha_e(i) = \frac{Cl_{inviscid}(i)}{Cl_{\alpha v}} - \alpha_{2D}(i) + \alpha_{3D} \tag{2.7}$$

4: Interpolate the viscous lift at the effective angle of attack :
$\alpha_e(i) \Rightarrow Cl_{visc}(\alpha_e(i))$
5: Calculate the angle of attack corection :
$\alpha_{2D}(i) = \alpha_{2D}(i) + \frac{Cl_{visc}(\alpha_e(i)) - Cl_{inviscid}(i)}{Cl_{\alpha v}}$
6: **end for**
7: Repeat Steps 1-6 until $|Cl_{visc} - Cl_{inviscid}| < \epsilon$

Mukherjee *et al.* (2003) have developed a modified $\alpha$ method where the viscous moment coefficient is also used to calculate the effective angle of attack. The method relies on a decambering approach using thin airfoil theory. Two decambering functions are used and solved with a Newton scheme to calculate the local decambering at each section. Their method shows great results for both lift and moment coefficients. They also demonstrate the non-uniqueness of the solution in post-stall conditions depending on the residual scheme used to solve the local decambering.

More recently, Gallay and Laurendeau (2015; 2016) revisited the $\alpha$ method of Van Dam using a VLM (Katz and Plotkin, 2001) and a *Finite Step Method* of Blackwell (1969). Instead of using the viscous lift curve slope to update the local angle of attack, thin airfoil theory lift curve slope of $2\pi$ is used and the collocation point is modified at high angles of attack to ensure a local inviscid slope of $2\pi$. The non-uniqueness of the solution in post-stall conditions was also demonstrated in his work that confirmed the observation of Spalart(2014) concerning spontaneous stall cells appearance in stall regime using a periodic lifting-line method. With a modification made to the artificial viscosity formulation of Chattot (2004), Gallay and Laurendeau (2015) presented a strongly-coupled scheme to apply local viscous corrections. The non-linear system is solved with a Newton-Raphson scheme and shows better convergence rate compared to the loosely-coupled scheme used in the previous methods. Estimation of aerodynamic coefficients for high-lift configurations was also investigated by Gallay and Laurendeau (2016) where different multi surfaces in the inviscid code were tested, planform with/without gap or clean planform only (Figure 2.3). They found that the results are very

similar between the different mesh configurations for $C_L$, $C_D$ and $C_M$, so only the clean configuration can be modeled by the VLM. The reason is that the complex flow physics is incorporated by the viscous data.

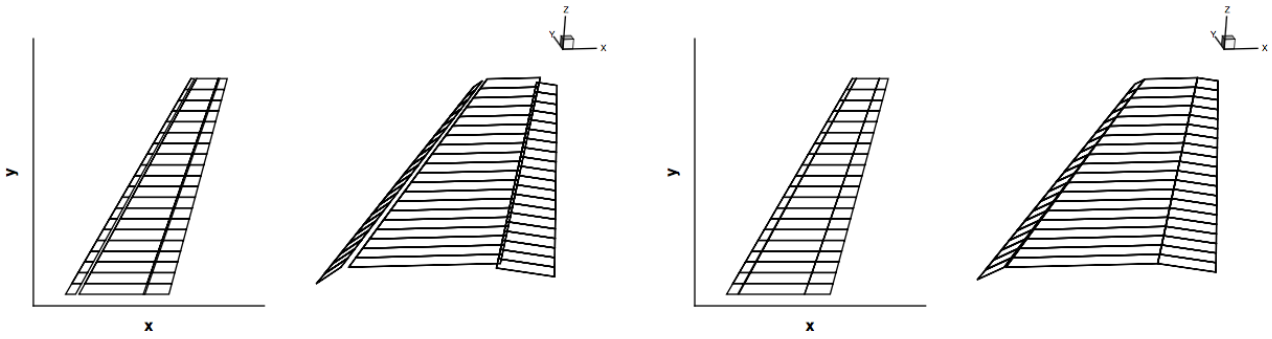


Figure 2.3 Multi surfaces mesh for the inviscid code, with gap (left) our without gap (right) between the elements (Source : Gallay *et al.* (2014)).

An important contribution of Gallay and Laurendeau's work is the use of 2.5D RANS to generate the sectional viscous data (Gallay *et al.*, 2014; Gallay and Laurendeau, 2016). A 2D RANS flow solver is extended for infinite swept flows to capture the crossflow effects on the boundary-layer over swept wings (Bourgault-Cote *et al.*, 2017). Since the solver remains two-dimensional, computing sectional data remains as fast and viscous crossflow effects are captured. The use of 2.5D RANS sectional data allows a better prediction of $C_{L_{max}}$. Aerodynamic coefficients calculation in transonic conditions is also improved because oblique shocks are captured with the infinite swept wing condition.

## 2.3 MDO Based on Linear Potential Aerodynamic Solver

Different approaches have been tested to perform aerodynamic design optimization using lifting-line methods with viscous correction applied from experimental data or viscous airfoil solutions. Using quasi-three-dimensional solvers allow fast turnaround time to explore a wide range of design space with relatively low computational time.

Wilcox and Wakayama (2003) used a VLM for a multi-disciplinary design optimization for a family aircraft. The VLM is coupled with experimental data and empirical methods to evaluate the maximum lift coefficient. The low computational cost of the VLM allows more than 20 design cases to be evaluated at each iteration of the optimization.

A quasi-three-dimensional solver with fast turnaround time was developed by Hilemana *et al.* (2010) to fully explore the design space for aircraft optimization with noise reduction and fuel

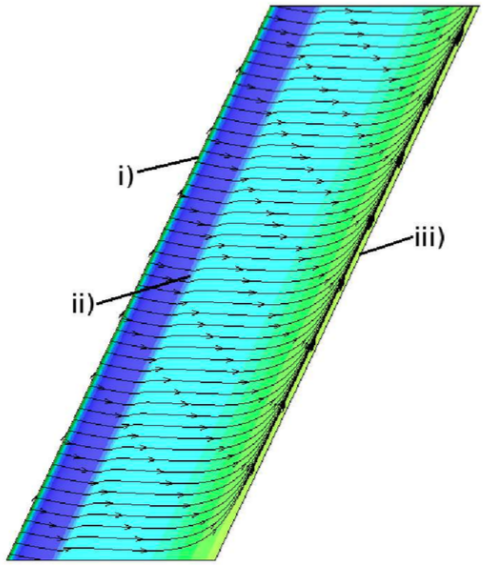


Figure 2.4 Physical effects captured by infinite swept wing RANS solution : i) stagnation region, ii) shock waves, iii) trailing-edge region (Source : Gallay *et al.* (2014)).

efficiency as objective functions. The quasi-three-dimensional solver consists of a 2D VLM with sectional viscous airfoil data and empirical drag estimates.

Another quasi-three-dimensional solver was developed by Mariens *et al.* (2014) to perform MDO of lifting surfaces. A Vortex Lattice Method is used to calculate the local lift coefficient and strip theory with simple sweep theory is then used to find the local aerodynamic characteristics, which are then used as an input to an airfoil analysis tool to obtain viscous drag. The airfoil analysis tool is either a coupled Euler/Boundary layer method (MSES (Drela, 2007)) or a full potential solver integrated with a boundary layer solver (VGK (Society, 1996)). The aircraft maximum take-off weight (MTOW) is considered as the objective function. The optimization results showed a reduction of 2.95% in aircraft MTOW.

The same quasi-three-dimensional solver of Mariens *et al.* (2014) was used to perform design optimization of winglets (Elham and van Tooren, 2014). A multi-objective genetic algorithm is used to find the Pareto front (Figure 2.5) for two objective functions, minimum wing drag and minimum wing weight. The results of the optimization estimated 3.8% reduction in fuel weight.

More recently, the quasi-three-dimensional solver of Mariens *et al.* (2014) was used with a combination of Adjoint method and chain rule for differentiation to compute the sensitivities of drag with respect to the design variables (Elham, 2015). The quasi-three-dimensional solver is used to compute the derivatives and drag while a higher fidelity method calibrates

the solution from the quasi-three-dimensional solver. The idea is to use the low computational time of the Q3D solver to compute the derivatives to accelerate the convergence toward the optimum of the higher fidelity tool.

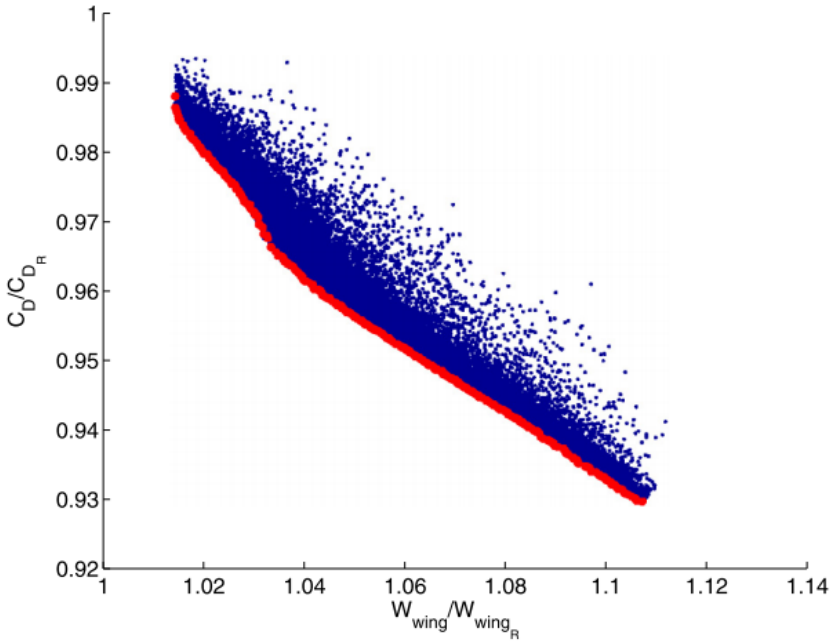


Figure 2.5 Pareto front for the wing structural weight and the wing drag for Fokker 100 aircraft (Source : Elham and van Tooren (2014)).

Linear potential methods offer an interesting approach for MDO with their fast turnaround time and complex flow physics can be incorporated by two-dimensional RANS solutions with a coupling algorithm based on the alpha method.

# CHAPTER 3 VLM COUPLED WITH 2.5D RANS APPROACH

The Vortex Lattice Method is chosen as the basis of the aerodynamic solver for its simplicity of representing complex wing geometries by a single planform and its low computation time. The fast turnaround time of the method is essential since multi-disciplinary design optimization is intended with a stochastic optimizer that requires many function evaluations to converge to an optimum.

## 3.1 Vortex Lattice Method

The VLM is implemented following the description in Katz and Plotkin(2001) where the wing is represented by a lattice of vortex rings (Figure 3.1). The bound vortices are placed

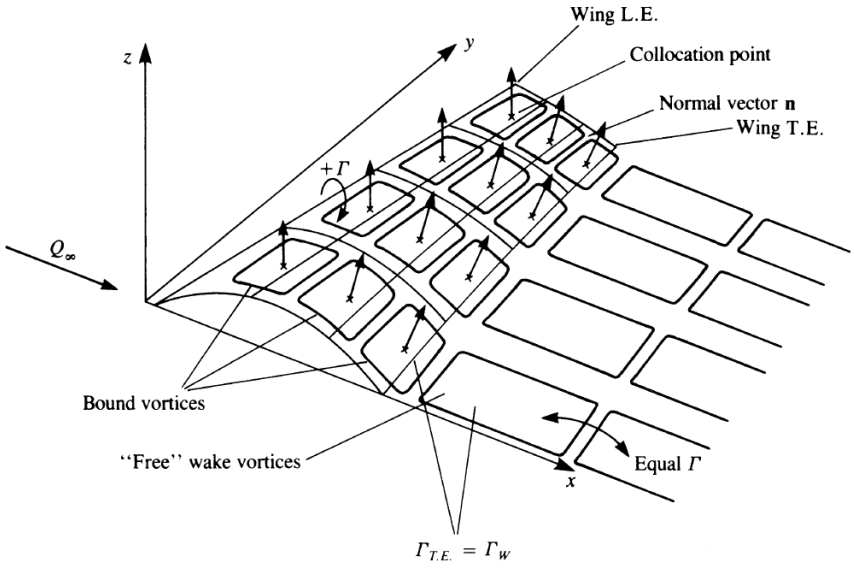


Figure 3.1 Representation of thin lifting surfaces (Source : Katz and Plotkin (2001)).

on the wing panel's 1/4 chord and the Neumann boundary condition of no penetration is enforced at the collocation point located at the 3/4 chord of the wing's panel. This is referred to as the 1/4-3/4 rule and it is a fundamental concept for Vortex Lattice Methods derived by Pistolesi(1937). By using a single panel vortex lattice in two-dimension (Figure 3.2), he found that by placing the vortex point at the 1/4 chord and the boundary condition at the 3/4 chord, the section lift curve slope corresponds exactly to the thin airfoil theory ($2\pi$). **However, this is only true with the assumption of small angles of attack**.

The velocity induced $U$ at a distance $r$ from a vortex placed at c/4 with the boundary condition is represented by :

$$U = U_\infty sin(\alpha) = \frac{\Gamma}{2\pi r} \tag{3.1}$$

with Kutta-Joukowski formulation of lift and thin airfoil theory, but without assumption of small angles :

$$\frac{1}{2}\rho U_\infty^2 c 2\pi\alpha = \rho U_\infty \Gamma = \rho U_\infty 2\pi r U_\infty sin(\alpha) \tag{3.2}$$

$$\frac{1}{2} c 2\pi\alpha = 2\pi r sin(\alpha) \tag{3.3}$$

$$r = \frac{1}{2}\frac{\alpha}{sin(\alpha)} \tag{3.4}$$

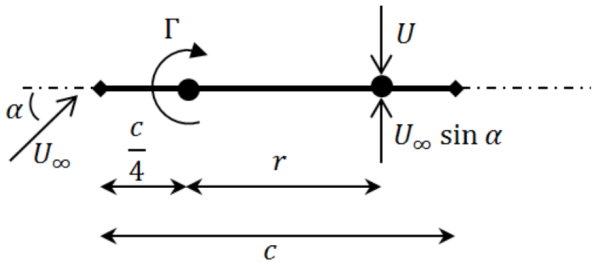


Figure 3.2 Control point and vortex location (Source : Gallay (2016)).

Therefore, the collocation point must be corrected at high angles of attack to maintain a local lift curve slope of $2\pi$. After the collocation point is calculated, the influence of each vortex rings on each other is evaluated using the Biot-Savart Law and assembled into an influence matrix $A$. The boundary condition is incorporated in the right-hand side and the linear system is solved for the unknown circulation $\Gamma$ (Equations 3.5).

$$\begin{pmatrix} A_{1,1} & A_{1,2} & \cdots & A_{1,m} \\ A_{2,1} & A_{2,2} & \cdots & A_{2,m} \\ \vdots & \vdots & \ddots & \vdots \\ A_{m,1} & A_{m,2} & \cdots & A_{m,m} \end{pmatrix} \begin{pmatrix} \Gamma_1 \\ \Gamma_2 \\ \vdots \\ \Gamma_m \end{pmatrix} = \begin{pmatrix} RHS_1 \\ RHS_2 \\ \vdots \\ RHS_m \end{pmatrix} \tag{3.5}$$

$$RHS_K = \Big(U,V,W\Big)_\infty \cdot n_K \tag{3.6}$$

The Vortex Lattice Method only models inviscid, incompressible and attached flows. Therefore, we include sectional data computed with two-dimensional RANS solutions in order to incorporate non-linear effects such as flow separation.

### 3.2 Coupling Algorithm

The coupling algorithm used is derived from Van Dam(2002) with the only difference being the lift curve slope used to update the local angle of attack. The collocation point is adjusted according to the local angle of attack as derived previously in Equation 3.4 to ensure a local lift curve slope of $2\pi$. The VLM with viscous correction is referred to as Non-Linear VLM (NL-VLM). To better understand the coupling scheme, Figure 3.3 shows how the local effective angle of attack is calculated. Using the thin airfoil theory, the local inviscid lift coefficient is evaluated as follow :

$$Cl_{inviscid} = 2\pi(\alpha - \Delta\alpha - \alpha_i) \tag{3.7}$$

where $\alpha$ is the geometric angle of attack, $\alpha_i$ is the induced angle of attack by the downwash and $\Delta\alpha$ is the viscous correction. Using the definition of the lifting-line theory for the effective angle of attack :

$$\alpha_e = \alpha - \alpha_i \tag{3.8}$$

Equation 3.7 can be arranged as follow :

$$\alpha_e = \frac{Cl_{inviscid}}{2\pi} + \Delta\alpha \tag{3.9}$$

Finally, $\Delta\alpha$ is the difference between the geometric angle of attack($\alpha_{3D}$) and the local angle of attack($\alpha_{2D}$). Thus, the complete formulation of the local effective angle of attack is expressed as follow :

$$\alpha_e = \frac{Cl_{inviscid}}{2\pi} - \alpha_{2D} + \alpha_{3D} \tag{3.10}$$

Equation 3.10 is used to evaluate iteratively the local effective angle of attack. The viscous lift coefficient is then interpolated from the RANS solutions at the corresponding effective angle of attack. A correction on the local angle of attack ($\alpha_{2D}$) is calculated from the difference between the viscous and the inviscid lift until a solution is found where the local viscous lift is equal to the local inviscid lift. The right hand side of the linear system (Equation 3.5) is then updated with the new local angle of attack $\alpha_{2D}$ and the collocation point is also recalculated with $\alpha_{2D}$. This coupling algorithm is resumed in Algorithm 3.

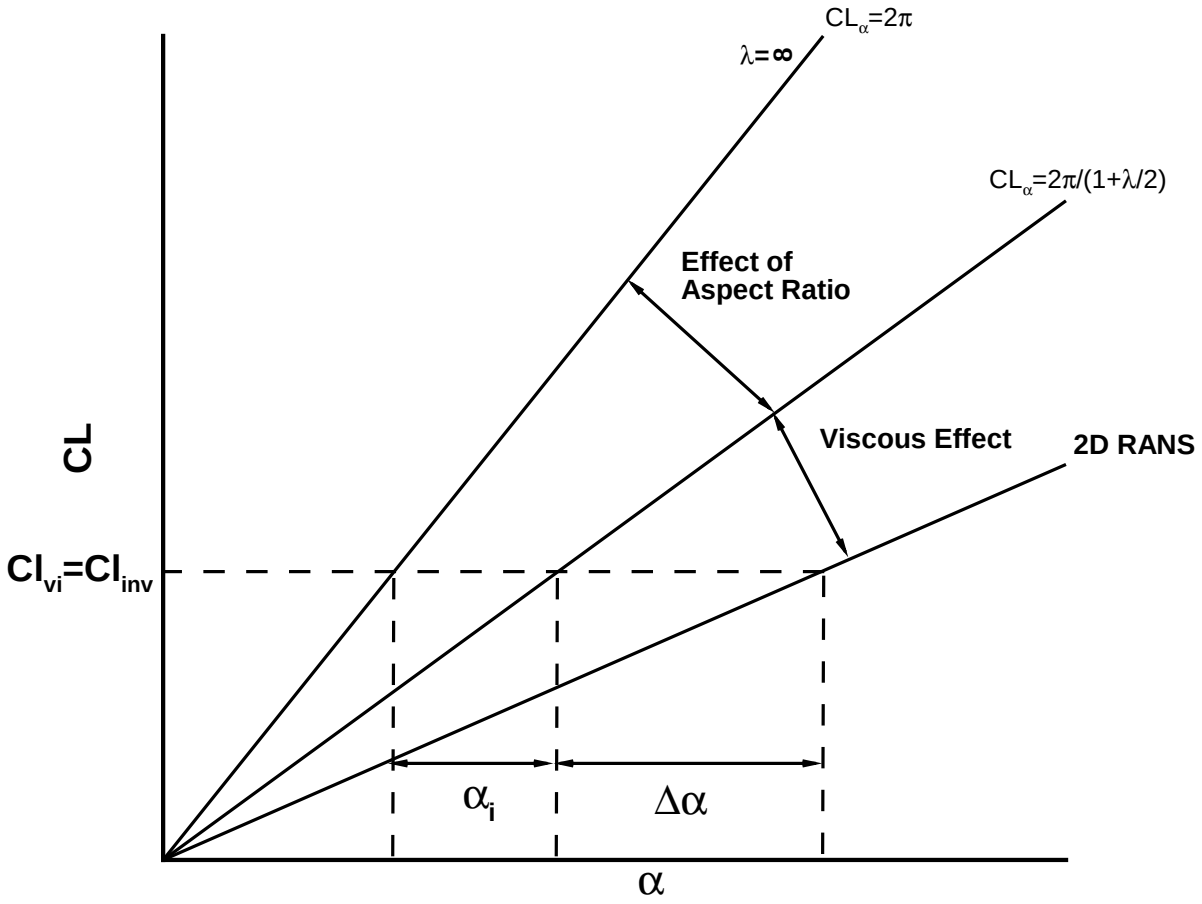


Figure 3.3 Coupling algorithm.

**Algorithm 3** Van Dam modified $\alpha$ method

1: Solve the VLM to calculate $Cl_{inviscid}$
2: **for** Every Span-Wise Section $i$ **do**
3: Calculate the effective angle of attack :

$$\alpha_e(i) = \frac{Cl_{inviscid}(i)}{2\pi} - \alpha_{2D}(i) + \alpha_{3D}$$

4: Interpolate the viscous lift at the effective angle of attack :
$\alpha_e(i) \Rightarrow Cl_{visc}(\alpha_e(i))$
5: Calculate the angle of attack corection :
$\alpha_{2D}(i) = \alpha_{2D}(i) + \frac{Cl_{visc}(\alpha_e(i)) - Cl_{inviscid}(i)}{2\pi}$
6: **end for**
7: Repeat Steps 1-6 until $|Cl_{visc} - Cl_{inviscid}| < \epsilon$

### 3.3 Forces Calculation

After the system is converged to a final solution of circulation $\Gamma$, the total lift is evaluated by summing the incremental lift force of each panel with the Kutta-Joukowski theorem as follows :

$$F = \sum_{i=1}^{N} \rho_\infty \Gamma_i (U_\infty \times dl) \tag{3.11}$$

where $dl$ is the bound vortex filament. The lift force is calculated with the VLM while the drag estimation is divided into two contributions, induced drag and viscous drag.

$$D_{total} = D_{induced} + D_{viscous} \tag{3.12}$$

The induced drag is calculated by integrating the kinetic energy far behind the lifting body in a plane normal to the freestream called the Trefftz plane (Figure 3.4). For a lifting-line method, the surface integral can be transferred to a spanwise line integral over the wake trailing vortices as follows :

$$D_{induced} = -\frac{\rho_\infty}{2} \int_{-b/2}^{b/2} \Gamma(y) w dy \tag{3.13}$$

where $w$ is the induced velocity of the trailing vortices in the Trefftz plane. This method is found to be accurate and robust for optimization purposes. On the other hand, the viscous drag is calculated from the sectional RANS data and includes the friction and pressure

drag. For each section spanwise, the viscous drag coefficient is interpolated from the local RANS data values at the corresponding effective angle of attack calculated by the coupling algorithm. A spanwise integration is then performed to obtain the total viscous drag

$$D_{viscous} = \frac{1}{2}\rho_\infty U_\infty^2 \int_{-b/2}^{b/2} C_{D_{viscous}} c dy \tag{3.14}$$

where $c$ is the local chord length. The 3D pitching moment is also evaluated by a similar spanwise integration of the local pitching moment. The center of pressure for every spanwise section is evaluated using the local viscous lift and viscous drag interpolated at the corresponding effective AoA. The pitching moment relative to the 3D wing reference point is then computed and integrated spanwise as follow :

$$x_{cp} = \frac{(C_{m_{c/4}})_{visc}}{C_{l_{visc}}} \tag{3.15}$$

$$C_{m_{x_{ref}}} = \left[C_{l_{visc}} \cos(\alpha_e) + C_{d_{visc}} \sin(\alpha_e)\right] \frac{x_{ref} + x_{cp}}{c} \tag{3.16}$$

$$M_{x_{ref}} = \frac{1}{2}\rho_\infty U_\infty^2 \int_{-b/2}^{b/2} C_{m_{x_{ref}}} c^2 dy \tag{3.17}$$

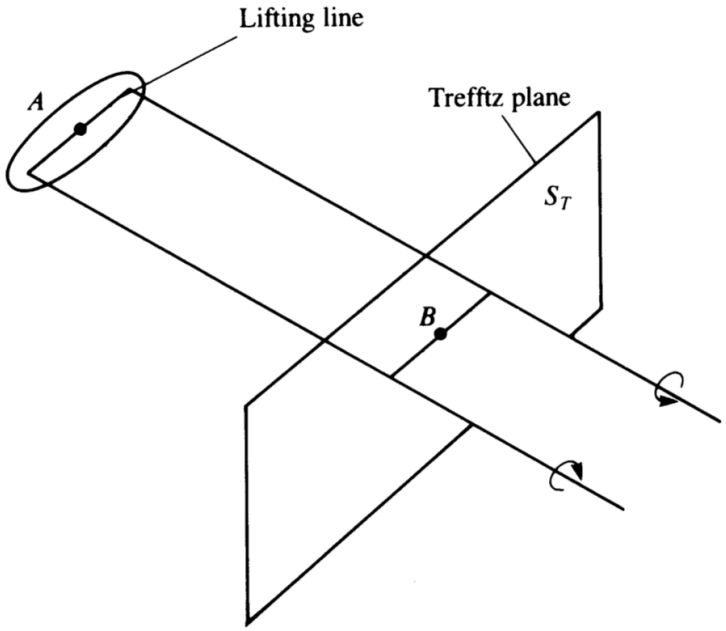


Figure 3.4 Trefftz plane used for induced drag calculation (Source : Katz and Plotkin (2001)).

### 3.4 Numerical Implementation

The goal is to develop a tool for aerodynamic analysis for conceptual design. The flexibility of the tool is then necessary to allow complex geometries to be easily modeled and analyzed. Therefore, the tool was implemented in C++ to take full advantage of the language object-oriented capabilities to obtain a modular code. The *Boost Python* library was also used to extend the C++ classes to Python and allow direct access to the constructors. Instead of having complex input files, the problem is build dynamically inside a Python script. Therefore, large problems can then easily be built with any number of lifting surfaces. An example Python script is available in Appendix B.

The other concern is the computation cost of the method. Even though a Vortex Lattice Method has a fast turnaround time by default, it is necessary to minimize as much as possible the computation time because the code is intended to be used with a stochastic optimizer where thousands of function evaluations are necessary to converge towards an optimum.

The main computation effort for a Vortex Lattice Method is in the influence matrix calculation and solving the linear system. The computation time of the matrix grows exponentially with the number of panels. To reduce the calculation time, the influence matrix evaluation is performed in parallel with *OpenMP*. *For loops* can be executed in parallel with a single directive without changing the code's structure.

Additionally, the linear system is solved using a biconjugate gradient stabilized method (BiCGSTAB(Vorst, 1992)). BiCGSTAB is an iterative Krylov subspace method with fast convergence rate. BiCGSTAB is more efficient than direct methods like Gaussian elimination for large dense and non-symmetric linear systems.

Finally, the precision of the viscous lift coefficient interpolation performed in the coupling algorithm is crucial for a good estimation of the maximum lift coefficient. Therefore, an Akima spline is built over the viscous database to achieved the desired accuracy for $C_{L_{max}}$ evaluation. The Akima spline was chosen for its stability when a neighboring point is far from the others as opposed to a cubic spline that could oscillate.

### 3.5 Verification Results

The accuracy of the method is investigated and compared to 3D RANS solutions. The effect of 2.5D RANS sectional data is also investigated using three different sweep lines (leading edge, quarter-chord and half-chord). All the simulations are performed on the isolated Bombardier Research Wing (BRW) in low-speed conditions (Figure 3.5). In order to reduce numerical

errors, both the 3D RANS and 2D/2.5D RANS sectional data were generated with Bombardier's unstructured RANS flow solver DRAGON(Yang and Langlois, 2015) and with the same turbulence model, Wilcox $k-\omega$ . The clean configuration is analyzed first and then with three different flap deflections (10°, 20° and 30°). 2D and 2.5D RANS calculations are performed for the various sections along the span presented in (Figure 3.5) to generate the viscous database.

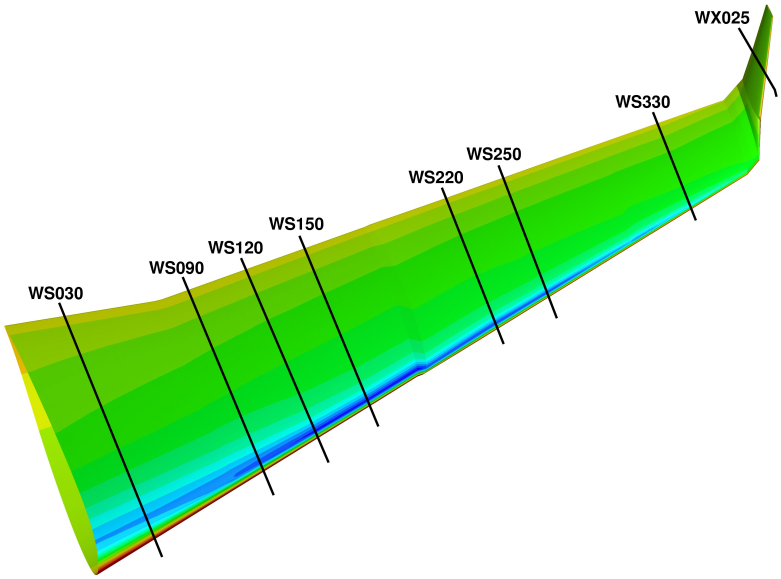


Figure 3.5 BRW - Section cuts used for 2D RANS calculations.

### 3.5.1 3D Solution Reconstruction

In order to compare chordwise pressure distribution along the span with the 3D RANS solutions, the two-dimensional RANS pressure solutions are used to reconstruct the 3D wing surface pressure. The VLM solution is used to find the effective angle of attack at each of the section cuts of Figure 3.5. Afterward, the two-dimensional RANS pressure coefficients are interpolated at the corresponding $\alpha_e$ and the 3D wing is generated by transfinite interpolation from the interpolated 2D pressure solutions. Figure 3.5 is an example of a reconstructed 3D solution.

### 3.5.2 Results with 2D RANS Sectional Data

The overall aerodynamic coefficients are well predicted except for $C_{L_{max}}$, which is overestimated (Figures 3.6, 3.7 and 3.8). However, at low angles of attack the solution compares quite well against 3D RANS.

Figure 3.9 and 3.10 show the pressure distribution and the skin friction lines comparison between the NL-VLM reconstructed solution and 3D RANS at $C_L = 0.639$. The pressure distribution from the reconstructed solution compares well along the span with the exception of the winglet. Differences are also noticeable at the section near the root that could be explained by the symmetry plane effect (unsweeping effect of isobars (Kuchemann, 2012)).

Swept wings such as the BRW will encounter crossflow effects which become important at higher angles of attack. It can be seen in Figure 3.11 that the effect of the crossflow is not modeled by the 2D RANS sectional data. The flow separation outboard is not captured as well as the stagnation point when comparing the chordwise pressure coefficient in Figure 3.9.

The crossflow has a significant effect on stall and it is necessary to incorporate its effect in the RANS sectional data for swept wings for a better maximum lift coefficient estimation.

To avoid large legends in the Figures presented next, the solutions using two-dimensional RANS sectional data will be referred to as "2D" and the solutions using 2.5D RANS sectional data will be referred to as "2.5D" or "sweep".

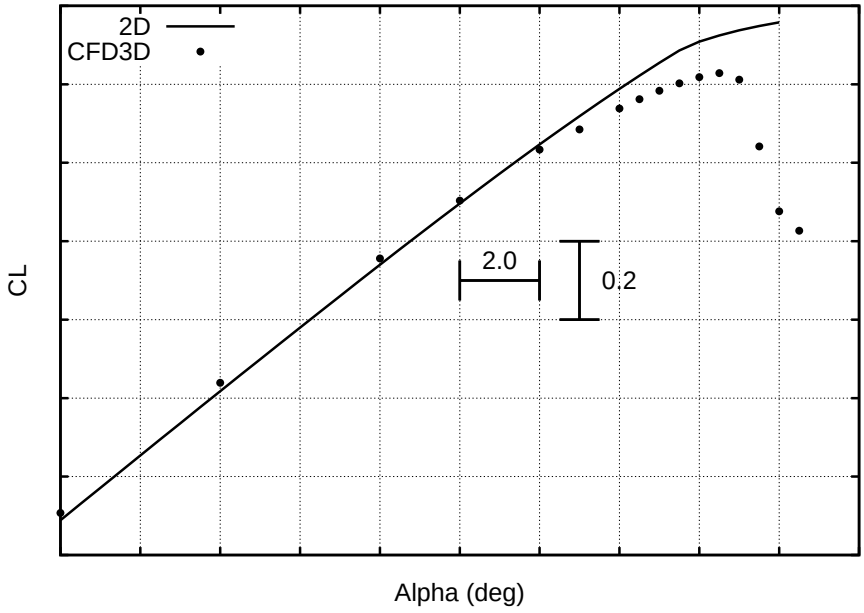


Figure 3.6 BRW - Clean isolated wing - $C_L$.

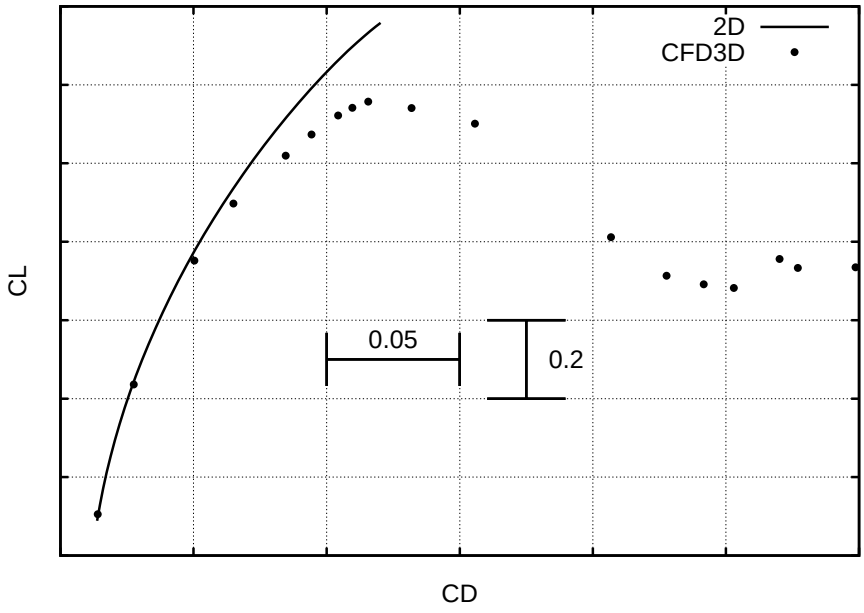


Figure 3.7 BRW - Clean isolated wing - $C_D$.

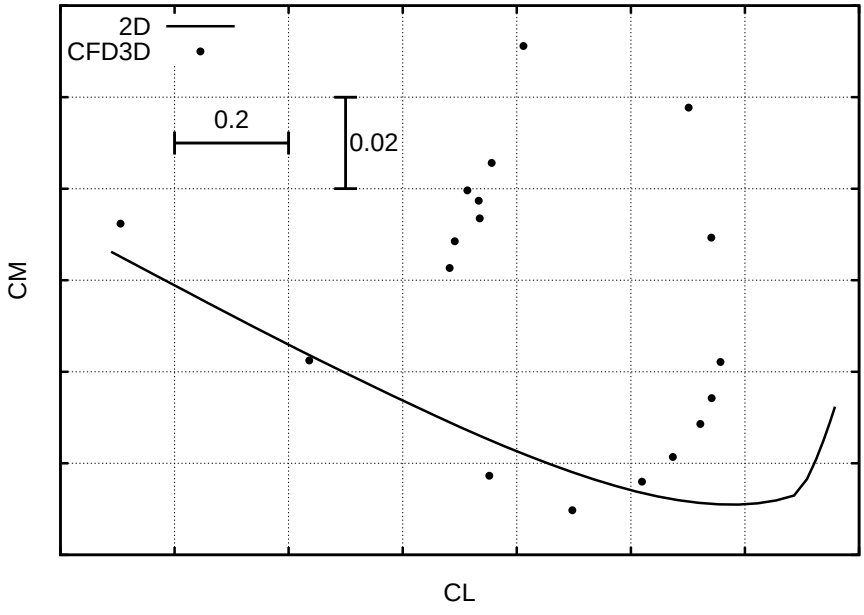


Figure 3.8 BRW - Clean isolated wing - $C_M$.

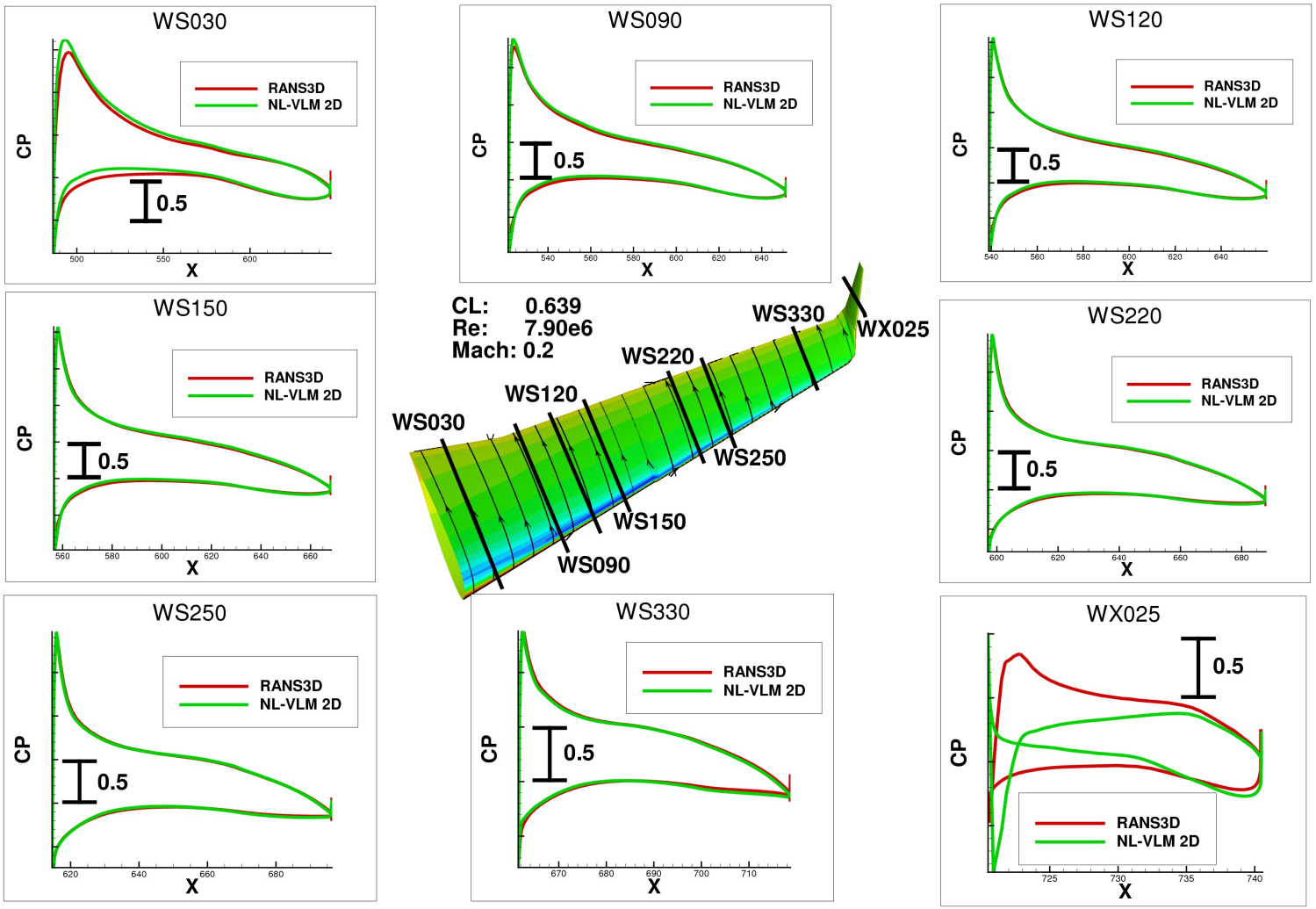


Figure 3.9 Pressure distribution along the span compared with 3D RANS.

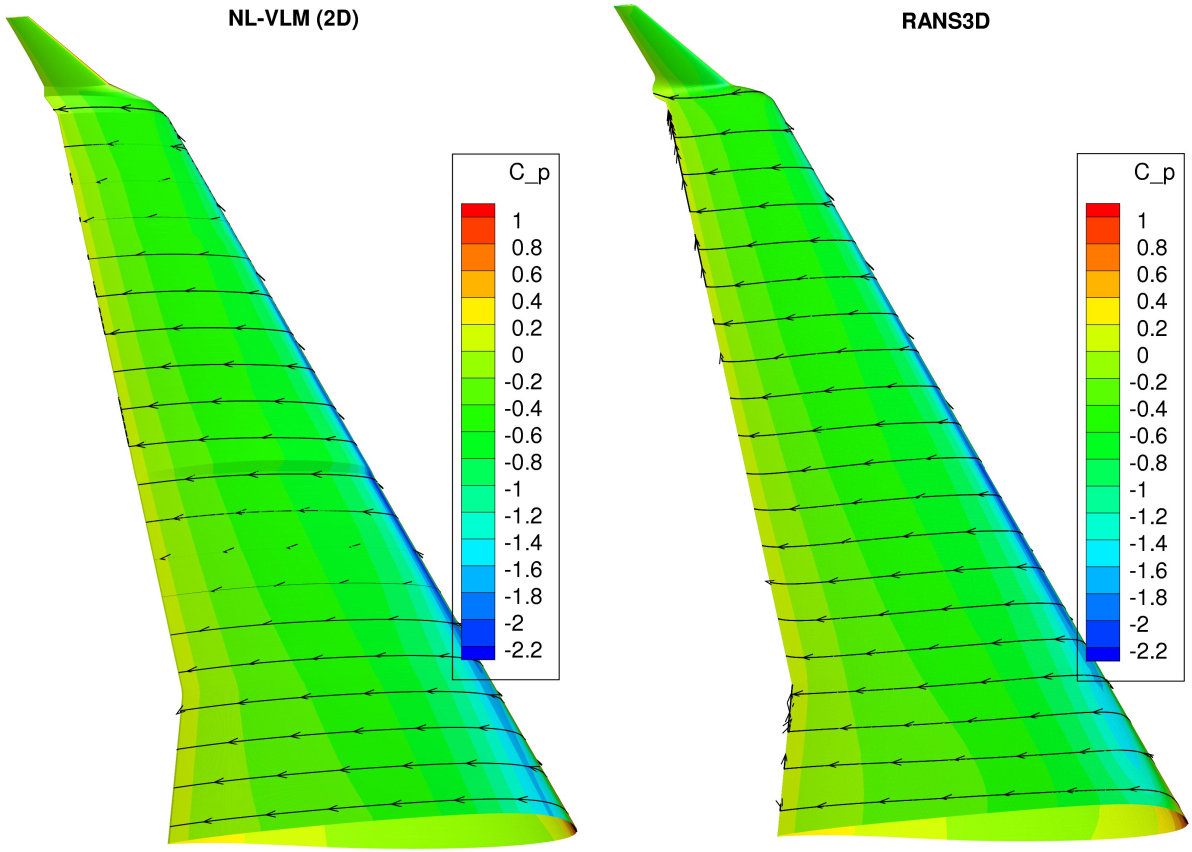


Figure 3.10 3D reconstructed solution comparison with 3D RANS at CL = 0.639.

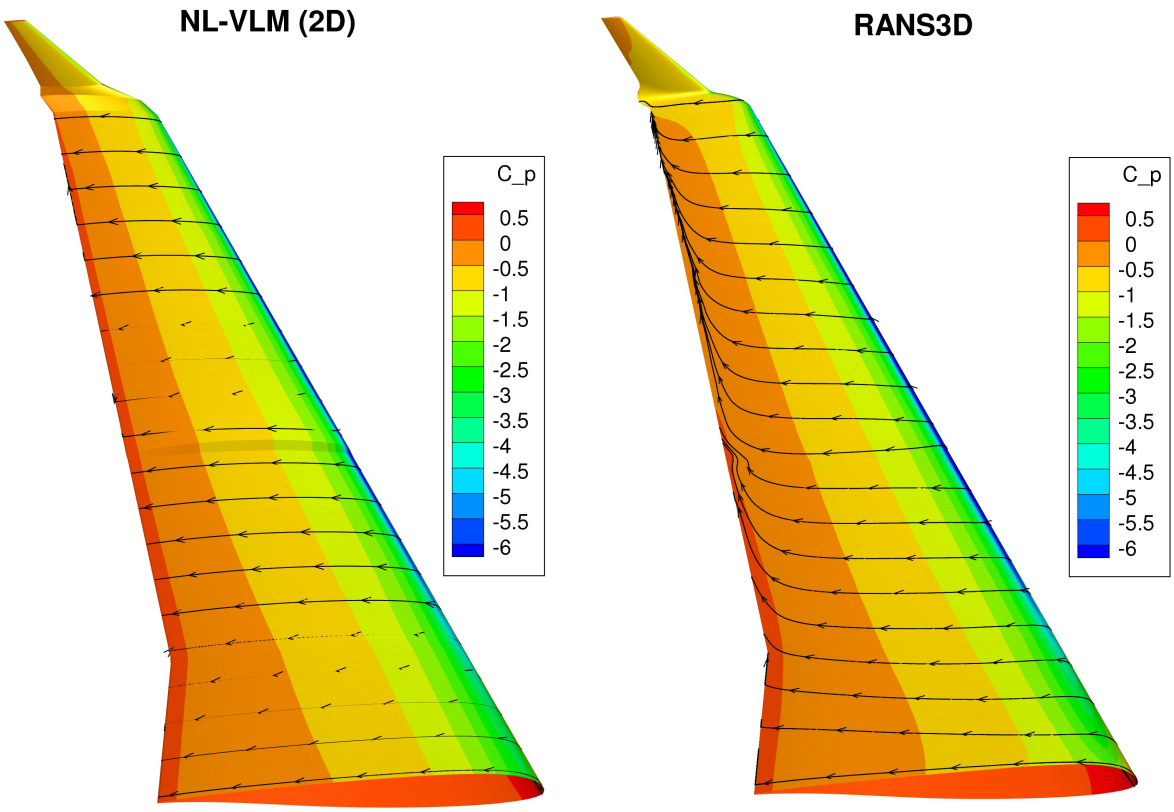


Figure 3.11 3D reconstructed solution comparison with 3D RANS at CL = 1.285.

### 3.5.3 2.5D Infinite Swept Wing

To incorporate crossflow effects in the RANS sectional data, the mesh is extruded with a sweep angle with periodicity boundary conditions applied on each side. The periodicity boundary creates an infinite swept wing condition(Kuchemann, 1956, 2012). Figure 3.12 shows the same two-dimensional RANS calculation at the wing station *WS030* for different sweep extrusions. The sweep causes a significant drop in the lift curve slope and the $C_{L_{max}}$ is also reduced with increasing sweep.

The change of sectional lift curve slope due to sweep is, however, an issue for the coupling scheme with the VLM. The coupling algorithm is intended to work with purely two-dimensional sectional data. The local angle of attack correction with 2.5D RANS includes viscous and sweep effects (Figure 3.13). Figure 3.14 illustrates this issue where the results with swept sectional data are no longer in good agreement with the 3D RANS solution.

This can be explained by the effect of sweep that is taken into account twice, from the VLM with the swept planform and with the sectional data. To demonstrate this double effect of sweep, the solution is run with 2.5D sectional data but with the planform modeled without sweep in the VLM (Figure 3.15(a)). The results in Figure 3.15(b) with zero half-chord sweep is in good agreement with 3D RANS because the effect of sweep has been removed from the VLM and is now only taken into account by the 2.5D RANS sectional data. However, modeling the exact planform in the VLM is preferable. Therefore, the coupling algorithm must be modified.

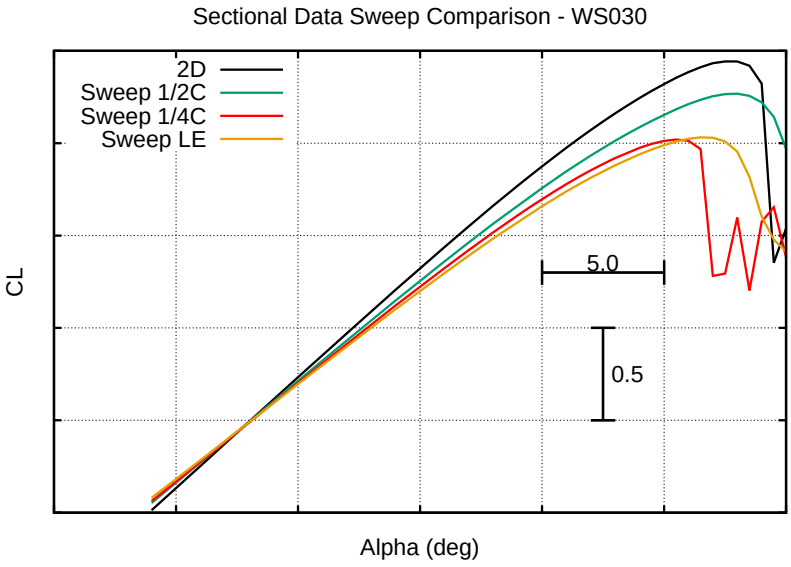


Figure 3.12 $C_{L_\alpha}$ curve for different sweep at WS030.

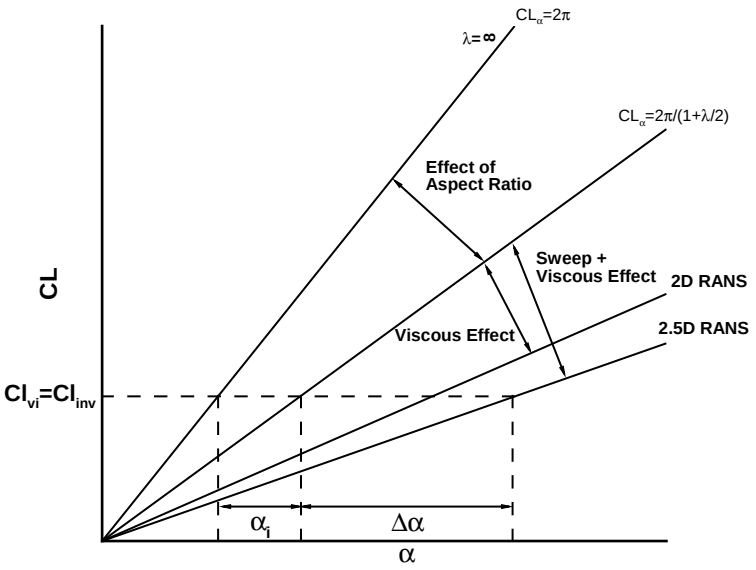


Figure 3.13 Couling algorithm with 2.5D RANS data.

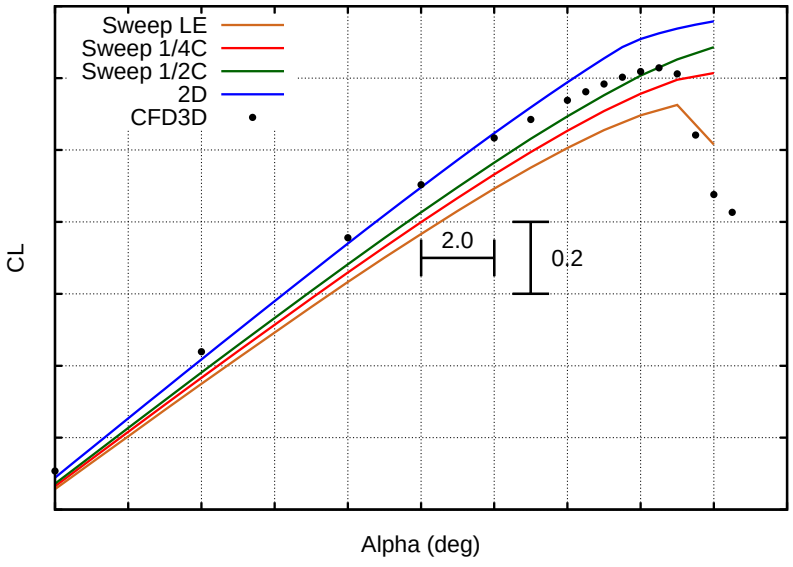


Figure 3.14 BRW - NL-VLM Solution with Different Sweep.

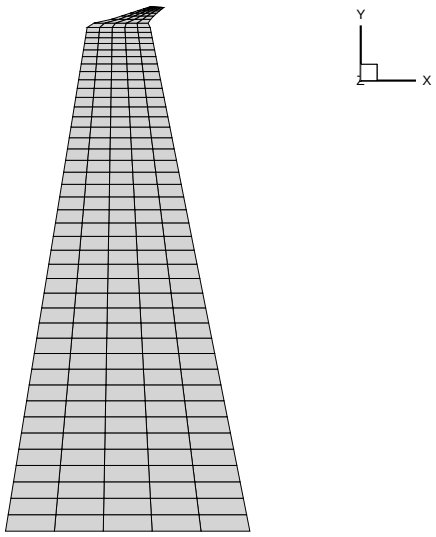


(a) VLM planform with 0 half-chord sweep.

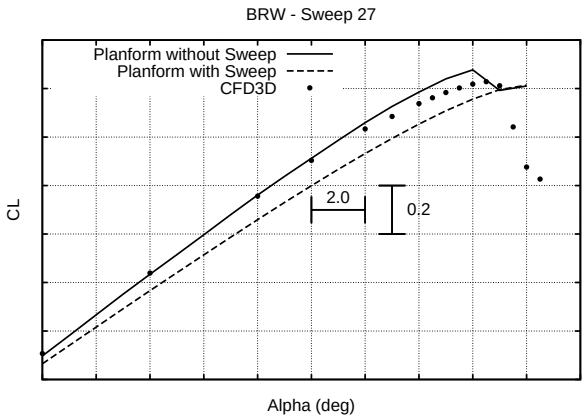


(b) NL-VLM solution with/without swept planform in VLM.

Figure 3.15 BRW - Sweep effects.

**Infinite Swept Wing Coupling with VLM**

The infinite swept wing theory was used with the lifting-line theory by Kuchemann(1956) to derive a relation between the section normal to the sweep line and the section aligned with the flow. Using the lifting-line potential equations, the lift curve slope at any given section is reprensented as follow :

$$a = 2\pi \frac{cos\phi}{sin\pi n_o} \frac{2n}{1 - \pi n(cot\pi n - cot\pi n_o)} \tag{3.18}$$

where $n$ and $n_o$ both depends on the sweep and the position along the span. For an infinite swept wing, $n = n_o = \frac{1}{2}$ and the lift curve slope becomes :

$$a = 2\pi cos\phi \tag{3.19}$$

The change of sectional lift curve slope due to sweep effect may be regarded as a change of the effective incidence(Kuchemann, 1956) :

$$\alpha_e = \frac{C_l}{2\pi} \tag{3.20}$$

$$\alpha_{ep} = \frac{C_l}{a} = \frac{C_l}{2\pi cos\phi} \tag{3.21}$$

$$\frac{\alpha_e}{\alpha_{ep}} = \frac{2\pi cos\phi}{2\pi} \rightarrow \alpha_e = \alpha_{ep} cos\phi \tag{3.22}$$

where $\alpha_{ep}$ is the effective incidence in the section normal to the sweep line. Therefore, Equation 3.22 states that the effective angle of attack normal to the sweep line is related by a factor of $\cos\phi$ to the stripwise angle of attack where $\phi$ is the sweep angle. In other words, if the sweep line normal section angle of attack is $\alpha_{ep}$, the streamwise section angle of attack is equal to $\alpha_{ep} \cdot \cos\phi$. Therefore, the correction $\cos\phi$ must be applied in the coupling algorithm to the local angle of attack ($\alpha_{2D}$) where $\phi$ corresponds to sweep used to generate the sectional RANS data. The idea is to separate the sweep effects from the viscous effects in the correction applied to the local AoA (Figure 3.16). Thus, the coupling algorithm becomes :

**Algorithm 4** Van Dam modified $\alpha$ method for 2.5D RANS sectional data

1: Solve the lifting line method to calculate $Cl_{inviscid}$
2: **for** Every Span-Wise Section $i$ **do**
3: Calculate the effective angle of attack :

$$\alpha_e(i) = \frac{Cl_{inviscid}(i)}{Cl_\alpha} - \alpha_{2D}(i)cos(\phi) + \alpha_{3D} \tag{3.23}$$

4: Interpolate the viscous lift at the effective angle of attack :
$\alpha_e(i) \Rightarrow Cl_{visc}(\alpha_e(i))$
5: Calculate the angle of attack corection :
$\alpha_{2D}(i) = \alpha_{2D}(i) + \frac{Cl_{visc}(\alpha_e(i)) - Cl_{inviscid}(i)}{Cl_\alpha}$
6: **end for**
7: Repeat Steps 1-6 until $|Cl_{visc} - Cl_{inviscid}| < \epsilon$

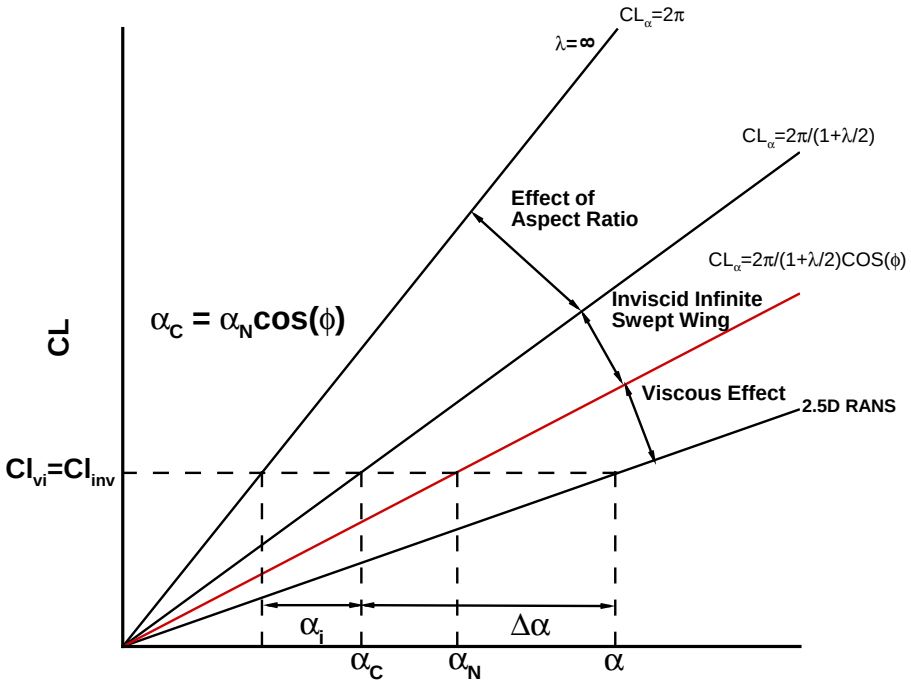


Figure 3.16 Couling algorithm modified for 2.5D RANS data.

With the correction $\cos\phi$ applied, 2.5D RANS data can be successfully coupled with the VLM. The lift curve slope of the linear portion remains the same in regards to the different sweep used, thus confirming the $\cos\phi$ correction (Figure 3.17). Crossflow effects are significant at higher lift coefficient and also stronger with increasing sweep. Thus, an earlier stall is observed with sweep with an increase in viscous drag as well (Figure 3.18).

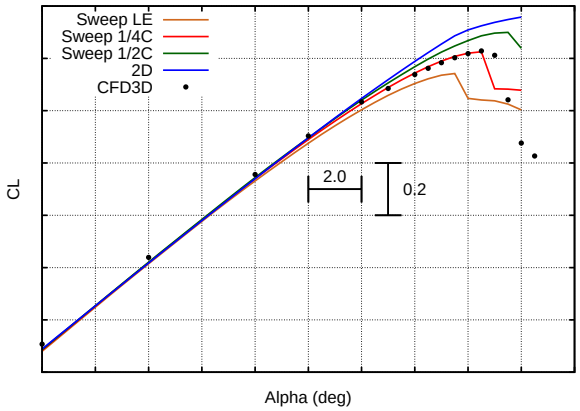


Figure 3.17 BRW - Isolated wing - $C_L$.

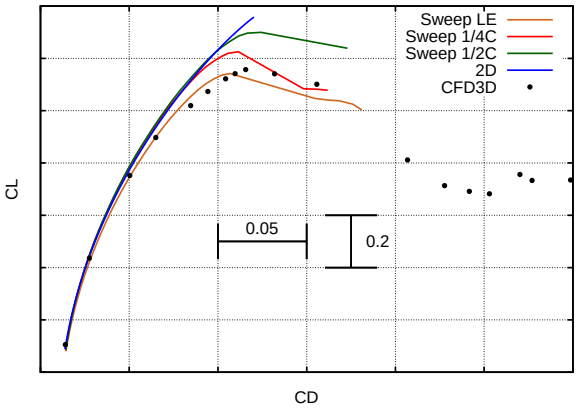


Figure 3.18 BRW - Isolated wing - $C_D$.

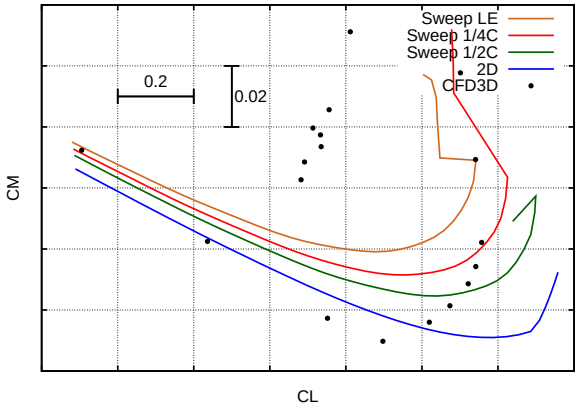


Figure 3.19 BRW - Isolated wing - $C_M$.

Incorporating crossflow effects increase the accuracy of the chorwise pressure distribution evaluation(Figure 3.20). The pressure distribution interpolated from the VLM solution with 2.5D sectional data is more accurate when compared to the 3D RANS solution. The leading edge pressure peak is better captured as well as the stagnation point with significant effect over the moment calculation (Figure 3.19). Moreover, a better $C_{L_{max}}$ prediction is achieved with 2.5D sectional data (Figure 3.17). This is mainly due to the outboard separation that can be captured with 2.5D RANS (Figure 3.21). These results clearly show the necessity of using 2.5D for swept wings, but one question remains regarding the sweep line to use for generating these sectional data.

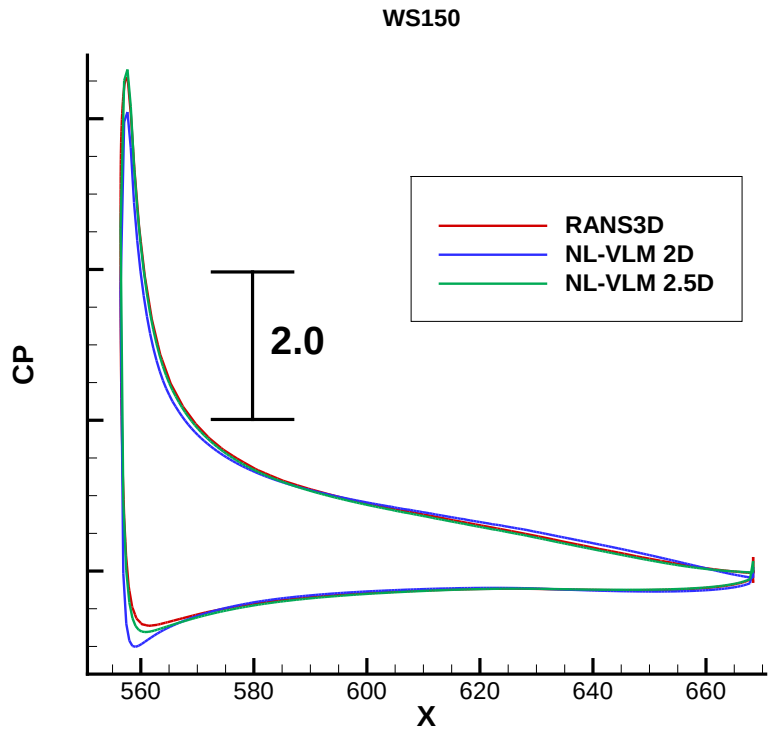


Figure 3.20 Presure distribution at WS150 at CL = 1.285 with 1/4C sweep used for the 2.5D.

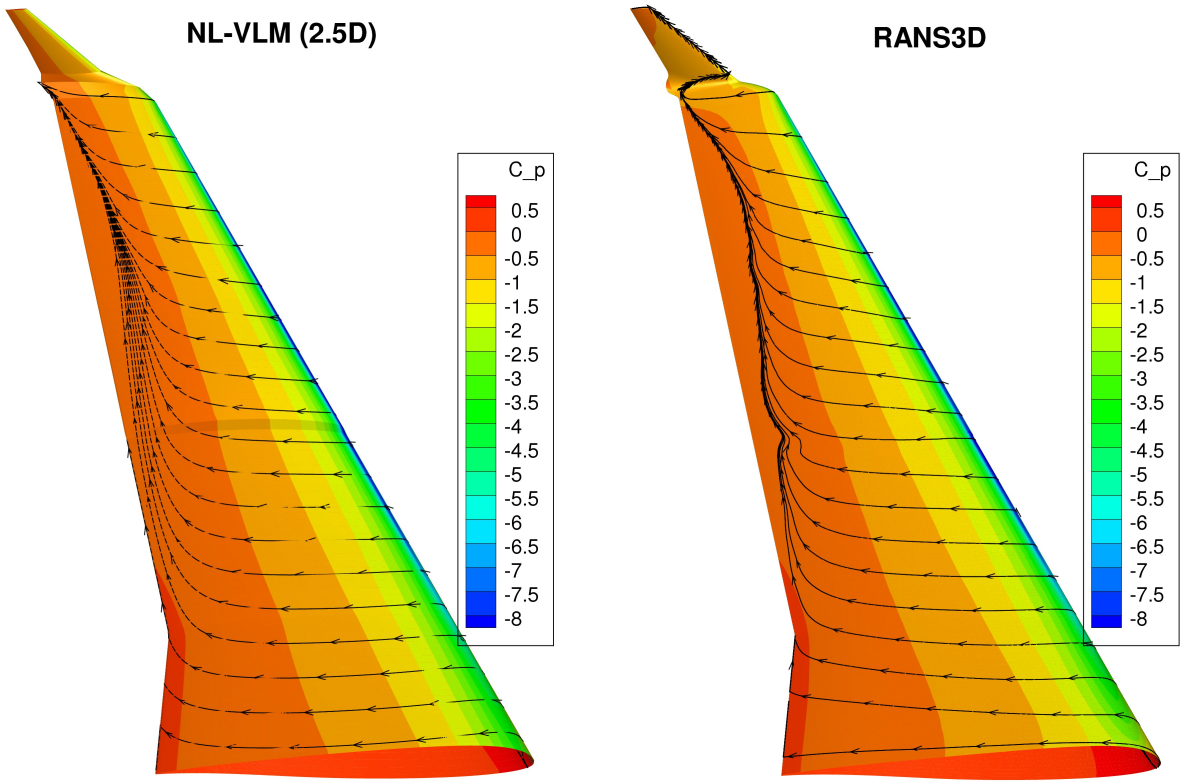


Figure 3.21 3D reconstructed solution comparison with 3D RANS at alpha = 15.5 with 1/4C sweep used for the 2.5D RANS sectional data.

### 3.5.4 BRW - High-Lift Configuration

The BRW has a partial span flap configuration and three different flap deflections are investigated (10°, 20° and 30°). The section cuts used to generate the viscous database are presented in Figure 3.22.

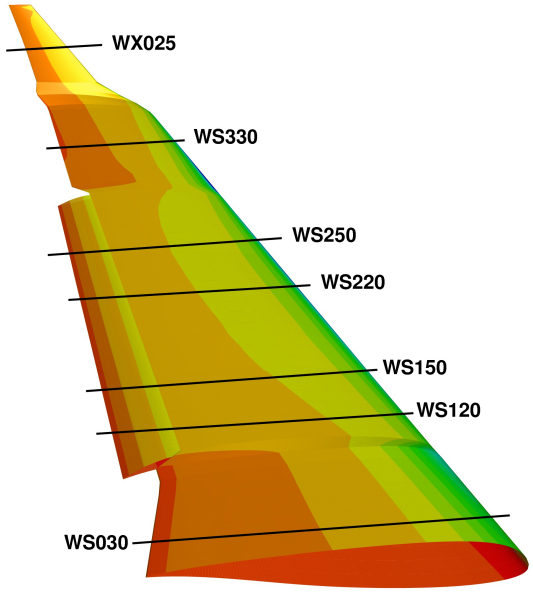


Figure 3.22 BRW high-lift configuration - Cuts for viscous sectional data calculation.

#### Artificial Viscosity

The VLM models only the clean planform and the section aerodynamic's characteristics are incorporated by the viscous database. Therefore, the VLM's geometry never changes when designing high-lift systems which is a simplification allowing easier high-lift aerodynamic analysis. However, issues arise with partial-span flap like the BRW. An important increment in circulation is present along the span at both intersections where the flap begins and ends. Theses increments cause a large circulation to be released in the wake(Figure 3.23) which in turn creates a strong upwash outboard. The upwash induces an earlier stall caused by spontaneous stall cells appearence(Spalart, 2014). To avoid this numerical stall, artificial viscosity is added to ensure convergence to a unique solution and dissipation of these stall cells (Figure 3.24). The artificial viscosity is implemented following the work of Gallay(2016) and Chattot (2004).

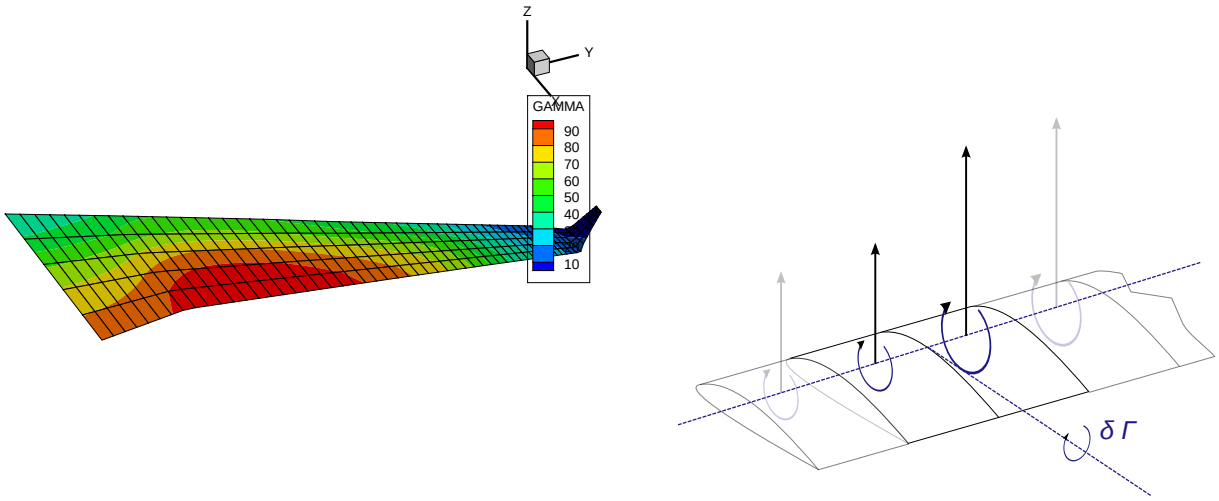


Figure 3.23 Strong upwash induced by a partial span flap.

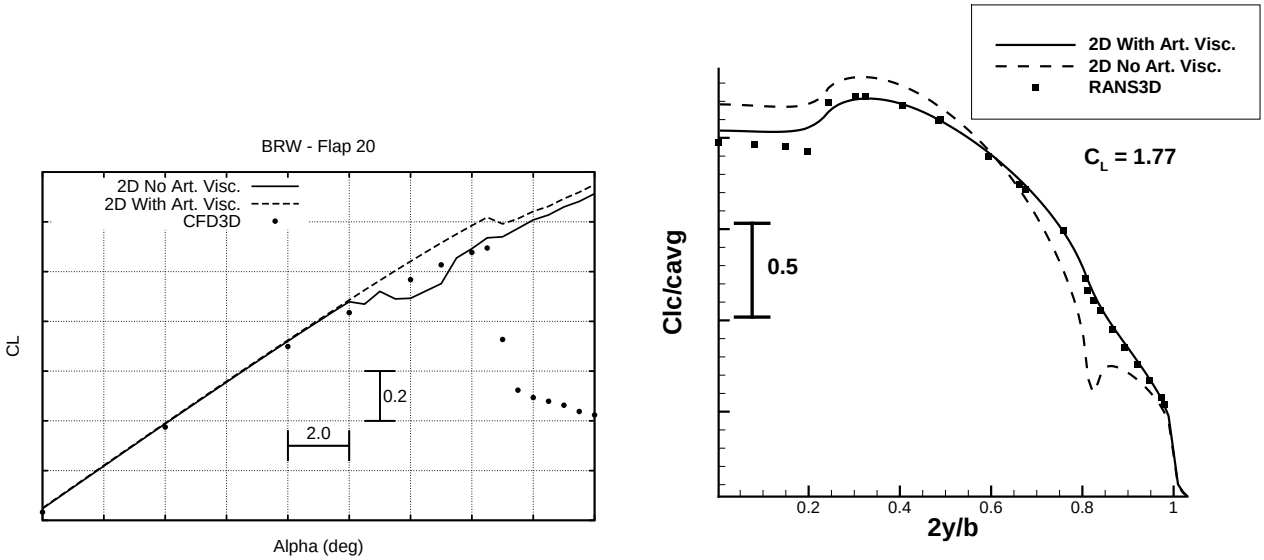


(a) $C_L$ - $\alpha$.

(b) Spanload - $C_L = 1.77$.

Figure 3.24 BRW Flap 20 - Artificial dissipation with 2D RANS sectional data.

## High-Lift Configuration Results

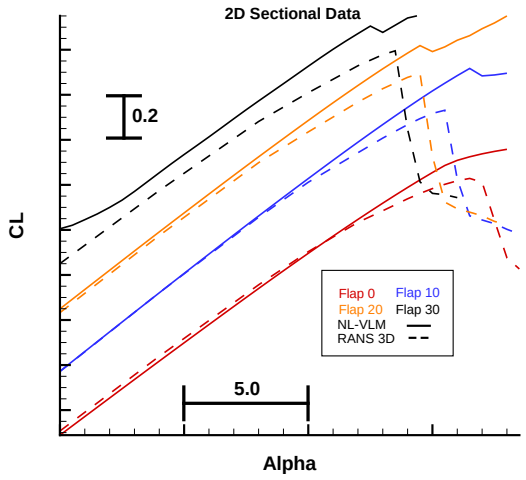


(a) CL - 2D sectional data.

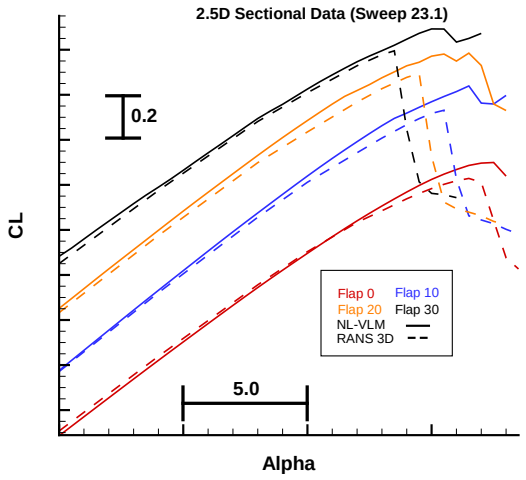


(b) CL - 2.5D sectional data (Sweep 1/2C).

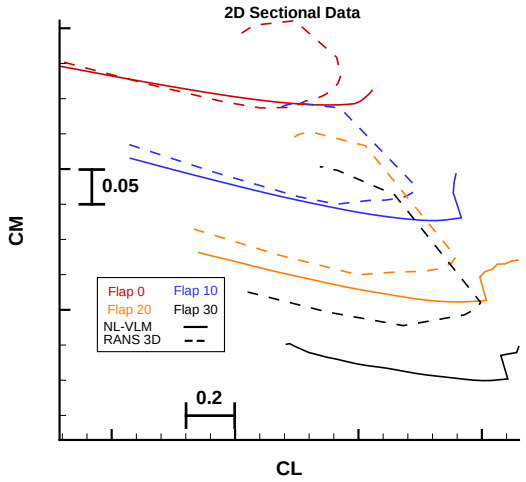


(c) CM - 2D sectional data.

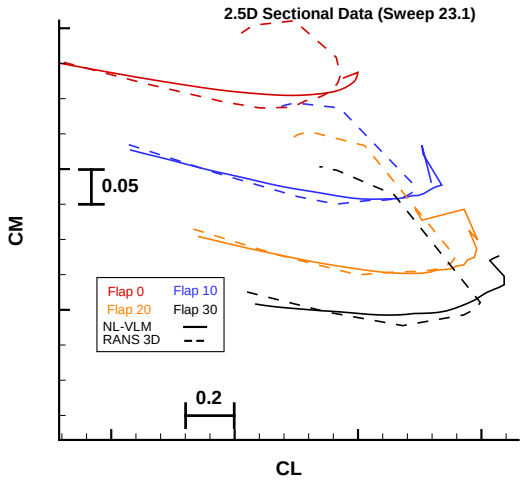


(d) CM - 2.5D sectional data (Sweep 1/2C).

Figure 3.25 BRW - Aerodynamic coefficient increment in regards to flap deflection .

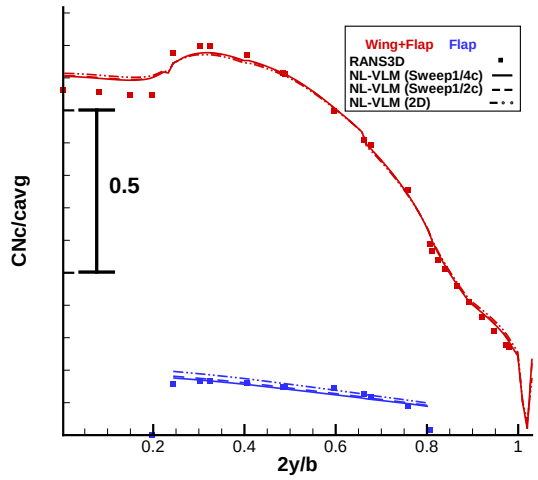


(a) SpanLoad flap 10 at $C_L = 0.921$.

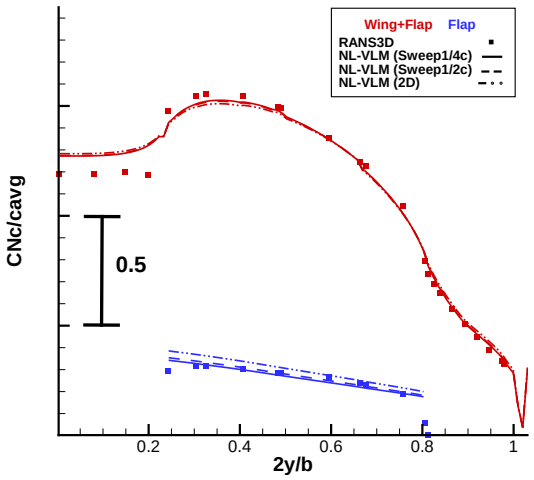


(b) SpanLoad flap 20 at $C_L = 1.175$.

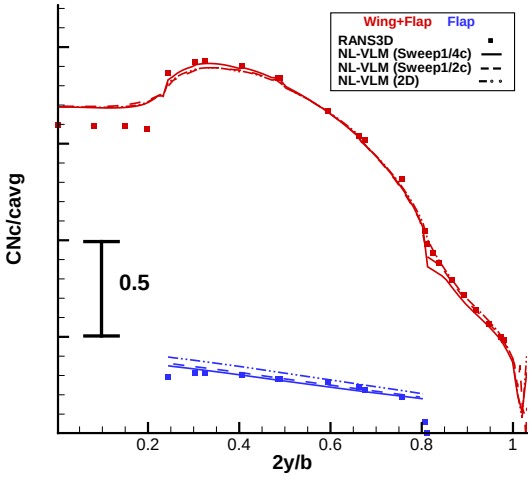


(c) SpanLoad flap 20 at $C_L = 1.499$.

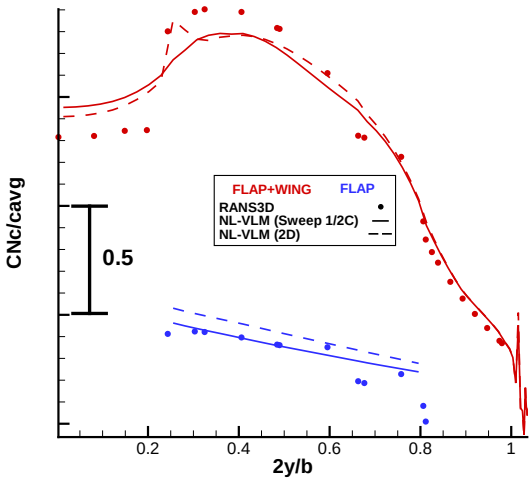


(d) SpanLoad flap 30 at $C_L = 1.375$.

Figure 3.26 BRW high-lift configuration - Spanload.

**Discussion**

The verification performed on the BRW confirms the necessity to use 2.5D RANS sectional data to increase the method's fidelity over swept wings. A better maximum lift coefficient is achieved and outboard separation is well captured compared to 3D RANS (Figure 3.21).

The importance of crossflow is further confirmed in the aerodynamic coefficient increments due to flap deflection (Figure 3.25). The $C_{L_{max}}$ estimation is overestimated when using two-dimensional data and the lift coefficient with flap deflected at 30° is not in agreement with the 3D RANS solution. The difference is even more important for the moment coefficient with the flap deflected at 20° and 30°. However, the results with 2.5D RANS sectional using the half-chord sweep compare quite well against the 3D RANS solution and for all flap deflections.

The difference in the results between the solution using 2D RANS and the 3D RANS solver for high flap deflection is explained by analyzing the spanload over the flap (Figure 3.26). The two-dimensional sectional data cannot capture accurately the spanload over the flap where crossflow effects are significant. A constant offset compared to 3D RANS is observed, particularly at 30 degrees flap deflection. This explains the difference of lift coefficient and moment coefficient at higher flap deflection when using two-dimensional data. On the other hand, the 2.5D RANS solution captures correctly the spanload over the flap.

Finally, different sweep lines were used to generate the 2.5D sectional data to investigate the effects over the aerodynamic coefficients. As expected, higher sweep induces stronger crossflow effects which in turn reduces the maximum lift coefficient. For the clean configuration, sectional data using the quarter-chord sweep line seems to produce the best results. However, the half-chord sweep line seems more appropriate for the high-lift configuration. Therefore, it appears that the correct sweep line to use lies between the half-chord and the quarter-chord line. However, a constant sweep along the span was assumed and this assumption might not be appropriate. As it can be seen on the pressure distribution and spanload, two-dimensional sectional data solutions have a better match at the root than 2.5D solutions. This can be explained by the unsweeping effect encounter at the symmetry plane(Kuchemann, 2012). Thus, different spanwise distributions of swept sectional data should be investigated.

The complete results of this verification campaign on the BRW is available in Appendix C.

### 3.6 Transonic Conditions

A validation of the method was performed by Gallay and Laurendeau (2016) in transonic conditions. A comparison with experimental data was performed on the DLR-F4 configuration at $Mach = 0.75$. The 2.5D RANS allows the shock position to be captured more accurately than two-dimensional RANS over swept wings(Figure 3.27). These results confirm the fidelity of the method for transonic regimes. The fuselage is not addressed in this work.

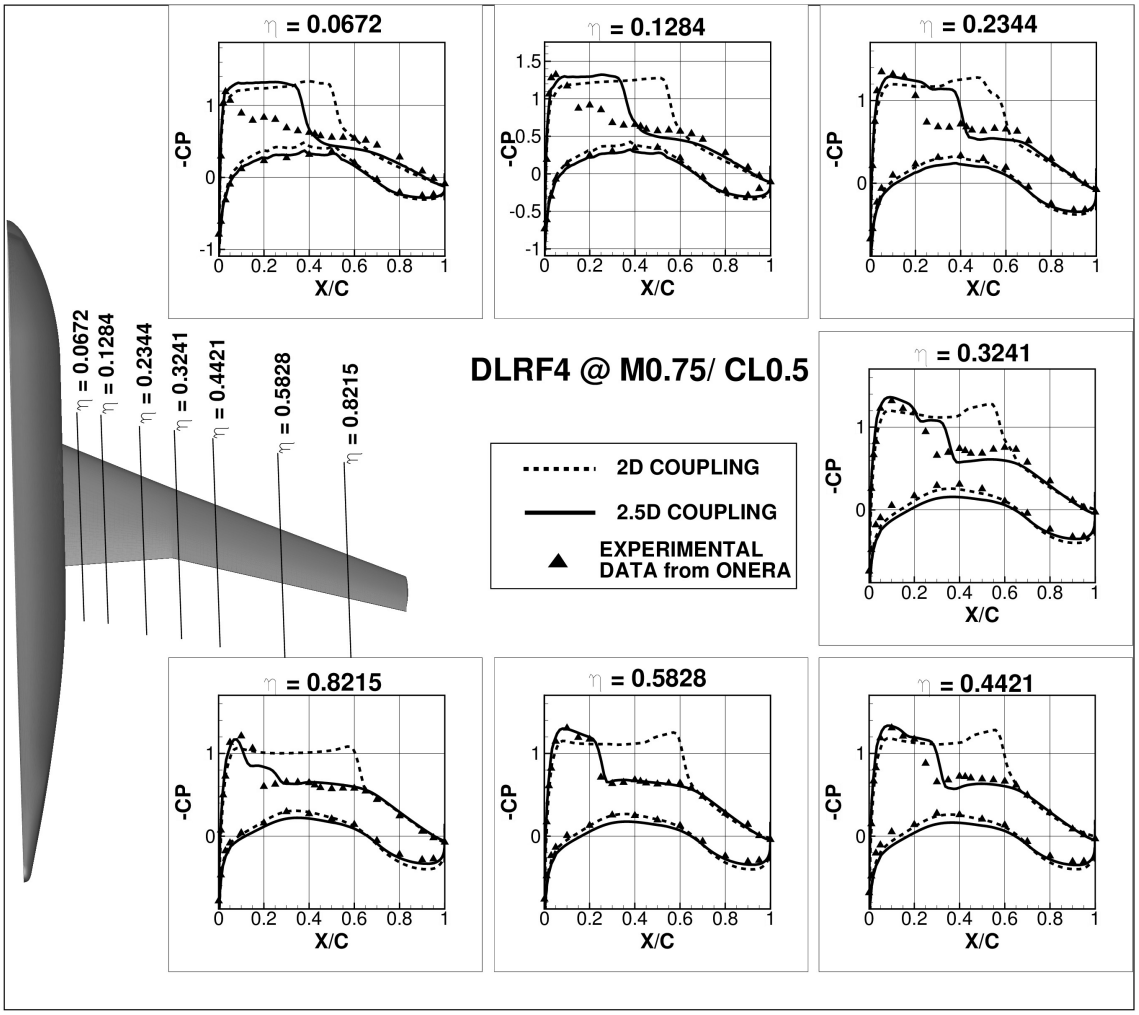


Figure 3.27 DLRF4 - Pressure coefficient at $Mach = 0.75$ and $C_L = 0.5$ (Source : Gallay and Laurendeau (2016)).

# CHAPTER 4 WING PLANFORM OPTIMIZATION

The goal of this chapter is to explore the aerodynamic optimization of lifting surfaces using a coupled VLM/2.5D RANS approach. A spanwise stall constraint is considered with $C_{L_{max}}$ objective function and cruise performance in transonic conditions as well.

## 4.1 Reference Geometry

The Lovell wing (Lovell, 1977) is a 30.5° leading edge swept wing (Figure 4.1(a)) that was used for wind tunnel investigation on the effect of flap deflections. The geometry is simple with a constant airfoil geometry (Figure 4.1(b)) along the span and experimental results are available for the isolated wing at different flap deflections. For its simplicity and available geometry for clean and high-lift configurations, the isolated Lovell wing was chosen as the reference geometry for this optimization work. The geometry and experimental data were used by Valarezo to calibrate its widely used semi-empirical stall criteria (Cebeci *et al.*, 2005).

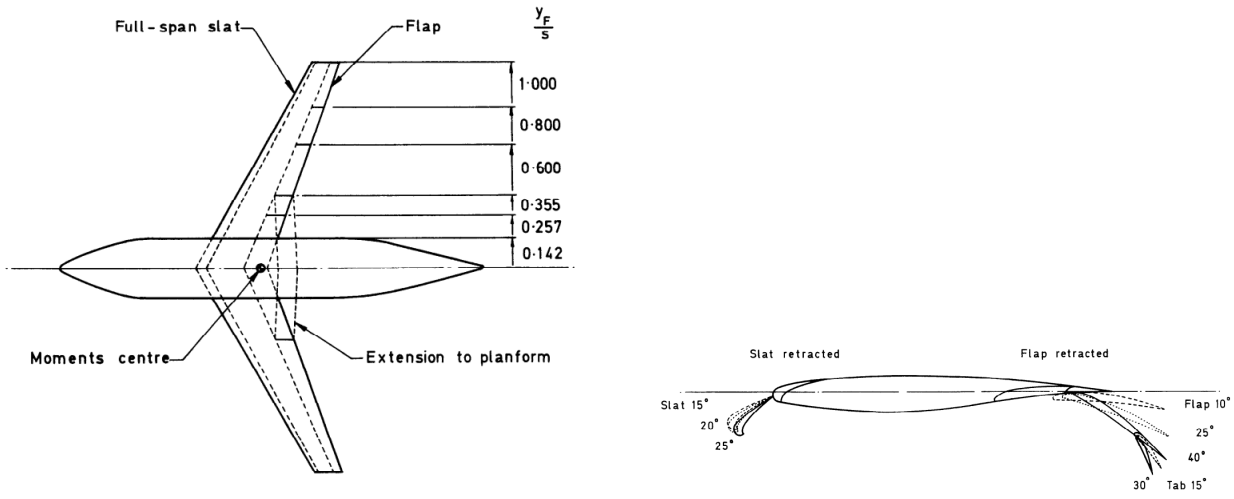


(a) Planform. (b) Airfoil.

Figure 4.1 Lovell geometry(Lovell, 1977).

The VLM coupled with RANS solutions are compared against experimental data for the Lovell wing to verify that the aerodynamic coefficients are well estimated by the method for the reference geometry(Figures 4.2-4.6).

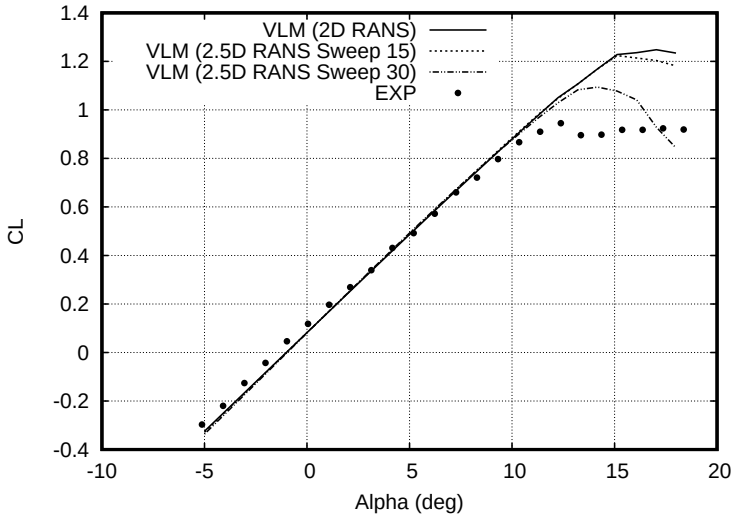


Figure 4.2 Lovell clean configuration - CL.

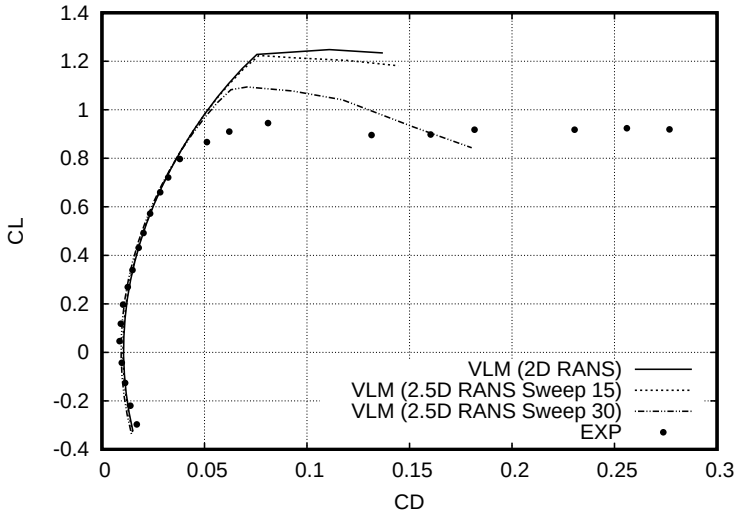


Figure 4.3 Lovell clean configuration - CD.

## 4.2 Spanwise Stall Detection Criteria

The VLM coupled with viscous sectional data is capable of capturing stall cells as it was demonstrated by Spalart(2014). Stall cells are triggered when the lift-curve slope becomes negative. Therefore, the appearance of the first stall cell spanwise is used as the criteria for the stall position. To do so, the spanload before and after $\alpha_{max}$ is compared and the highest $\Delta Cl$ indicates the position of the stall cell, thus the spanwise stall position(Figure 4.7). This criteria was found to be very robust in all attempted flow simulations.

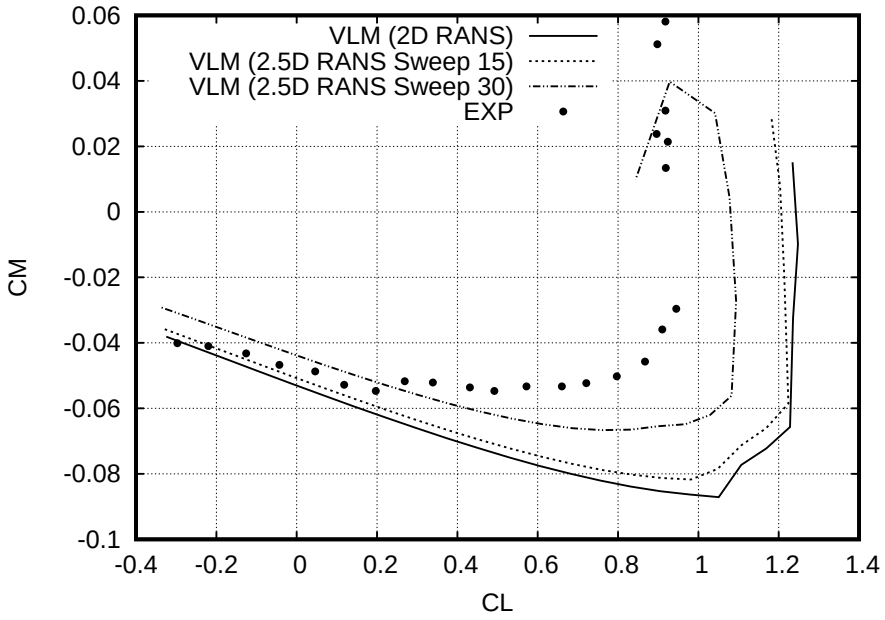


Figure 4.4 Lovell clean configuration - CM.

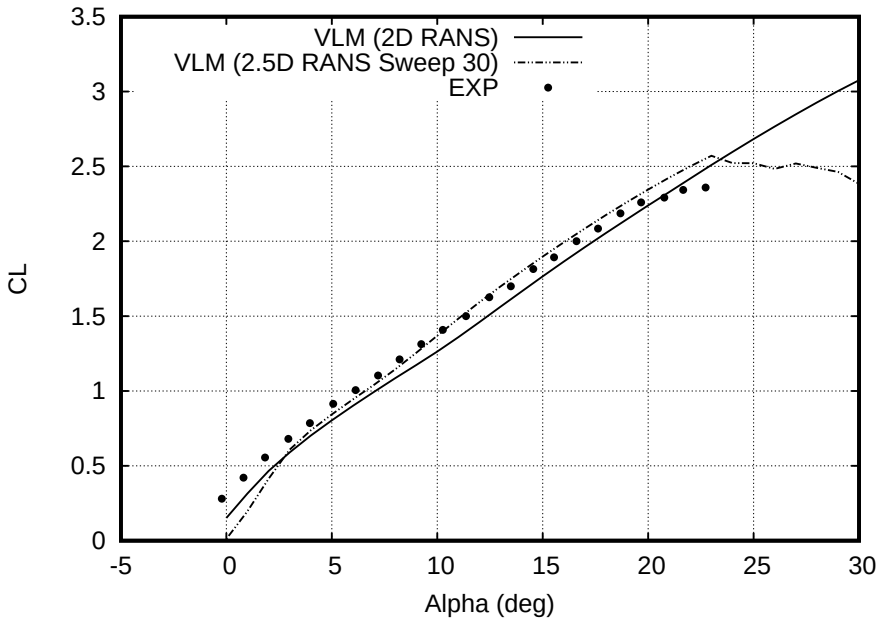


Figure 4.5 Lovell slat : 25° flap : 10° - CL.

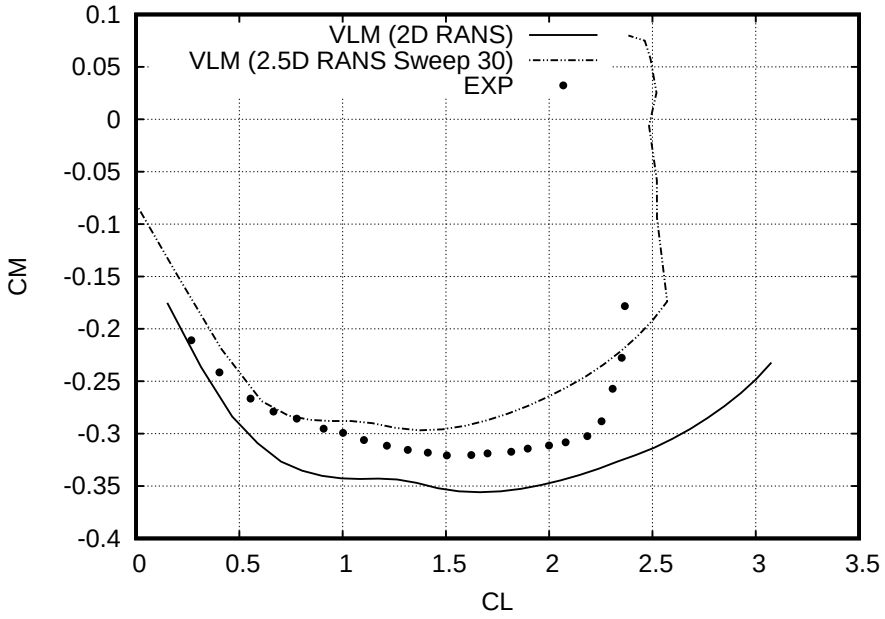


Figure 4.6 Lovell slat : 25° flap : 10° - CM.

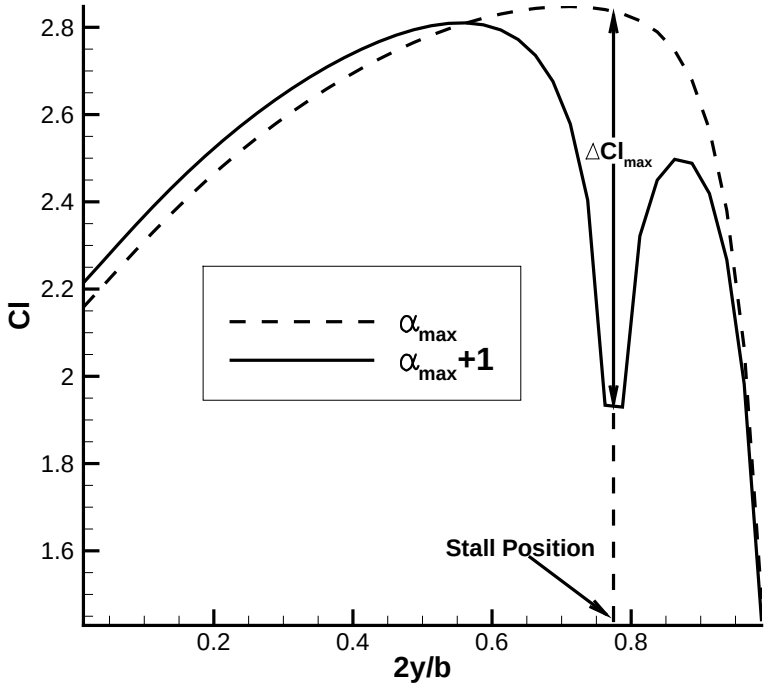


Figure 4.7 Spanwise stall detection scheme.

## 4.3 Evolution Strategy Optimizer

The use of a fast aerodynamic analysis tool allows a stochastic optimizer to be use. Moreover, gradient free optimizers are preferable for $C_{L_{max}}$ optimization since it can be a non-linear function. Thus, a Covariance Matrix Adaptation Evolution Strategy (CMA-ES) was chosen for its well known performance on non-linear and non-continuous problems (N. and A., 2001; Arnold and Hansen, 2012). CMA-ES is considered as state-of-the-art in evolutionary algorithm and reliable for global optimization(Hansen *et al.*, 2004). Furthermore, CMA-ES requires almost no calibration except population size. The code is available from `https://www.lri.fr/~hansen/cmaes_inmatlab.html` and the Python version was used to be fully integrated inside the VLM C++ Python interface.

### 4.3.1 Non-Linear Constraints

CMA-ES does not handle contraint by default. However, a penalty constraint violation can be incorporated following the work of Collangea *et al.* (2010). For every constraint $i$ and for a given solution $x$, the constraint value is computed as follow

$$\gamma_i(x) = \frac{1}{\epsilon_i} \times \Big\{ g_i(x) + \epsilon_i \text{ for inequality constraint } g_i(x) \leq 0.0 \Big\} \tag{4.1}$$

where $\epsilon_i$ are user-defined values. When $\gamma_i > 0$, the constraint is considered active and a penalty is added to the objective function. The penalty is evaluated with equation 4.2

$$f_i(x) = \begin{cases} w_i \gamma_i(x)^2, & \text{if } \gamma_i > 0 \\ 0, & \text{otherwise} \end{cases} \tag{4.2}$$

where $w_i$ are user-defined constants to scale the penalty. Every penalty $f_i$ are added to the cost function.

### 4.3.2 VLM with CMA-ES Implementation Verification

To verify the implementation of CMA-ES with the VLM, an induced drag minimization was performed with the twist as the design variable. The geometry used was the Lovell wing and it was discretized with 50 panels spanwise and 5 panels chordwise(Figure 4.8). The twist is controled at 5 equaly distant points along the span, thus 5 design variables are used. An inequality constraint for the lift coefficient, $C_L \geq 0.5$, is also added to verify the cost penalty implementation. Since the VLM is based on Prandtl's lifting-line theory, the optimal solution should be at $C_L = 0.5$ with a twist distribution giving an elliptical spanload, thus the lowest induced drag.

Results show that an elliptical spanload has been recovered by the optimizer as expected(Figure 4.9). Only 1000 function evaluations was necessary to achieve the optimal solution (Figure 4.10(a)) which took under 20 minutes complete on 6 cpus in parallel. A population size of eight was used, thus 1000 function evaluations represent 125 optimizer iterations. Furthermore, the inequality constraint on $C_L$ was handled properly with the final solution lying at $C_L = 0.5$ as expected (Figure 4.10(b)).

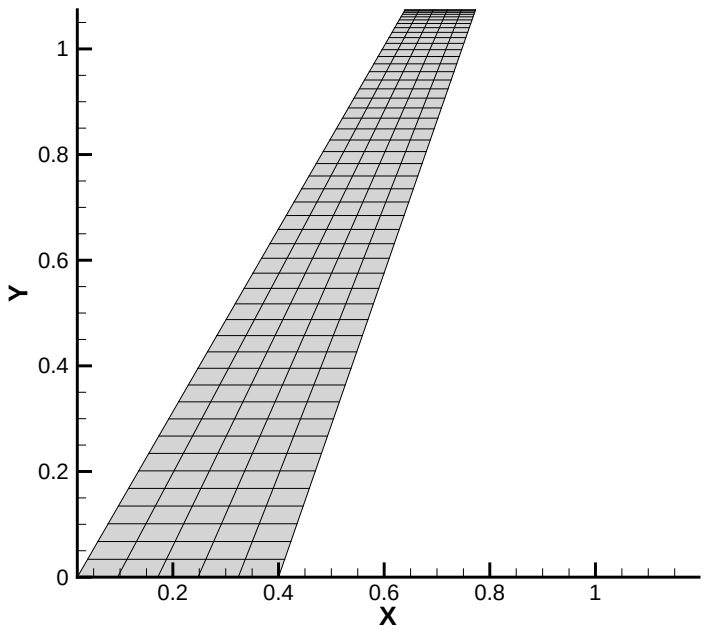


Figure 4.8 Lovell - VLM planform mesh.

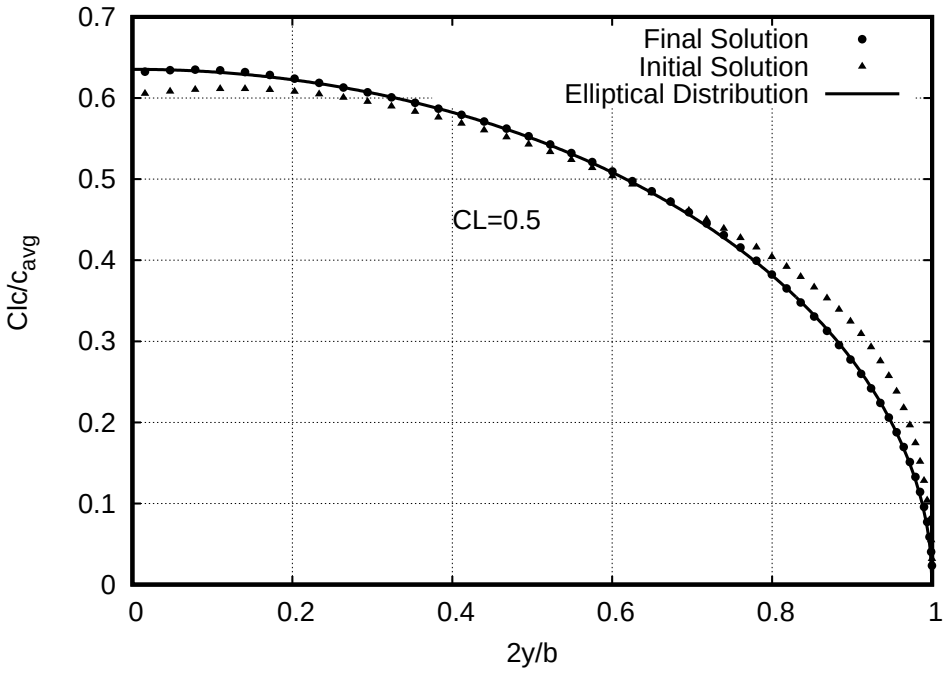


Figure 4.9 Twist optimization to minimize the induced drag.

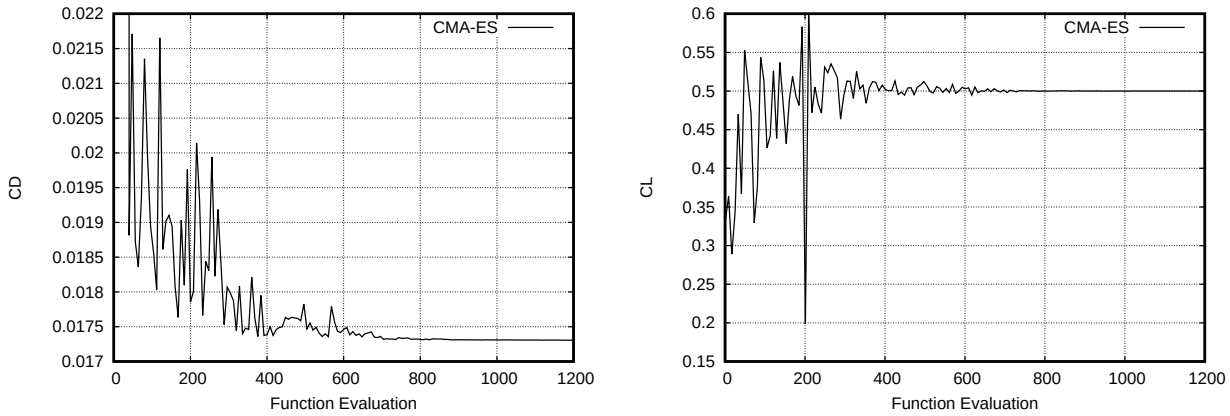


(a) Objective function convergence.

(b) Constraint $C_L \geq 0.5$.

Figure 4.10 CMAES - Induced drag optimization.

## 4.4 Structural Model

A structural constraint must be considered to avoid optimal solutions with unrealistic geometries (infinite span). A simple solution is to incorporate the wing's weight calculation with a constraint stating that the optimal solution cannot be heavier than the Lovell reference wing. Since the constraint is applied as a difference in terms of weight between the new configuration and the reference Lovell wing, the sensitivity in regards to the wing's geometry is more important than the precision of the wing's weight calculation. A sensitivity analysis was performed by Mariens (2012) for different statistical methods for wing weight estimation and the results of the analysis are presented in Table 4.1. From the analysis, Torenbeek and EMWET are the two methods with the best sensitivity in regards to wing parameters like sweep, thickness, span, etc...

The Torenbeek weight estimation used is a statistical method (Torenbeek, 1976) derived from a more complex quasi-analytical method derived also from Torenbeek. The evaluation of the wing weight is performed with Equation 4.3.

EMWET is a quasi-analytical tool developed by Elham *et al.* (2012) to estimate the wing weight. A VLM is used to calculate the spanload to increase the fidelity of the method. From the validation performed by Elham (2012), EMWET achieves levels of accuracy comparable to Finite Element Method based weight prediction, but with the same computation cost than empirical methods.

EMWET seems like a valid approach for the current aerodynamic solver. However, its implementation is more complex than Torenbeek's statistical approach and the structural accuracy is not the goal. Therefore, Torrenbeek was chosen to evaluate the wing weight, but EMWET should be considered for future work.

Table 4.1 Wing weight estimation method sensitivity to wing parameters (adapted from Mariens (2012)).

| **Method** | $W_{to}$ | $W_{zf}$ | $b$ | $c_r$ | $\Lambda$ | $\lambda$ | $t/c_r$ | $t/c_k$ | $t/c_t$ |
|---|---|---|---|---|---|---|---|---|---|
| **Torenbeek** | ✓ | ✓ | ✓ | ✓ | ✓ | ✓ | ✓ | ✓ | ✓ |
| **Howe** | ✓ | | ✓ | | ✓ | ✓ | ✓ | | |
| **EMWET** | ✓ | ✓ | ✓ | ✓ | ✓ | ✓ | ✓ | ✓ | ✓ |
| **Shevell** | ✓ | | ✓ | ✓ | ✓ | ✓ | ✓ | ✓ | ✓ |
| **LTH** | ✓ | | ✓ | ✓ | ✓ | ✓ | ✓ | ✓ | ✓ |

$$W_w = 0.06\frac{w}{\sigma_r}n_{ult}\sqrt{W_{to}W_{zf}}\frac{b^3}{S}\frac{1}{(t/c)_{ave}cos^2\Lambda}\frac{1+2\lambda}{1+\lambda} + wt_{ss}S \tag{4.3}$$

## 4.5 Viscous Database and Design Variables

The aim is to explore the optimization problem complexity that can be achieved using 2.5D RANS data with the VLM. Since low-speed $C_{L_{max}}$ and transonic cruise conditions are considered, the RANS sectional data must be generated with great care and for a wide range of conditions to perform a full flight spectrum optimization. At low-speed conditions, RANS simulations were performed for the clean configuration and for high-lift configuration with slat and flap deflected for three different flap deflections (10°, 25°, 40°). For cruise conditions, only the clean configuration was considered at four different Mach numbers (0.6, 0.7, 0.75, 0.8).

All the simulations were also performed at three different Reynolds number to capture the effect of taper ratio. Finally, to incorporate the viscous effects of crossflow over swept wings, every simulation was performed at nine different sweep angles (0°, 5°, 10°, 15°, 20°, 25°, 30°, 35°. 40°) with the 2.5D RANS flow solver NSCODE(Pigeon *et al.*, 2014). More than 3000 2.5D RANS calculations were necessary to generate the database. Note that these computations are performed only once and can be used for any optimization problem thereafter. Afterward, linear interpolation is used to generate the appropriate viscous database during the optimization, making for rapid function evaluation. The viscous database is summarized in Table 4.2.

Planform optimization is considered in the present study with seven design variables defining the geometry (Table 4.3 and Figure 4.11). The wing twist is defined by a linear function fixed by the root and tip twist. The tip chord is given a lower bound of 0.13 to prevent unrealistic geometries and ensure sufficient chord length for winglets. The leading edge sweep is bound between 0° to 40° which corresponds to the range of sweep evaluated in the viscous database. The spanwise kink position is set to a minimum of 0.1524 that corresponds to the actual Lovell wing's kink position and the chord's length at the kink position is controlled by the trailing edge sweep. The root chord is given a lower bound of 0.2 to avoid again unrealistic geometries. The planform surface area is also kept constant to the Lovell reference geometry, thus the span is evaluated at each function evaluation with the design variables to keep the wing surface area constant.

Table 4.2 Viscous database.

| | Low-Speed | High-Speed |
|---|---|---|
| **Mach Number** | 0.2 | 0.6, 0.7, 0.75, 0.8 |
| **Reynold's Number** | 0.7E6, 1.3E6, 2E6 | 3.3E6, 6.3E6, 9.3E6 |
| **Sweep** | 0, 5, 10, 15, 20, 25, 30, 35, 40 | |
| **Angle of Attack** | -6 to Post-Stall | |
| **Slat** | Retracted, Deflected : 25 | Retracted |
| **Flap** | Retracted, Deflected : 10, 25, 40 | Retracted |

Table 4.3 Design variables for planform optimization.

| DESIGN VARIABLES (7) | | |
|---|---|---|
| | **Lower Bound** | **Upper Bound** |
| **Root Chord (V1)** | 0.2 | – |
| **TE Kink Sweep (V2)** | 0 | 90 |
| **Tip Chord (V3)** | 0.13 | – |
| **LE Sweep (V4)** | 0 | 40 |
| **Root Twist (V5)** | -10 | 10 |
| **Tip Twist (V6)** | -10 | 10 |
| **Kink Position (V7)** | 0.1524 | – |
| **Wing Surf. Area** | 0.5523 (Constant) | |
| **Span** | Calculated from the design variables | |

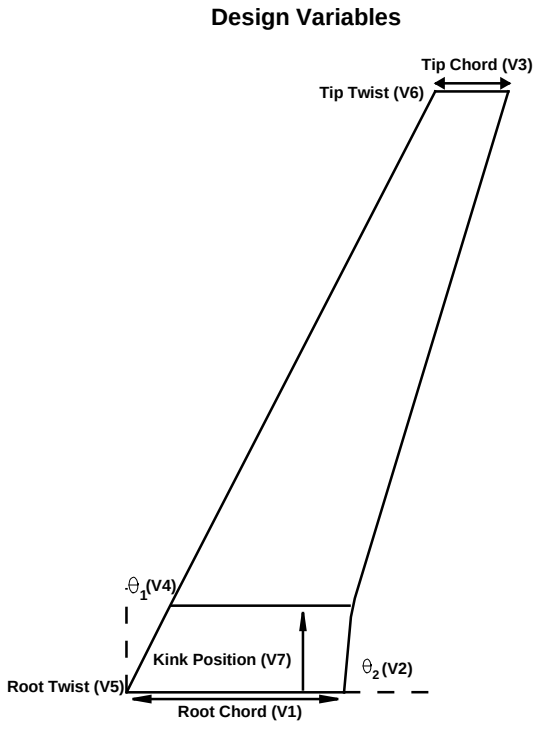


Figure 4.11 Design variables for planform optimization.

## 4.6 Optimization Results

### 4.6.1 High-Speed Optimization

The use of 2.5D RANS sectional data has a significant effect on the transonic shock as presented in Section 3.6. Therefore, it allows us to perform cruise optimization with the wave drag sensitivity in regards to sweep. The same optimization has been performed for different cruise Mach numbers to evaluate compressibility effects over the optimal planform. Since the twist is a design variable, the angle of attack has been fixed to 1°. The optimization problem is defined as follow,

$$\begin{aligned} \underset{x}{\text{minimize}} \quad & -\frac{C_L}{C_D} \\ \text{subject to} \quad & W_w(x) - W_{w_{reference}} \leq 0.0 \end{aligned}$$

where $W$ is the wing's weight calculated with Torenbeek (Equation 4.3). The weight constraint ensures the solution is not heavier than the reference Lovell wing.

As the cruise Mach number is increased, the optimal planform sweep is also increased(Figure 4.12). At a high Mach number, increasing sweep reduces wave drag, thus the optimal solution at a Mach number of 0.8 has a higher LE sweep of 39° compared to the Lovell wing 30.5° LE sweep. Therefore, the optimized planform has lower viscous drag (Figure 4.13). These results confirm the sensitivity of viscous drag in regard to the sweep from the 2.5D RANS sectional data.

Additionally, the optimizer has succesfully brought the maximum lift-to-drag ratio at the desired angle of attack of 1° (Figures 4.14(a)-4.14(b)). CMA-ES also managed to keep roughly the same lift-to-drag ratio around 29 for the different cruise mach numbers (Table 4.4). The optimal lift coefficient at 1° is also lower with increasing mach number. A population size of 16 was used, thus less than 187 optimizer iterations was necessary to converge (Figure 4.15).

Table 4.4 Optimized results for different Mach number at $\alpha = 1°$.

| **Mach** | **0.6** | **0.65** | **0.7** | **0.75** | **0.78** | **0.8** |
|---|---|---|---|---|---|---|
| **CL** | 0.409 | 0.394 | 0.391 | 0.359 | 0.333 | 0.344 |
| **CL/CD** | 29.36 | 29.11 | 29.11 | 28.95 | 28.71 | 28.85 |

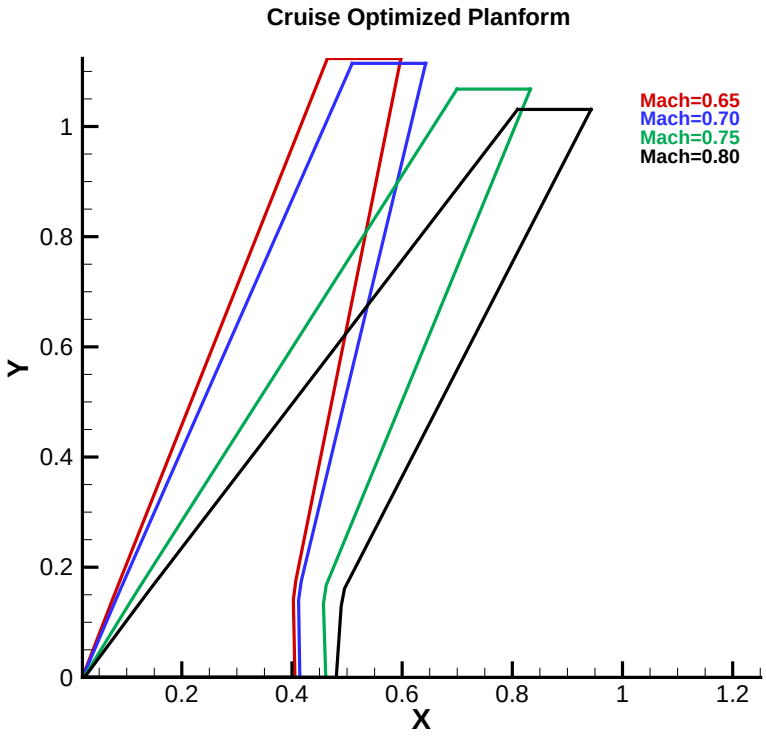


Figure 4.12 Optimized planform for different cruise Mach number.

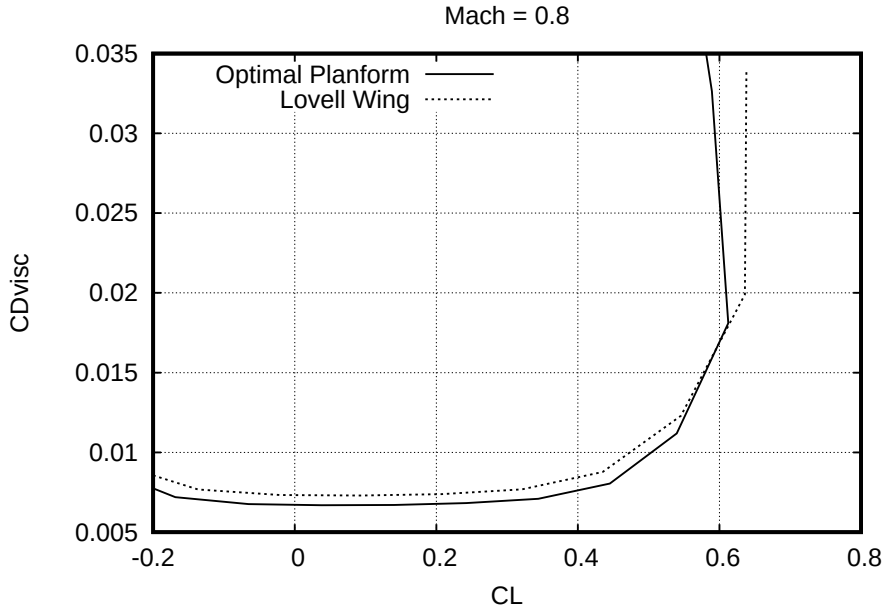


Figure 4.13 Viscous drag vs $C_L$ at $Mach = 0.8$.

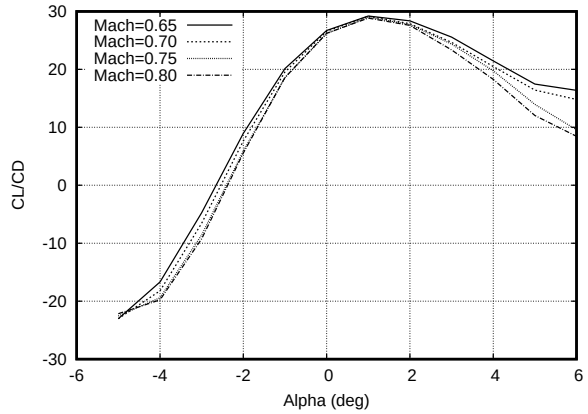


(a) Lift-to-drag ratio of optimized planform for different cruise Mach number.

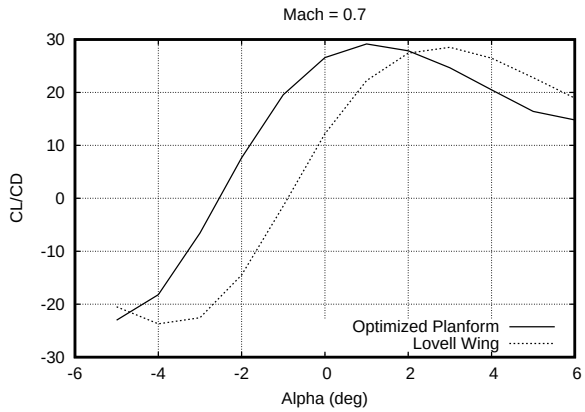


(b) Lift-to-drag ratio of optimized planform at Mach = 0.7.

Figure 4.14 High-speed lift-to-drag ratio optimization

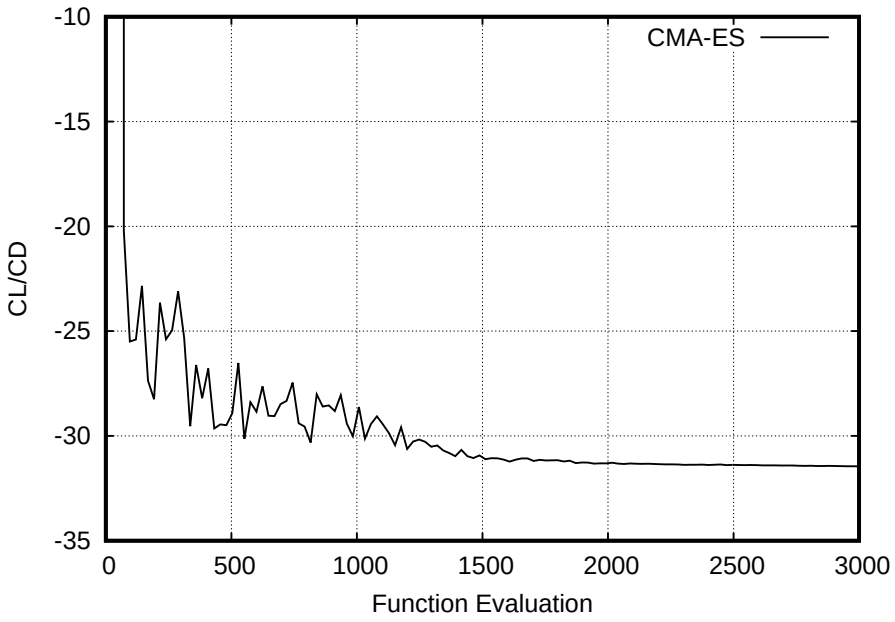


Figure 4.15 Lift-to-drag ratio optimization convergence at $Mach = 0.75$.

### 4.6.2 Low-Speed Optimization

The aerodynamic design of high-lift systems requires a tradeoff between maximum lift coefficient and lift-to-drag ratio. The takeoff distance and climb performance are strongly affected by lift-to-drag ratio. On the other hand, the approach airspeed, according to certification (Transport Canada 2012), must be $1.23 \times V_{s_{1g}}$ where $V_s$ is the stall speed. Therefore landing performance is directly related to $C_{L_{max}}$.

At takeoff, one important airspeed is $V_2$, the speed at which the aircraft may safely be climbed with one engine inoperative and according to certification, $V_2 = 1.13 \times V_s$(Transport Canada 2012). The lift-to-drag ratio at $V_2$ influence directly climb performance and $V_2$ can also be expressed in terms of lift coefficient, $C_{L_2} = \frac{C_{L_{max}}}{1.13^2}$. The lift-to-drag ratio at $C_{L_2}$ should therefore be considered as an objective function with $C_{L_{max}}$. However, CMA-ES is a single objective optimizer, thus composite objective function with user-defined weights is used (Equation 4.4). For simplicity, the high-lift configuration is considered constant along the span with the slat deflected at 25° and the flap deflected at 10°.

Single objective $C_{L_{max}}$ optimization yields a solution with a low lift-to-drag ratio of 7.76 at $C_{L_2}$ and a low aspect ratio planform (Figure 4.16 and Table 4.5). Adding the lift-to-drag ratio to the objective function is necessary for takeoff performance and in order to evaluate $C_D$ accurately at $C_{L_2}$, a Proportional Integral Derivative controller (PID) is used to find the correct AoA for the desired $C_{L_2}$.

The tradeoff between climb performances and $C_{L_{max}}$ is observed by a pareto front when performing the same optimization with different weights for $C_{L_{max}}$ (Figure 4.17). As the weight is reduced for $C_{L_{max}}$ in the objective function, the optimal planform sweep is increase, which in turns reduces the $C_{L_{max}}$ and increases the lift-to-drag ratio at $C_{L_2}$ (Figure 4.18 and Table 4.5).

$$\begin{aligned} \underset{x}{\text{minimize}} \quad & -W_1\big(C_{L_{max}}\big) - W_2\Big(\frac{C_L}{C_D}\Big)_{@C_{L_2}} \\ \text{subject to} \quad & W_w(x) - W_{w_{reference}} \leq 0.0 \end{aligned} \tag{4.4}$$

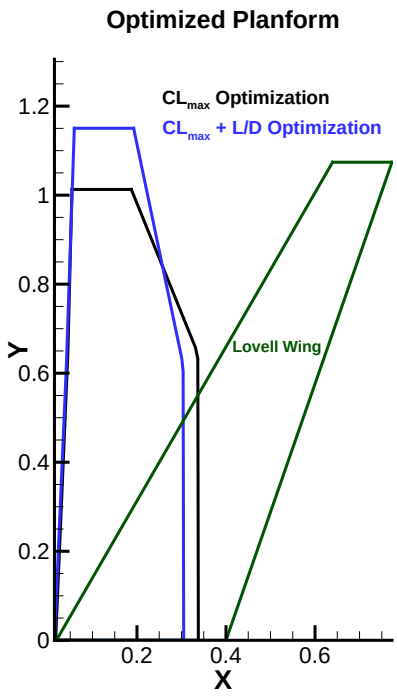


Figure 4.16 ($C_{L_{max}}$) Optimization compared with ($C_{L_{max}} + \frac{C_L}{C_D}$ at $C_{L_2}$) optimization.

Table 4.5 Low-Speed optimization results.

| | **Weights** | $C_{L_{max}}$ | $\frac{C_L}{C_D}$ |
|---|---|---|---|
| $W_{C_{L_{max}}}$<br>$W_{\frac{C_L}{C_D}}$ | 1.0<br>0.0 | 3.45 | 7.76 |
| $W_{C_{L_{max}}}$<br>$W_{\frac{C_L}{C_D}}$ | 2.0<br>1.0 | 2.85 | 11.19 |
| $W_{C_{L_{max}}}$<br>$W_{\frac{C_L}{C_D}}$ | 2.5<br>1.0 | 2.89 | 11.12 |
| $W_{C_{L_{max}}}$<br>$W_{\frac{C_L}{C_D}}$ | 3.0<br>1.0 | 3.18 | 10.37 |
| $W_{C_{L_{max}}}$<br>$W_{\frac{C_L}{C_D}}$ | 5.0<br>1.0 | 3.32 | 9.84 |
| $W_{C_{L_{max}}}$<br>$W_{\frac{C_L}{C_D}}$ | 10.0<br>1.0 | 3.43 | 9.61 |

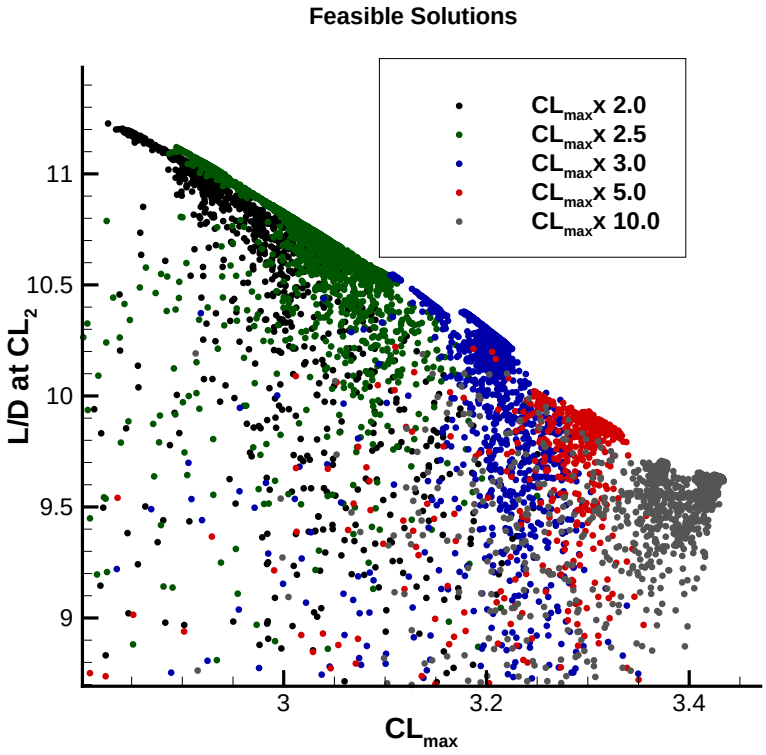


Figure 4.17 Optimization solution with different weights for $C_{L_{max}}$.

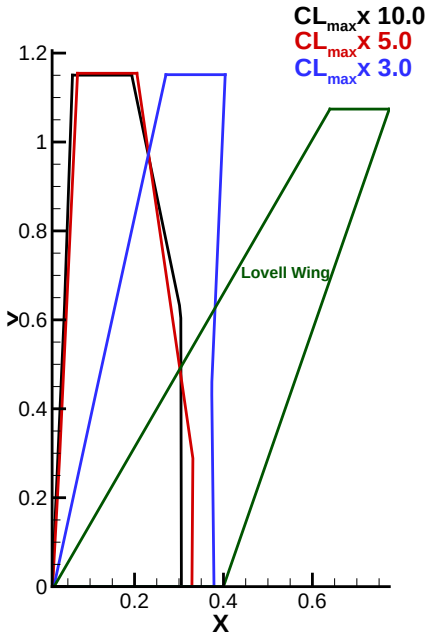


Figure 4.18 Optimization solution comparison with different weights for $C_{L_{max}}$.

### Spanwise Stall Constraint

It is required per certification of transport aircraft that handling qualities are adequate to allow a safe recovery from high angle of attack where stall conditions are reached (Federal Aviation Administration 2016). However, swept wings tend to have a higher spanload towards the tip which contributes to a less stable outboard stall. The VLM/RANS solver allows the spanwise stall position to be detected with stall cells(Spalart, 2014) (Figure 4.7) and can be introduced as a constraint in the optimization to ensure stable stall conditions. The spanwise stall constraint is chosen to be less than 60% of the span.

The stall constraint is well handled by the optimizer (Figure 4.19) with the optimal planform stalling at 58%. Moreover, adding the stall constraint does not change the overall planform (Figure 4.20(a)). Only the twist distribution is affected by the constraint (Table 4.6) with a $4.02°$ root twist and $-1.55°$ tip twist as anticipated. The optimization was performed with a population size of 16 and around 125 iterations was necessary to converge toward the optimal solution (Figure 4.20(b)).

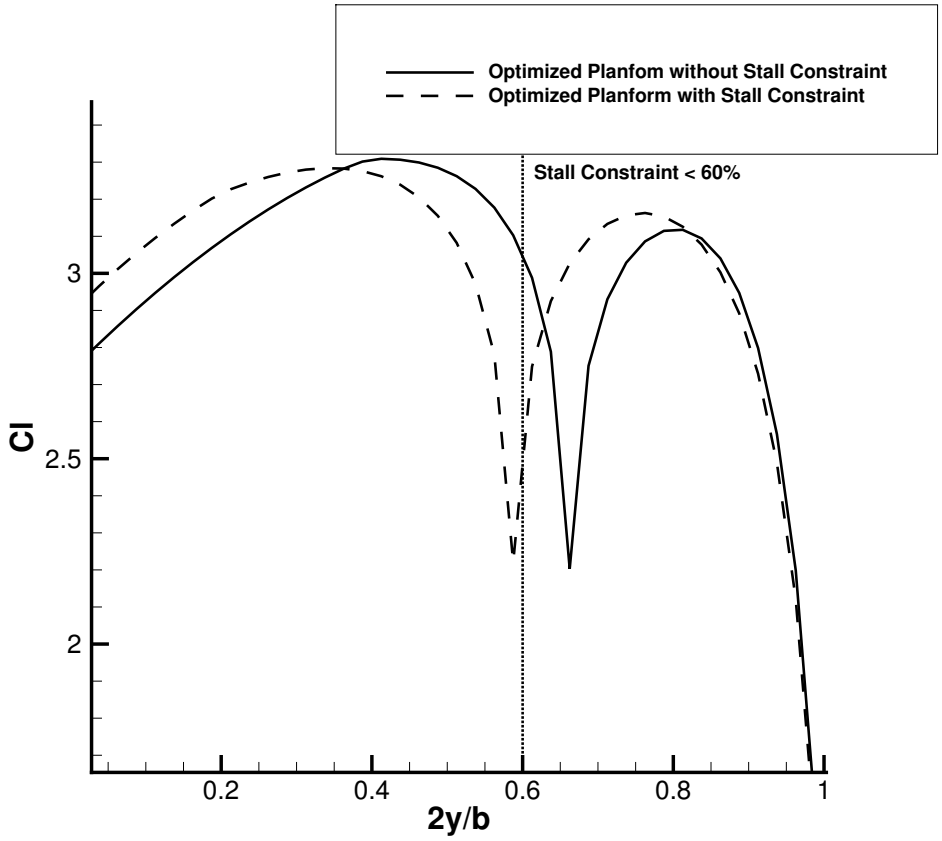


Figure 4.19 Spanwise stall constraint.

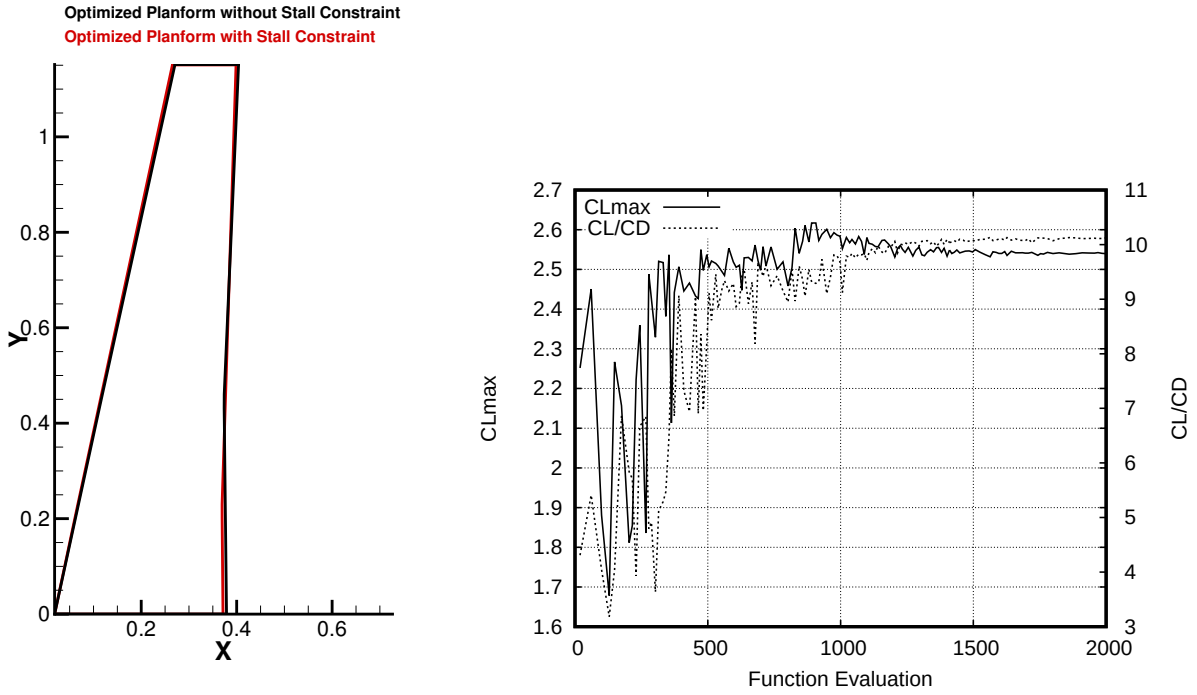


(a) Optimized planform.

(b) Objective functions convergence.

Figure 4.20 Low-speed optimization with spanwise stall constraint

Table 4.6 Optimmal solution with and without spanwise stall constraint.

| | **Root Twist** | **Tip Twist** | $C_{L_{max}}$ | $\frac{C_L}{C_D}$ | **Spanwise Stall Pos.** |
|---|---|---|---|---|---|
| **Optimization without Stall Constraint** | -3.06 | -1.66 | 3.18 | 10.37 | 67% |
| **Optimization with Stall Constraint** | 4.02 | -1.55 | 3.24 | 10.14 | 58% |

### High-Lift Configuration Optimization

The clean planform is modeled by the VLM while the section characteristics are incorporated by the viscous data. Therefore, high-lift optimization can be performed by assigning different viscous sectional data corresponding to different high-lift configurations along the span. One scenario explored is a slat optimization to achieved a minimum $C_{L_{max}}$. The problem is defined with 2 design variables, the start and end points of the slat along the span. The objective function is to minimize the slat length for a required $C_{L_{max}}$ (Equation 4.5).

The optimal solution for different $C_{L_{max}}$ constraint (Figure 4.21) shows the continuity of the solution, thus confirming the performance and robustness of CMA-ES and the aerodynamic solver.

$$\begin{aligned} \underset{y_1,y_2}{\text{minimize}} \quad & L_{slat}(y_1, y_2) = y_2 - y_1 \\ \text{subject to} \quad & CL_{maxTarget} - CL_{max}(y_1, y_2) \leq 0.0 \\ & y_1 - y_2 \leq 0.0 \end{aligned} \tag{4.5}$$

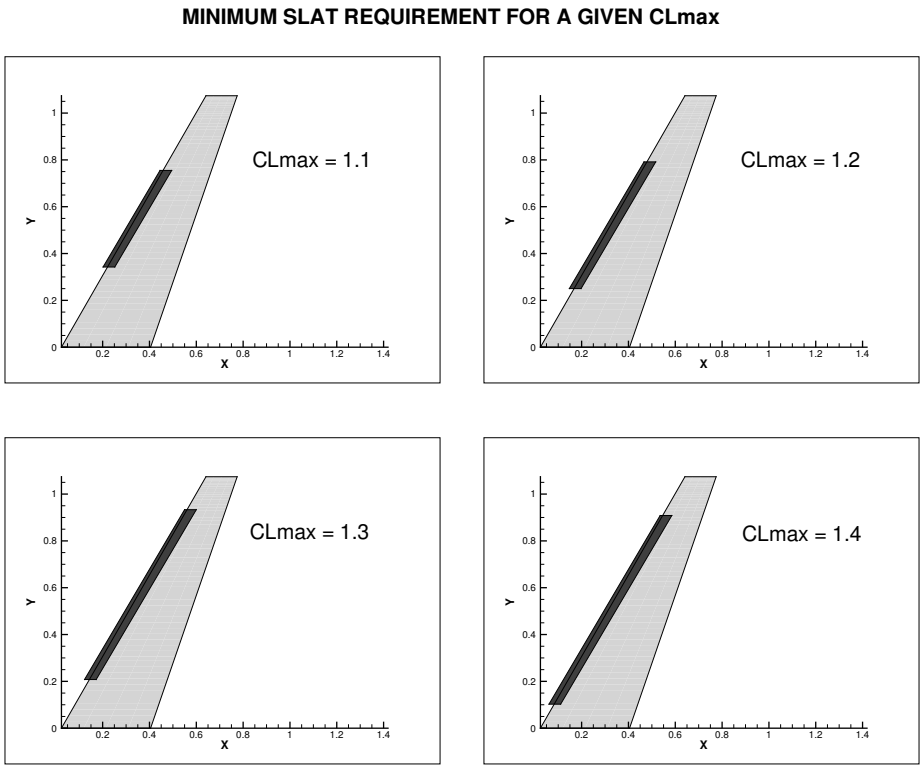


Figure 4.21 Optimiation of slat configuration.

### 4.6.3 Multi-Obective Low-Speed and High-Speed Optimization

Finally, a composite objective function optimization combining the previous low-speed and high-speed objectives is explored with cruise conditions at Mach = 0.75 (Equation 4.6). The optimal planform lies between the low-speed and high-speed optimal planforms with a moderate leading edge sweep (Figure 4.22). The low-speed optimized planform has poor cruise performance with a lift-to-drag ratio of 9.74 (Table 4.7). On the other hand, the high-speed optimized planform has a relatively low $C_{L_{max}}$ of 2.596 compared to the low-speed optimized planform. Combining low-speed and high-speed objective functions result in a solution with good stall characteristics, climb performances and cruise performances as well (Table 4.7).

$$\begin{aligned} \underset{x}{\text{minimize}} \quad & -5.0 \times \left(C_{L_{max}}\right) - 1.0 \times \left(\frac{C_L}{C_D}\right)_{@C_{L_2}} - 1.0 \times \left(\frac{C_L}{C_D}\right)_{cruise} \\ \text{subject to} \quad & W_w(x) - W_{w_{reference}} \leq 0.0 \end{aligned} \tag{4.6}$$

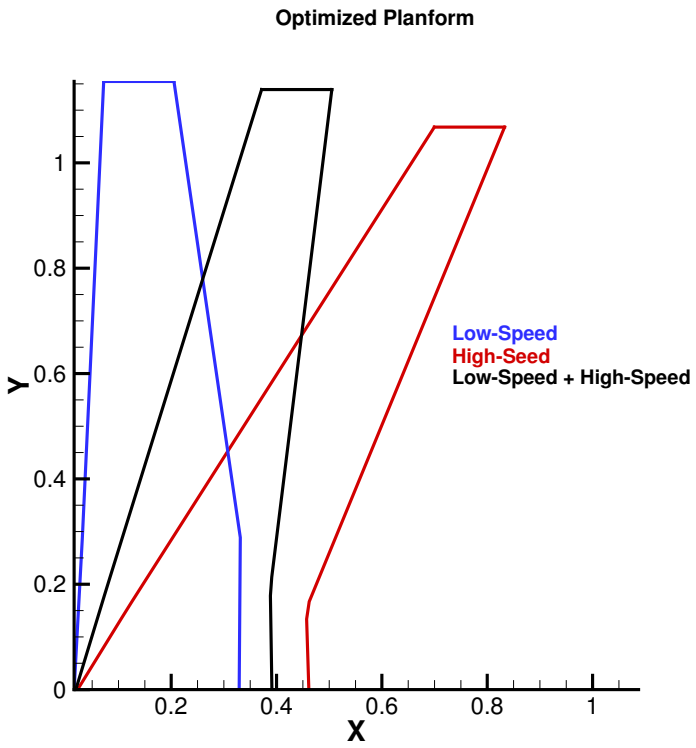


Figure 4.22 Optimized planform comparison with composite low-speed/high-speed objective function.

Table 4.7 High-speed and low-Speed optimization performed at $Mach = 0.75$ for cruise conditions.

| | $C_{L_{cruise}}$ | $\frac{CL}{CD}@C_{L_{cruise}}$ | $C_{L_{max}}$ | $\frac{CL}{CD}@V_2$ |
|---|---|---|---|---|
| **Low-Speed Optimization** | 0.086 | 9.74 | 3.32 | 9.84 |
| **High-Speed Optimization** | 0.359 | 28.95 | 2.596 | 10.96 |
| **Low-Speed/High-Speed Optimization** | 0.46 | 27.02 | 3.12 | 10.48 |

# CHAPTER 5 CONCLUSION

## 5.1 Synthesis of Work

The overarching goal of the current project is to develop an aerodynamic tool suitable for conceptual multi-disciplinary design optimization with low computational cost and sufficient fidelity to explore a large design space.

The first objective was to assess the fidelity of a Vortex Lattice Method coupled with 2.5D RANS approach for high-lift design with a comparison to 3D RANS solutions. A Vortex Lattice Method was developed using the object-oriented capabilities of C++ and an exhaustive numerical verification was performed to assess the level of accuracy that can be achieved with the method using 2D and 2.5D RANS sectional data. The verification was performed on the Bombardier Research Wing (BRW) for clean and high-lift configurations. The *alpha-based* coupling algorithm was further developed to enable the use of 2.5D RANS sectional data by incorporating a correction factor to the local angle of attack. The solutions were compared against Bombardier's high fidelity 3D RANS flow solver DRAGON. The results of the verification campaign showed the importance of incorporating the crossflow for $C_{L_{max}}$ and flap spanload prediction. The crossflow effects were mainly visible when analyzing the spanload over the flap at high deflections. Moreover, it was found that the appropriate sweep line to generate the 2.5D RANS data should be between the quarter-chord and the half-chord sweep line. The work also highlights the importance of the sweep factor with coupling procedures, as well as the benefits of introducing artificial dissipation. Overall, the method provides surprisingly high fidelity results comparable to 3D RANS solutions with outboard separation well captured.

The second objective was to explore the various optimization problems and the level of complexity and accuracy that can be achieved using a VLM coupled with 2.5D RANS approach. Aerodynamic planform optimization was performed based on the Lovell wing. More than 3000 2.5D RANS simulations were performed to assemble the viscous database to cover a wide range of low-speed and high-speed conditions. Single-objective and composite-objective function optimization were performed, combining clean planform configuration and high-lift configurations in low-speed/high-speed conditions. The optimizer used was a gradient-free Covariant Matrix Adaptation Evolution Strategy (CMA-ES). The capability of the VLM/2.5D approach in capturing stall cells was used to introduce a new spanwise stall criteria and incorporated as an optimization constraint. This non-linear constraint was well handled by the optimizer, thus confirming the robustness of both the optimizer and the VLM/2.5D coupling

algorithm. This section thus highlights a novel multi-topology optimization procedure.

## 5.2 Limitations of the Proposed Solution

Even though adequate results were achieved with the VLM/2.5 RANS solver, the method does not model the fuselage. The fuselage has a significant effect on the spanwise loading of the wing and the flaps. While the fuselage cannot be ignored when designing the wing, the Vortex Lattice Method is only appropriate for thin lifting surfaces, leading to a gap in modeling requirements.

The second major limitation is the viscous database when performing optimization. Sectional RANS simulations are performed to incorporate viscous corrections and the airfoil geometry is included in the RANS data, not the VLM. In other words, if the airfoil geometry changes, a new set of 2D/2.5D RANS simulations must be performed. Important computation cost is added if the airfoil geometry is chosen as a design variable. Because of this limitation, the optimization performed in this work was with a constant airfoil geometry.

## 5.3 Future Work

In light of the previous limitations, three ideas are proposed for future developments :

1. To overcome the issue of fuselage effect, the Vortex Lattice Method can be replaced by a Panel method that can handle complex geometries such as wing-fuselage junctions. This would require modification to the coupling algorithm. The panel method uses additional doublet and source singularities as opposed to the VLM where only vortex filaments are used.
2. To use airfoil geometry as a design variable without increasing drastically the computation time, a solution could be to replace RANS calculation by Euler/Boundary-layer methods like MSES (Drela, 2007). However, it will be necessary to implement the infinite swept wing condition to capture the viscous cross-flow effects.
3. Finally, instead of replacing the sectional RANS calculations by lower fidelity methods, the viscous database could be enlarged by adding airfoil characteristics. The idea is to construct a reduced order model from all the RANS solutions to quickly estimate the aerodynamic coefficients in regards of the airfoil geometry. Proper Orthogonal Decomposition (POD) (Malouin, 2010) could be used to construct the reduced order model. Computation cost is then only added in the viscous database generation, which is performed once. The aerodynamic analysis would remain as fast as the current method.

# REFERENCES

AFTOSMIS, M. J., NEMEC, M., and CLIFF, S. E., "Adjoint-based low-boom design with cart3d," *29th AIAA Applied Aerodynamics Conference*, June 2011.

ANDERSON, J., *Fundamentals of aerodynamics*. McGraw-Hill New York, 2001, vol. 2.

ARNOLD, D. and HANSEN, N., "A (1+1)-cma-es for constrained optimisation." Philadelphia, United States : The Genetic and Evolutionary Computation Conference (GECCO), July 2012, pp. 297–304.

BLACKWELL, J., "A finite-step method for calculation of theoretical load distributions for arbitrary lifting-surface arangements at subsonic speeds," *NASA TN D-5335*, 1969.

BOURGAULT-COTE, S., GHASEMI, S., MOSAHEBI, A., and LAURENDEAU, E., "Extension of a two-dimensional navier–stokes solver for infinite swept flow," *AIAA Journal*, vol. 55, no. 2, February 2017.

CEBECI, T., SHAO, J., KAFYEKE, F., and LAURENDEAU, E., *Computational Fluid Dynamics for Engineers*. Springer Berlin Heidelberg New York, 2005.

CHATTOT, J.-J., "Analysis and design of wings and wing/winglet combinations at low speeds," *Computational Fluid Dynamics Journal*, vol. 13, no. 3, 2004.

COLLANGEA, G., DELATRE, N., HANSEN, N., QUINQUIS, I., and SCHOENAUER, M., *Multidisciplinary Optimisation in the Design of Future Space Launchers*. ISTE Ltd and John Wiley & Sons, Inc, 2010.

DRELA, M., "Mses : Multi-element airfoil design/analysis software," *Massachusetts Inst. of Technology*, 2007.

DYKE, M. V., *An Album of Fluid Motion*. The Parbolic Press, Stanford, California, 1988.

ELHAM, A., "Adjoint quasi-three-dimensional aerodynamic solver for multi-fidelity wing aerodynamic shape optimization," *Aerospace Science and Technology*, vol. 41, pp. 241–249, 2015.

ELHAM, A., TOOREN, M. V., and ROCCA, G. L., "An advanced quasi-analytical weight estimation method for airplane lifting surfaces," *71st International Conference on Mass Properties, Society of Allied Weight Engineers*, no. 3571, May 2012.

ELHAM, A. and VAN TOOREN, M. J., "Winglet multi-objective shape optimization," *Aerospace Science and Thecnology*, 2014.

*Flight Test Guide For Certification Of Transport Category Airplanes*, Federal Aviation Administration, October 2016.

GALLAY, S. and LAURENDEAU, E., "Nonlinear generalized lifting-line coupling algorithms for pre/poststall flows," *AIAA Journal*, vol. 53, no. 7, pp. 1784–1792, 2015.

GALLAY, S. and LAURENDEAU, E., "Preliminary design aerodynamic model for complex configurations using lifting line coupling algorithm," *Journal Aircraftl*, vol. 53, no. 4, 2016.

GALLAY, S., GHASEMI, S., and LAURENDEAU, E., "Sweep effects on non-linear lifting line theory near stall," in *52nd Aerospace Sciences Meeting*. National Harbor, Maryland : AIAA, 2014, pp. 1105–1124.

GALLAY, S., "Algorithmes de couplage rans et d'ecoulement potentiel," Ph.D. dissertation, Ecole Polytechnique de Montreal, 2016.

HANSEN, N., and KERN, S., "Evaluating the CMA evolution strategy on multimodal test functions," in *Parallel Problem Solving from Nature PPSN VIII*, ser. LNCS, YAO, X. *et al.*, Eds., vol. 3242. Springer, 2004, pp. 282–291.

HILEMANA, J., SPAKOVSKY, Z. S., DRELA, M., SARGEANT, M., and JONES, A., "Airframe design for silent fuel-efficient aircaft," *Journal of Aircraft*, vol. 47, no. 3, May 2010.

JAMESON, A., *Encyclopedia of Computational Mechanics*. ohn Wiley & Sons Ltd., 2004.

KAFYEKE, F., PIPERNI, P., and ROBIN, S., "Application of ktran transonic small disturbance code to the challenger business jet configuration with winglets," *SAE Technical Paper*, 1988.

KATZ, J. and PLOTKIN, A., *Low-Speed aerodynamics*. Cambridge University Press, 2001, vol. 13.

KUCHEMANN, D., "A simple method for calculating the span and chordwise loading on straight and swept wings of any given aspect ratio at subsonic speeds," *Aeronautical Research Council Reports and Memoranda*, no. 2935, 1956.

KUCHEMANN, D., *The Aerodynamic Design of Aircraft*. AIAA, 2012.

LOVELL, D. A., "A wind-tunnel investigation of the effects of flap span and deflection angle, wing planform and a body on the high-lift performance of a 28 degrees swept wing," R.A.E., Tech. Rep. 1372, 1977.

MALOUIN, B., "Prediction of aerodynamic coefficients using proper orthogonal decomposition," Ph.D. dissertation, École Polytechnique de Montréal, 2010.

MARIENS, J., ELHAM, A., and VAN TOOREN, M. J. L., "Quasi-three-dimensional aerodynamic solver for multidisciplinary design optimization of lifting surfaces," *Journal of Aircraft*, vol. 51, no. 2, March 2014.

MARIENS, J., "Wing shape multidisciplinary design optimization," Master's thesis, Delft University of Technology, 2012.

MASKEW, B., "Program vsaero theory document : A computer program for calculating nonlinear aerodynamic characteristics of arbitrary configurations," NASA, Tech. Rep., 1987.

MUKHERJEE, R., GOPALARATHNAM, A., and KIM, S. W., "An iterative decambering approach for post-stall prediction of wing characteristics using known section data," *AIAA Paper*, vol. 1097, 2003.

N., H. and A., O., "Completely derandomized self-adaptation in evolution strategies," *Evolutionary Computation*, vol. 9, no. 2, pp. 159–195, 2001.

PHILLIPS, W. and SNYDER, D., "Modern adaptation of prandtl's classic lifting-line theory," *Journal of Aircraft*, vol. 37, no. 4, pp. 662–670, 2000.

PIGEON, A. L., A.-T, and LAURENDEAU, E., "Two-dimensional navier-stokes flow solver developments at école polytechnique de montréal," *22nd Annual Conference of the CFD Society of Canada*, 2014.

PIPERNI, P. and DEBLOIS, A., "Development of a multilevel multidisciplinary- optimization capability for an industrial environment," *AIAA Journal*, vol. 51, no. 10, October 2013.

PISTOLESI, E., "Bertrachtungen uber die gegenseitige beeinflussung von tragflugelsystem (considerations on the mutual interference of aerofoil systems)," *L.G.L. Rep.*, pp. 214–219, 1937.

RIZZI, A., "Modeling and simulating aircraft stability and control—the simsac project," *Progress in Aerospace Sciences*, vol. 47, no. 8, pp. 573–588, 2011.

SAFFMAN, P. G., *Vortex Dynamics*. Cambridge Univ. Press, 1992.

SEARS, W., "Some recent developments in airfoil theory," *Journal of the Aeronautical Sciences*, vol. 23, no. 5, pp. 490–499, 1956.

SIVELLS, J. and NEELY, R., "Method for calculating wing charateristics by lifting-line theory using nonlinear section lift data," National Advisory Committee for Aeronautics, Washington, DC, United States, Rapp. tech., 1947.

SOCIETY, R. A., "Vgk method for two dimensional aerofoil sections," *ESDU Data Item 69028*, London, September 1996.

SPALART, P. R., "Prediction of lift cells for stalling wings by lifting-line theory," *AIAA Journal*, vol. 52, no. 8, pp. 1817–1820, 2014.

TANI, I., "A simple method of calculating the induced velocity of a monoplane wing," *Aeronautical Research Institut., Tokyo Imperial University*, vol. 111, 1934.

TORENBEEK, E., *Synthesis of Subsonic Airplane Design*. Delft Univ. Press, The Netherlands, 1976.

*Aeronautical Information Manual GEN – 1.0 GENERAL INFORMATION*, Transport Canada, October 2012.

TSENG, J. and LAN, C., "Calculation of aerodynamic characteristics of airplane configuratioons at high angles of attack," National Advisory Committee for Aeronautics, Rapp. tech., 1988.

VAN DAM, C., "The aerodynamic design of multi-element high-lift systems for transport airplanes," *Progress in Aerospace Sciences*, vol. 38, no. 2, pp. 1775–1779, 2002.

VORST, H. A. V. D., "Bi-cgstab : A fast and smoothly converging variant of bi-cg for the solution of nonsymmetric linear systems*," *Society for Industrial and Applied Mathematics*, vol. 13, no. 2, pp. 631–644, March 1992.

WEISSINGER, J., "The lift distribution of swept-back wings," *National Advisory Committee for Aeronautics*, 1947.

WILLCOX, K. and WAKAYAMA, S., "Simulataneous optimization of a multiple-aircraft family," *Journal of Aircraft*, vol. 40, no. 4, July 2003.

YANG, H. and LANGLOIS, M., "Towards accurate simulation of aircraft high-lift flows with one and two-equation turbulence models," *AERO 2015 - CASI*, 2015.

# APPENDIX A Non-Linear Effect Captured with the VLM/RANS Solver

The two-dimensional RANS simulations allow complex flow physics to be captured and incoporated inside the 3D solution of the VLM. For example, a separation bubble on the main component of the wing is captured from 5° to 8° when the slat is deflected. This separation bubble induces a kink in the lift curve slope which is captured both by experimental data and the non-linear VLM coupled with 2.5D RANS (Figure A.1). The RANS solutions were performed with chimera meshes with NSCODE (Pigeon *et al.*, 2014) (Figure A.2).

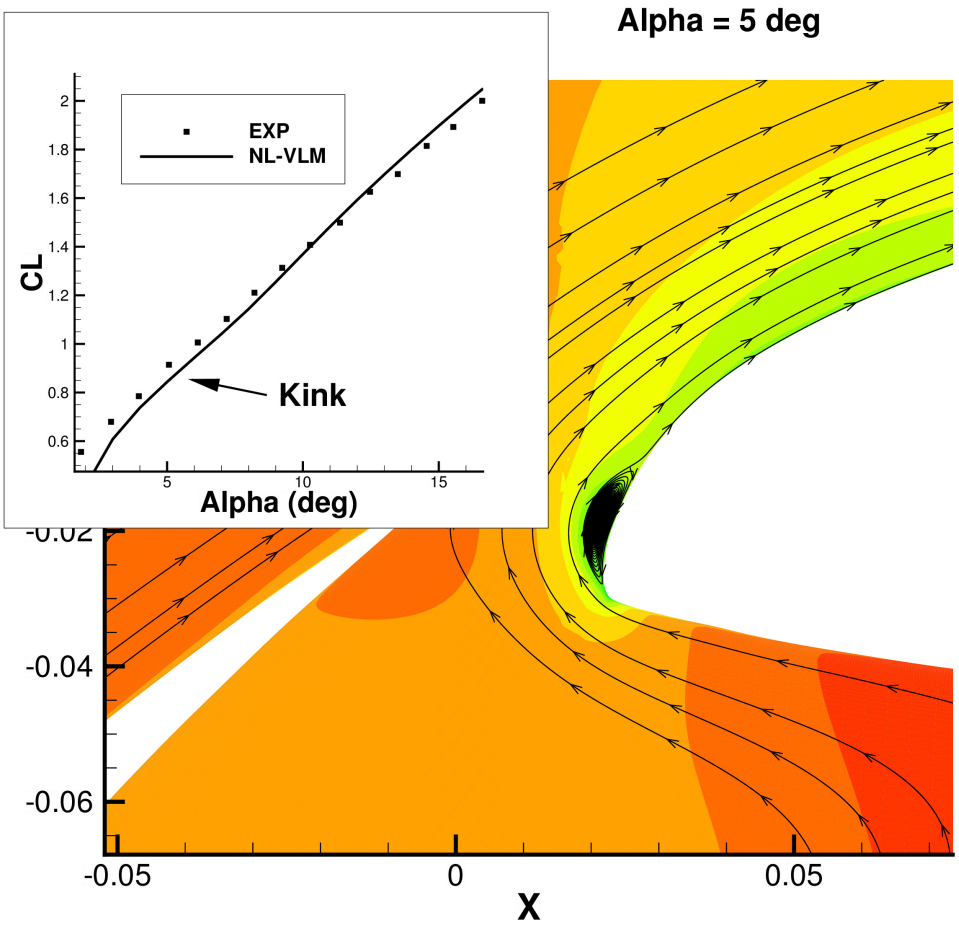


Figure A.1 Lovell - Non-Linear Effects Captured by the VLM/2.5D RANS Solver

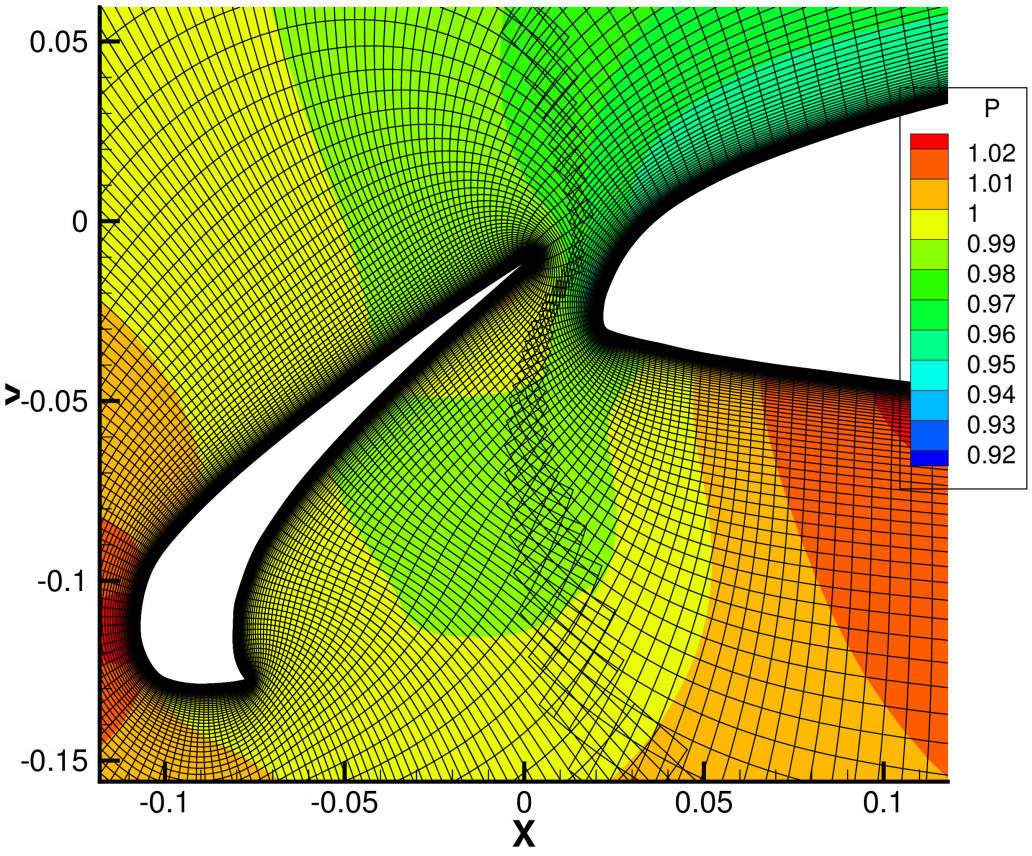


Figure A.2 Lovell - Chimera Mesh Used for 2D RANS Simulation

# APPENDIX B VLM Script Run Example

```
import numpy as np
import os.path,imp
import subprocess
from math import *
libpath = "MERCURIAL_VLM/"
import sys
sys.path.append(libpath+".shared")
sys.path.append(libpath+"Python")
from VLM.Geometry import *
from VLM.vlm import *
from VLM.Math import Vector3,Vector
from Solver import solver
from Postprocessor import postprocess
import os
import time
import filecmp
global evalIT

goem = 'planform.geom'
viscData = ViscDataBase('ViscousData.dat')

Lovell = Geometry()
wing = Component(Name='Wing')
rightWing = Body(Sym=1,Name='RightWing',ViscousData=viscData,CFDsweep=30.51)
rightWing += Element(planformFile=newgoem,ifWake=True,nspan=50,ncord=5,mesh='
    Cosine')
wing += rightWing
Lovell += wing

nlvlm = NLVlm(Nthread=4,geom=Lovell,Sref=0.5523,Cmac=0.257123,
            Xref=Vector3(0.3349,0.0,0.0),Mach=0.0,Beta=0.0,
            CouplingIter=300,Relaxation=0.5,CouplingTol=1e-5)

case = solver(vlm=nlvlm,alpha=range(0,20))

case.solve()
post = postprocess(case,Forces=1,SectionData=1,view3D=1)
```

### Planform File (*planform.geom*)

```
Planform
y z x chord twist
0.000000 0.000000 0.000000 0.380923 0.000000
0.537000 0.000000 0.316443 0.257128 0.000000
1.074000 0.000000 0.632887 0.133323 0.000000
```

### Viscous Data File (*ViscousData.dat*)

```
Polar 0.000000 30.510000
Alpha CL CD CM
-6.000000 -0.053437 0.099639 -0.065678
-5.000000 -0.045378 0.091088 -0.061882
-4.000000 -0.043241 0.083367 -0.057841
-3.000000 -0.045636 0.076251 -0.054600
-2.000000 -0.045973 0.069226 -0.054843
-1.000000 -0.034020 0.062021 -0.061371
0.000000 0.012702 0.053988 -0.080349
1.000000 0.479778 0.030053 -0.217653
2.000000 0.665371 0.029514 -0.236493
3.000000 0.801479 0.031074 -0.238662
4.000000 0.925709 0.033101 -0.236362
5.000000 1.044088 0.035154 -0.231590
6.000000 1.164972 0.036391 -0.226261
7.000000 1.328314 0.032392 -0.226359
8.000000 1.478922 0.030113 -0.221139
9.000000 1.619506 0.029077 -0.213807
10.000000 1.751459 0.029172 -0.204926
11.000000 1.877469 0.029899 -0.194837
12.000000 1.998510 0.031155 -0.183806
13.000000 2.115332 0.032801 -0.171988
14.000000 2.227499 0.034943 -0.159605
15.000000 2.335756 0.037353 -0.146690
16.000000 2.444651 0.039512 -0.133566
17.000000 2.544347 0.042499 -0.119731
18.000000 2.638130 0.046025 -0.105486
```

```
19.000000 2.726280 0.049857 -0.090814
20.000000 2.807806 0.054160 -0.075802
21.000000 2.881531 0.058939 -0.060450
22.000000 2.945259 0.064643 -0.044953
23.000000 2.996465 0.071146 -0.029405
24.000000 3.029367 0.078841 -0.014147
25.000000 2.979029 0.094145 -0.006850
26.000000 2.934942 0.113049 -0.003036

Polar 0.500000 30.510000
Alpha CL CD CM
-6.000000 -0.048234 0.100294 -0.066223
-5.000000 -0.039707 0.091750 -0.062388
-4.000000 -0.036988 0.084002 -0.058301
-3.000000 -0.038995 0.076866 -0.054878
-2.000000 -0.039729 0.069927 -0.054622
-1.000000 -0.029167 0.062836 -0.060390
0.000000 0.012381 0.055321 -0.077710
1.000000 0.260482 0.039869 -0.154907
2.000000 0.657923 0.030072 -0.234330
3.000000 0.794768 0.031627 -0.236732
4.000000 0.918811 0.033707 -0.234456
5.000000 1.036120 0.035879 -0.229570
6.000000 1.154018 0.037406 -0.223824
7.000000 1.296593 0.035743 -0.220600
8.000000 1.462006 0.031667 -0.218192
9.000000 1.604240 0.030430 -0.211129
10.000000 1.736465 0.030479 -0.202342
11.000000 1.862112 0.031219 -0.192287
12.000000 1.982503 0.032521 -0.181275
13.000000 2.098551 0.034222 -0.169474
14.000000 2.209626 0.036446 -0.157076
15.000000 2.316492 0.038956 -0.144134
16.000000 2.423827 0.041230 -0.130977
17.000000 2.521390 0.044345 -0.117067
18.000000 2.612580 0.048026 -0.102737
```

```
19.000000 2.697510 0.052044 -0.087972
20.000000 2.775091 0.056574 -0.072891
21.000000 2.843765 0.061626 -0.057503
22.000000 2.900969 0.067681 -0.042032
23.000000 2.943205 0.074597 -0.026605
24.000000 2.924180 0.086158 -0.015148
25.000000 2.875098 0.105609 -0.012948
26.000000 2.849604 0.117971 -0.002314
27.000000 2.773385 0.133453 0.003447

Polar 1.000000 30.510000
Alpha CL CD CM
-6.000000 -0.037861 0.100789 -0.067795
-5.000000 -0.028351 0.092133 -0.064040
-4.000000 -0.027019 0.084683 -0.059558
-3.000000 -0.028751 0.077560 -0.055981
-2.000000 -0.030215 0.070736 -0.055363
-1.000000 -0.022665 0.063953 -0.060229
0.000000 0.015786 0.056690 -0.076629
1.000000 0.193908 0.044326 -0.133179
2.000000 0.578571 0.033928 -0.217515
3.000000 0.779753 0.032803 -0.232804
4.000000 0.905005 0.034894 -0.230735
5.000000 1.019952 0.037259 -0.225658
6.000000 1.132558 0.039239 -0.219457
7.000000 1.261151 0.039043 -0.214291
8.000000 1.421368 0.035405 -0.211375
9.000000 1.571055 0.033330 -0.205426
10.000000 1.704767 0.033197 -0.196957
11.000000 1.829509 0.033985 -0.186965
12.000000 1.948152 0.035421 -0.175950
13.000000 2.062157 0.037273 -0.164139
14.000000 2.170502 0.039696 -0.151679
15.000000 2.273812 0.042454 -0.138622
16.000000 2.376965 0.045027 -0.125333
17.000000 2.469025 0.048476 -0.111223
```

```
18.000000 2.553620 0.052552 -0.096695
19.000000 2.630344 0.057050 -0.081747
20.000000 2.697839 0.062156 -0.066563
21.000000 2.752959 0.067973 -0.051200
22.000000 2.786184 0.075313 -0.036023
23.000000 2.736020 0.092088 -0.031045
24.000000 2.695029 0.106483 -0.021931
```

# APPENDIX C BRW - Complete Results

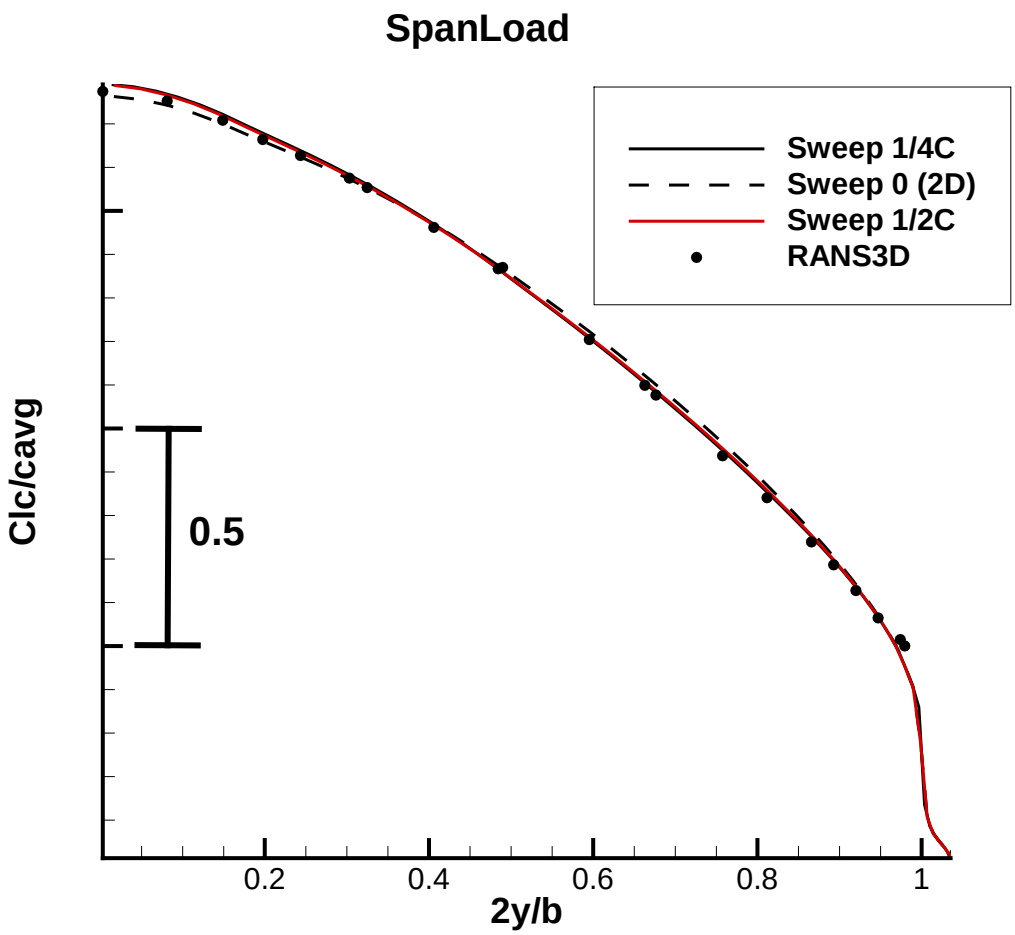


Figure C.1 BRW - Clean configurarion spanLoad at CL = 1.285

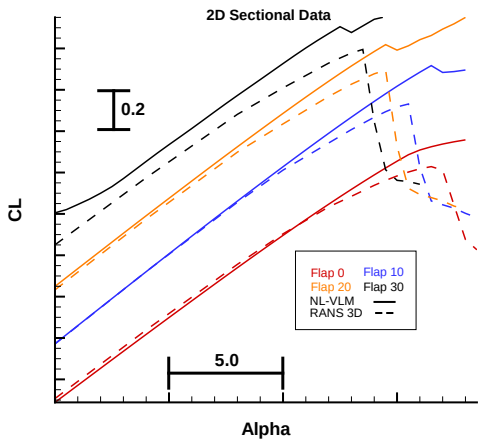


Figure C.2 BRW - CL with 2D Sectional Data

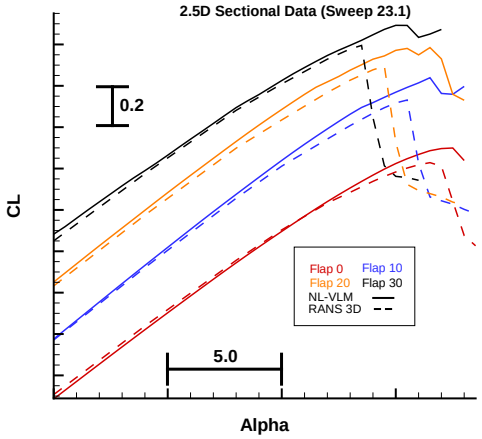


Figure C.3 BRW - CL with 2.5D (Sweep 1/2C) Sectional Data

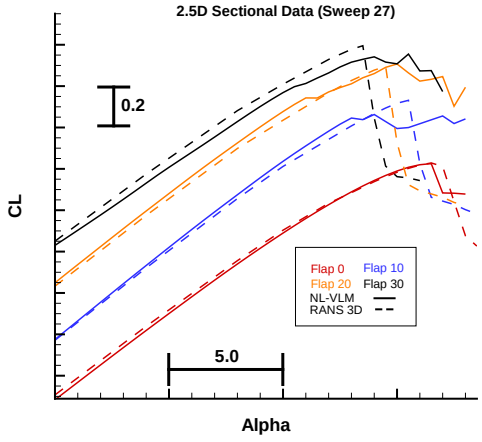


Figure C.4 BRW - CL with 2.5D (Sweep 1/4C) Sectional Data

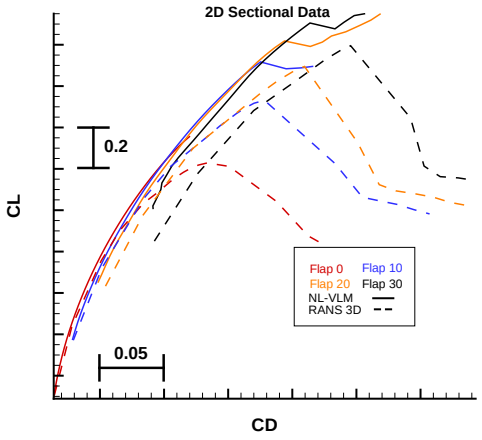


Figure C.5 BRW - CD with 2D Sectional Data

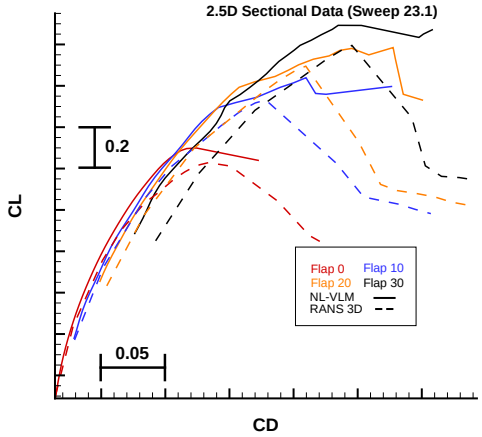


Figure C.6 BRW - CD with 2.5D (Sweep 1/2C) Sectional Data

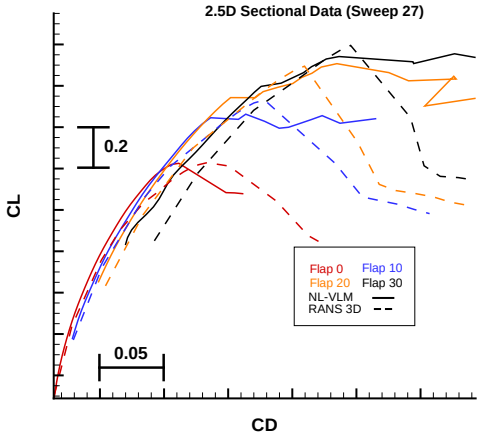


Figure C.7 BRW - CD with 2.5D (Sweep 1/4C) Sectional Data

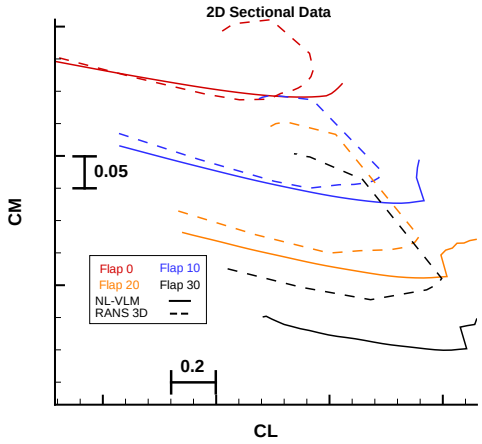


Figure C.8 BRW - CM with 2D Sectional Data

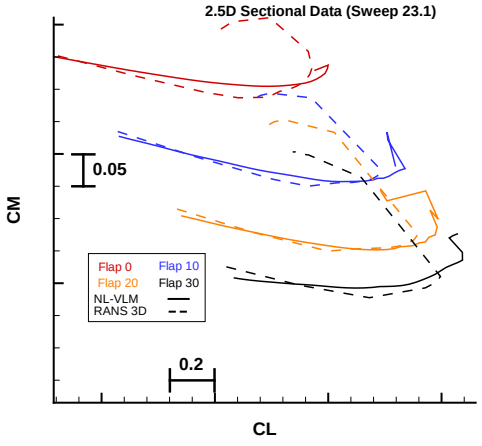


Figure C.9 BRW - CM with 2.5D (Sweep 1/2C) Sectional Data

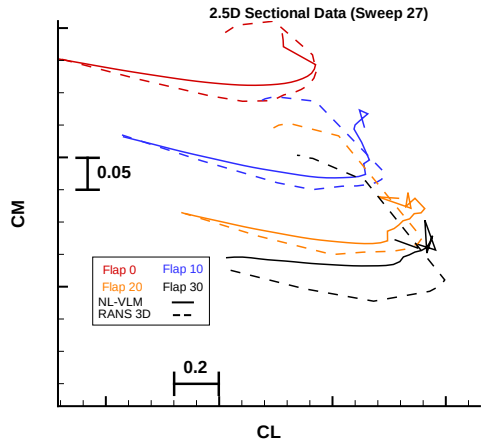


Figure C.10 BRW - CM with 2.5D (Sweep 1/4C) Sectional Data

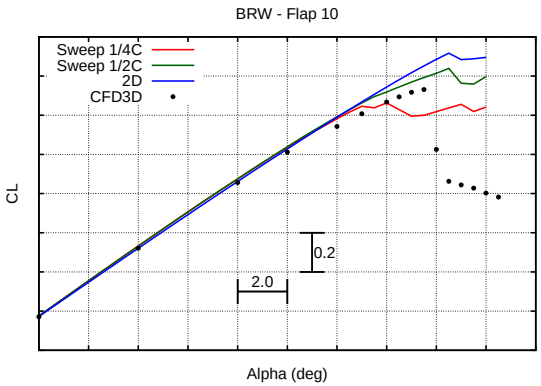


Figure C.11 BRW - Flap 10 - $C_L$

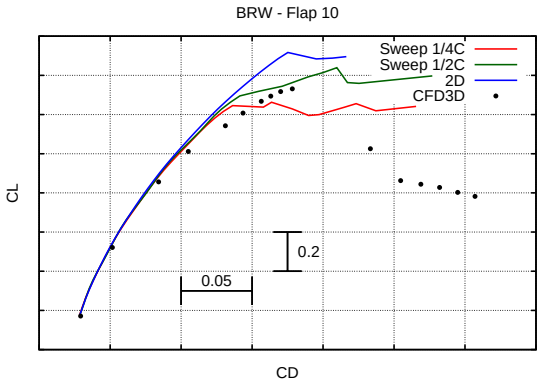


Figure C.12 BRW - Flap 10 - $C_D$

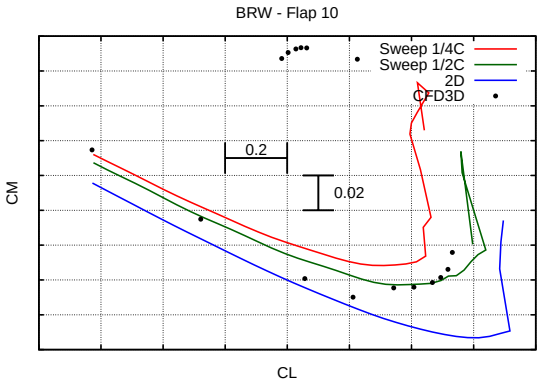


Figure C.13 BRW - Flap 10 - $C_M$

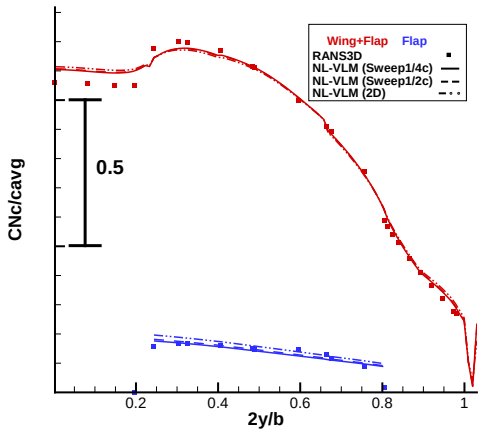


Figure C.14 SpanLoad Flap 10 at $C_L$ = 0.921

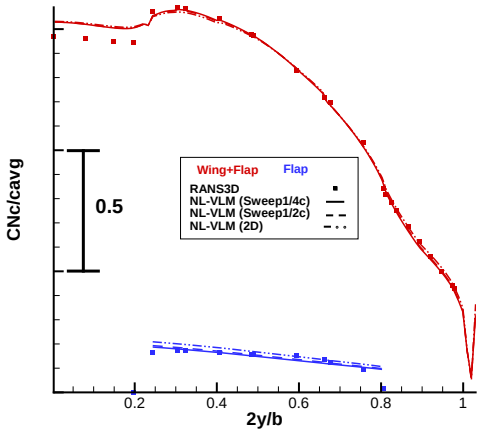


Figure C.15 SpanLoad Flap 10 at $C_L$ = 1.256

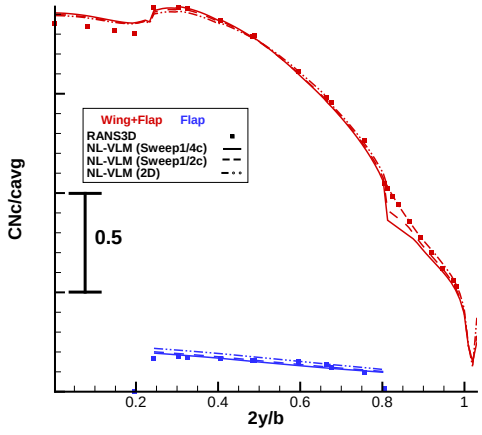


Figure C.16 SpanLoad Flap 10 at $C_L$ = 1.543

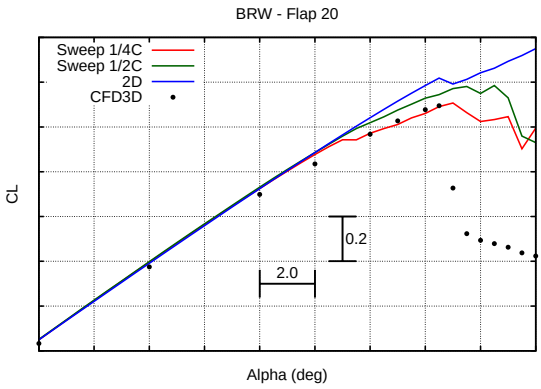


Figure C.17 BRW - Flap 20 - $C_L$

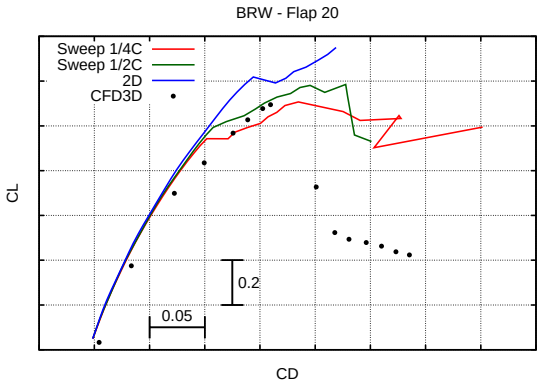


Figure C.18 BRW - Flap 20 - $C_D$

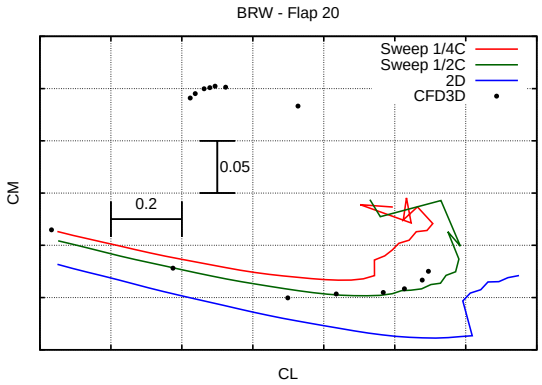


Figure C.19 BRW - Flap 20 - $C_M$

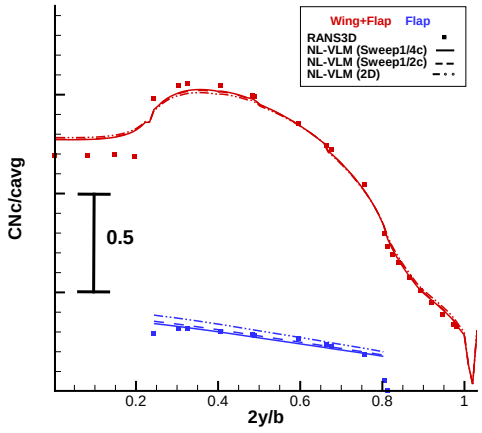


Figure C.20 SpanLoad Flap 20 at $C_L = 1.175$

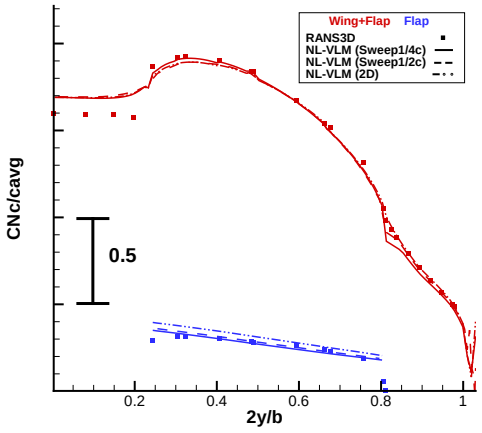


Figure C.21 SpanLoad Flap 20 at $C_L = 1.499$

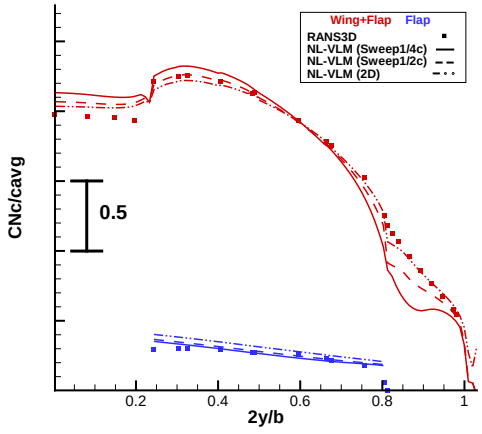


Figure C.22 SpanLoad Flap 20 at $C_L = 1.767$

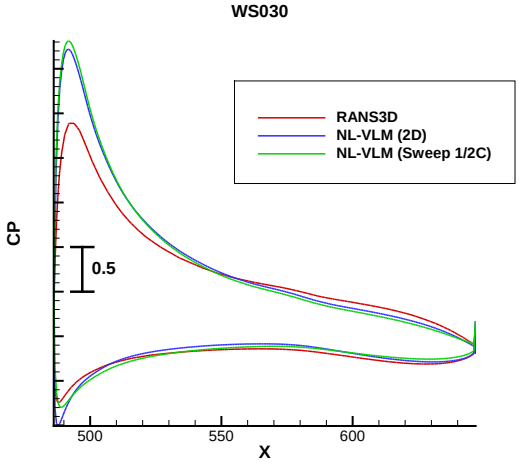


Figure C.23 Flap 20 Pressure Distribution at WS030 at $C_L = 1.499$

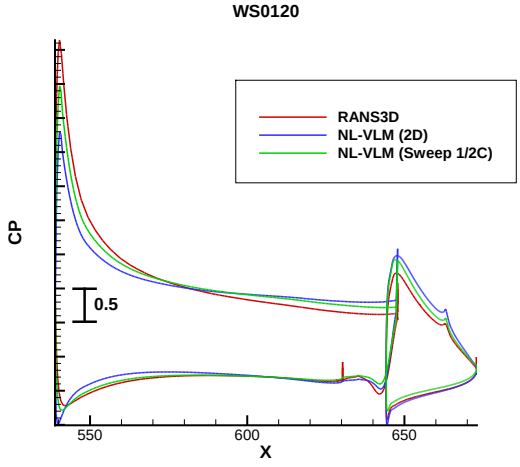


Figure C.24 Flap 20 Pressure Distribution at WS120 at $C_L = 1.499$

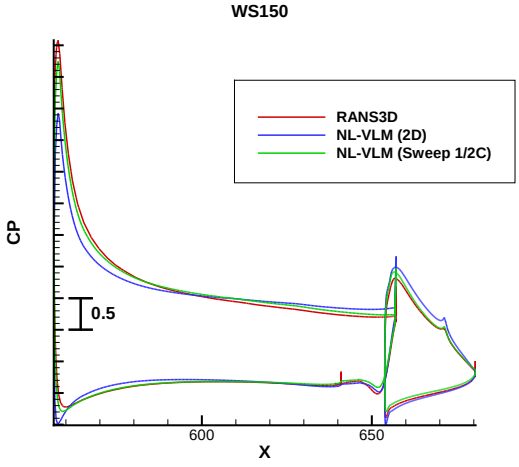


Figure C.25 Flap 20 Pressure Distribution at WS150 at $C_L = 1.499$

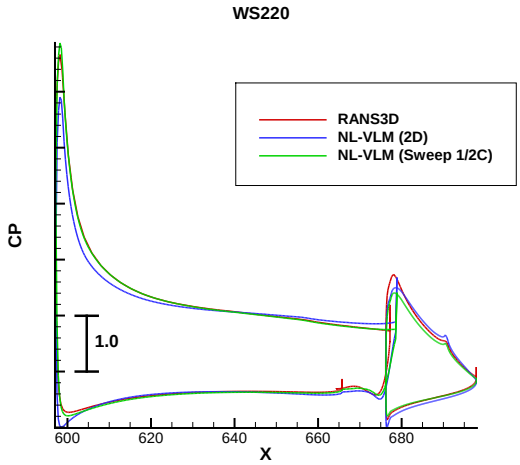


Figure C.26 Flap 20 Pressure Distribution at WS220 at $C_L = 1.499$

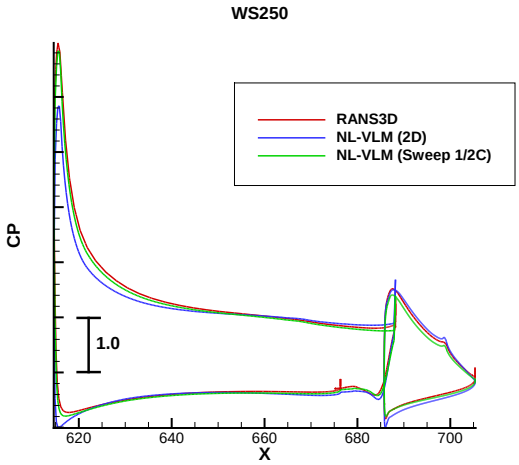


Figure C.27 Flap 20 Pressure Distribution at WS250 at $C_L = 1.499$

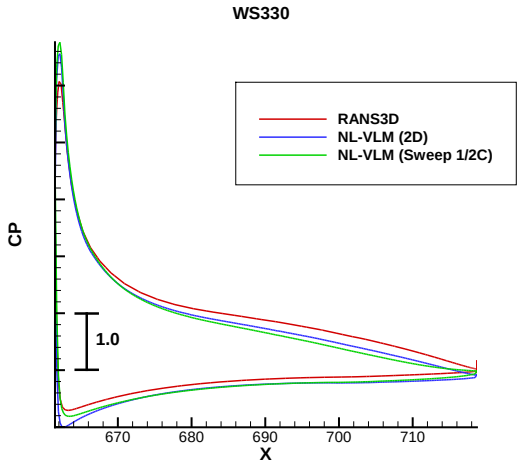


Figure C.28 Flap 20 Pressure Distribution at WS330 at $C_L = 1.499$

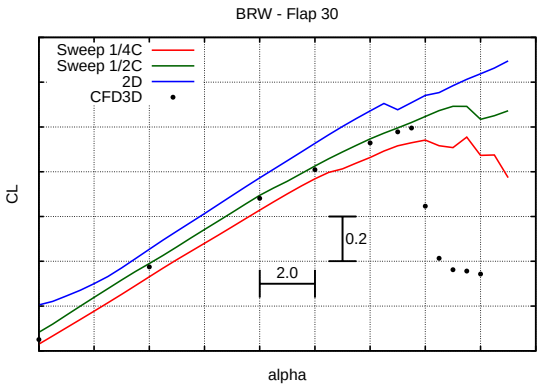


Figure C.29 BRW - Flap 30 - $C_L$

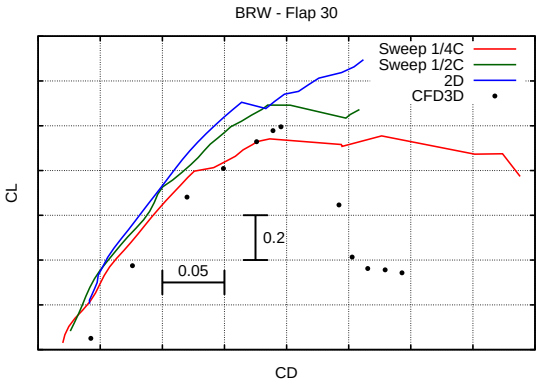


Figure C.30 BRW - Flap 30 - $C_D$

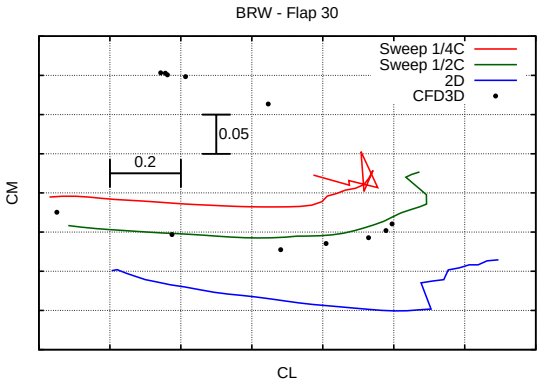


Figure C.31 BRW - Flap 30 - $C_M$

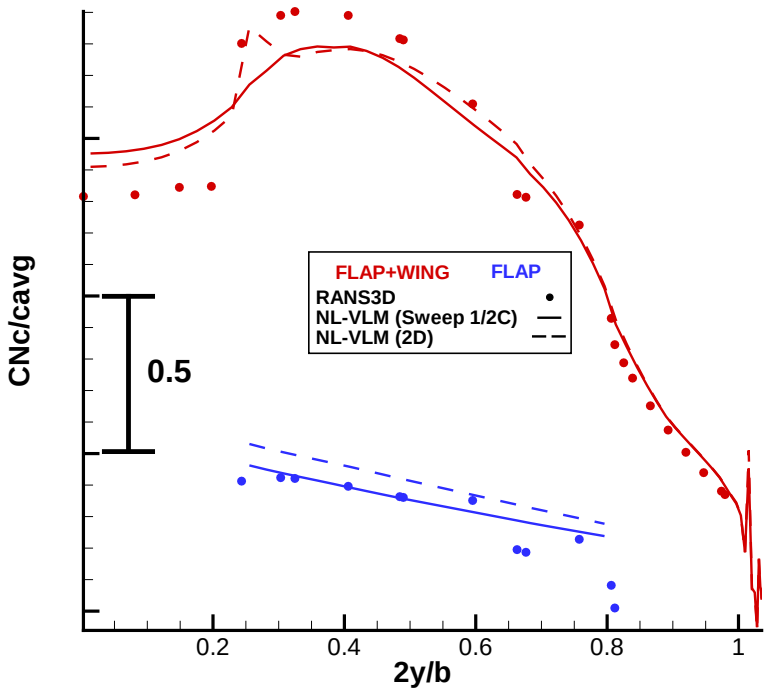


Figure C.32 SpanLoad Flap 30 at $C_L = 1.375$